8-1-2018

Grain Size Effects on Viscoelastic Relaxation of Sub-micron Thickness FCC Metallic Films

Jeffrey Smyth
Lehigh University, smyth122@gmail.com

Recommended Citation

Smyth, Jeffrey, "Grain Size Effects on Viscoelastic Relaxation of Sub-micron Thickness FCC Metallic Films" (2018). *Theses and Dissertations*. 4321.
https://preserve.lehigh.edu/etd/4321

Grain Size Effects on Viscoelastic Relaxation of Sub-micron Thickness FCC Metallic Films

By

Jeffrey R. Smyth

Presented to the Graduate and Research Committee

of Lehigh University

in Candidacy for the Degree of

Doctor of Philosophy

in

Materials Science & Engineering

Lehigh University

August 2018

Approved and recommended for acceptance as a dissertation in partial fulfillment of the requirements for the degree of Doctor of Philosophy.

____

Date

____

Accepted Date

____

Dissertation Advisor,

Prof. Richard P. Vinci

Committee Members:

____

Prof. Wojciech Z. Misiolek

____

Prof. Nicholas C. Strandwitz

____

Dr. Christopher D. Haines

ACKNOWLEDGEMENTS

The journey of this Ph.D. project expanded my scientific and engineering abilities beyond what I thought I was capable of when I started at Lehigh four years ago. My personal development would not have been possible without the kind, thoughtful, and compassionate support of my advisor, Professor Richard P. Vinci. He invited me into his research group to study thin film mechanical properties but I ended up learning much more about the fascinating world of Materials Science through his passion for the subject. I am deeply grateful for the knowledge and experience I gained from him over the years working in his lab.

I would also like to acknowledge the support from Dr. Walter L. Brown, who was instrumental in teaching me how the bulge thin film tester worked and operated. His laboratory know-how was second to none and I'll never forget his excitement when a well-planned experiment was successful. I am grateful for the advice and guidance Walter provided during my early years in the lab.

I would also like to thank the other members of my Ph.D. committee: Professor Wojciech Z. Misiolek, Professor Nicholas C. Strandwitz, and Dr. Christopher D. Haines for their time and technical guidance regarding my research progress.

Although not a complete list by any means, the following will acknowledge others in the Lehigh community who were pivotal in helping me complete my Ph.D. I am thankful to Mike Rex who helped me rebuild the bulge test chamber with careful

machining, assembling and welding. I am grateful for the patient tutelage of Dr. Rob Keyes and Bill Mushock who trained me on many of Lehigh's electron microscopes. Many thanks are due to the administrative staff in the department, including Katrina Kraft, Susan Stetler, Lisa Arechiga, and Janie Carlin. Of course, I must thank the fellow graduate students and post-docs who provided me equipment training, laughs, and coffee breaks.

I am thankful to the United States Army Armament Research, Development and Engineering (U.S. Army ARDEC) Fuze Division for allowing me to take a partial leave of absence to train in Dr. Vinci's lab. I am deeply appreciative for the support of my Fuze Division management, specifically Tom Crowley and Phil Gorman. In addition, I would like to thank funding support from the National Science Foundation (award no. CMMI-1332574) and the Department of Defense SMART scholarship program.

Finally, I would like to thank my friends and family. To all the friends who provided me an escape from the daunting process that is a Ph.D., thank you, it was well appreciated and needed. Thank you to my parents Kathy and Doug who have supported and encouraged me during this project and throughout my life. Thank you to Andy and Megan, the Nolfs, and our cats Pudge and Butters. A special thank you to my girlfriend, fiancé, and now wife Amy for being there with me every step of the way.

TABLE OF CONTENTS

LIST OF TABLES

LIST OF FIGURES

Abstract

Sub-micron thickness metallic thin films are known to exhibit mechanical size effects, where the thin film mechanical behavior can differ significantly from that of a bulk version of the same material. One such mechanical behavior, and the focus of this work, is the unique thin film viscoelastic deformation response to sub-yield, low-strain stimuli in near-ambient temperature environments. In engineering components using bulk materials, strains within the elastic regime are generally considered instantaneous. It is only at higher operating temperatures that temporal deformation processes, such as creep, are considered in bulk component design. However, in Micro-Electro-Mechanical Systems (MEMS), specifically Radio Frequency MEMS (RF MEMS) devices, the mechanical size effects of thin films result in time-dependent stress relaxation that can degrade component function and lead to reliability issues. For example, low temperature stress relaxation in RF MEMS thin films can cause a reduction in springback forces in moving membranes, leading to stiction failures and low device reliability.

The nanocrystalline structure and high purity of typical metallic thin films enable the viscoelastic behavior. In this study, the effect of microstructural features such as grain size and dislocation density are investigated for a series of face-centered cubic (FCC) metal films using the gas pressure bulge test technique at 80 °C. Commonly used MEMS metals including Ag, Al(Mg), Au, Cu, and Pt are grown to a nominally 500 nm thickness using the DC magnetron sputtering technique. The grain

size for each material class is altered by heating the film substrate during growth. SEM analysis is used to measure the planar grain size, D, of each film, ranging from 31.9 nm up through 878.4 nm. The dislocation density of each film is measured with TEM and XRD techniques, resulting in a range between 4.1×10^{14} m^{-2} to 15.1×10^{14} m^{-2} for all films.

The low-strain stress relaxation response of each film is fit using a four-term Prony series. The evaluating metric to compare viscoelastic behavior between films is the plane strain modulus decay after 10,000 s of relaxation. The Al(Mg), Au, and Pt films showed increasing relaxation with increasing grain size while the Ag and Cu films showed no relaxation dependence on grain size. The relaxation dependence is shown to be linearly proportional to D^n where n ranges from ½ to 2.

This work suggests that dislocation bowing and unbowing is the driving mechanism for the stress relaxation and respective recovery in metallic thin films. Thermal activation is associated with overcoming the Peierls barrier. For those films that exhibit a dependence of relaxation on grain size, it is shown that the average pinned dislocation segment length, L, increases as the grain size, D, increases, thereby allowing greater bowing and viscoelastic strain. Furthermore, calculated activation volumes for the first 100 s of relaxation change with D for those films that exhibit grain size dependence. This study indicates that the barrier to dislocation bowing was reduced with grain size for Al(Mg), Au, and Pt films but remained constant for Ag and Cu films.

A key outcome of this work is that the same relaxation mechanism is active in all FCC metals tested. A second outcome is that grain size dependence of viscoelastic stress relaxation is not an independent mechanism like Hall-Petch strengthening, but rather is a consequence of microstructural changes that accompany grain growth in certain metals.

1. Introduction

1.1 Background information

The material of choice for Micro-Electro-Mechanical Systems (MEMS) devices is predominantly silicon, due in part to the advancement of the material for the microelectronics industry over the past six or seven decades. Micromachining processes have been combined with chip-level electronics to produce microscale devices including pressure sensors, accelerometers, gyroscopes and optical devices [1]. One technology sector that could benefit from incorporation of MEMS devices is the RF (Radio Frequency) community [2]. For over a hundred years this industry has relied on bulky electromechanical relays to switch RF current from the on state to the off state. Although these devices perform well, they are large, expensive and will fail after a few million switching cycles. The solid-state switching industry [GaAs FETs, silicon on insulator (SOI), and silicon on sapphire (SOS)] has offered replacements for RF relay switches, but could not meet the conventional relay's switching performance. In contrast, a metal-contact technology such as an RF MEMS switch can provide superior performance ideally suiting it for the RF switching community. The five advantages of an RF MEMS switch over semiconductor and conventional switches [3] are: 1) higher isolation, 2) lower insertion loss, 3) very high linearity, 4) very low power consumption, and 5) high integration with different substrates.

Radio Frequency Micro-Electro-Mechanical Systems (RF MEMS) can be driven by different actuation mechanisms, including (1) electrostatic, (2) piezoelectric, (3) thermal, and (4) electromagnetic forces. The actuation occurs by converting electrical, thermal, or magnetic inputs into a response of mechanical motion. The electrostatic switch is the most widely developed device in which a thin metallic cantilever (or bridge) is pulled down across an air/vacuum gap to either short, open, or load an RF transmission line [4]. Switching is accomplished either by establishing direct contact between the moving electrode and a fixed electrode or by a change in capacitance between the moving electrode and a fixed electrode covered by a dielectric layer that prevents direct contact. Both styles of RF MEMS require low electrical resistivity materials for the cantilever, thus metals (and not silicon, doped or otherwise) are the material of choice. Column eight of Table 1.1 highlights the orders of magnitude difference in resistivity between silicon and the FCC metals used in this study. Lower resistivity allows quicker passage of electrical current, which ultimately allows increased switching frequencies. Currently, three main failure mechanisms of RF MEMS metal-contact switches are (1) contamination/frictional polymer formation leading to open switch, (2) adhesion leading to closed contacts, and (3) material transfer between contacting surfaces causing contact erosion [5]. Of these three, only adhesion is an issue for capacitive switches.

The adhesion or stiction failure mechanism listed above provides the motivation for this present work, which is focused on the underlying mechanics of FCC metallic thin films. The viscoelastic behavior of metal thin films has been shown to be a primary contributor to membrane stiction susceptibility [6,7] which can compromise overall device reliability. It has previously been shown that Au thin films are likely to exhibit significant viscoelastic behavior, and that the degree of stress relaxation is temperature dependent [8]. Measurements of activation energy indicated a dislocation-based relaxation mechanism. Tests also showed that the rate and extent of viscoelastic stress relaxation is dependent on grain size. Au is somewhat unique among FCC metals with its lack of surface oxide and very high malleability. It has a low stacking fault energy and therefore favors the development of annealing twins and partial dislocations. It has not been shown that the viscoelastic behavior seen in Au is also present in other FCC metals and alloys, and if the same general trends apply. This is the motivation for the current work; material properties that affect viscoelastic stress relaxation behavior of common FCC thin film metals (Al, Ag, Au, Cu, and Pt) are investigated to determine how universal reversible relaxation is in this class of metals, and to identify common trends such as dependencies on grain size and dislocation density. The underlying mechanism driving the viscoelastic trends has been studied through the determination of dislocation pinning geometries, dislocation densities, and activation volumes.

The following sections of this chapter discuss in more detail the RF MEMS devices that motivate this work, methods for fabricating metal films and characterizing their mechanical behavior, and the specific case of viscoelastic response.

1.2 RF MEMS switch design

Au thin films have been studied extensively as the cantilever beam or bridge of an RF MEMS chip, owing to its high electrical conductivity, inertness, and resistance to oxidation. For the most part these films are machined using MEMS-enabled micromachining and deposition techniques where the thickness of the film is submicron [9–12]. Figure 1.1 depicts a typical micromachined RF MEMS capacitive switch fixed-fixed bridge, where the suspended Au beam is deposited to 370 nm thickness.

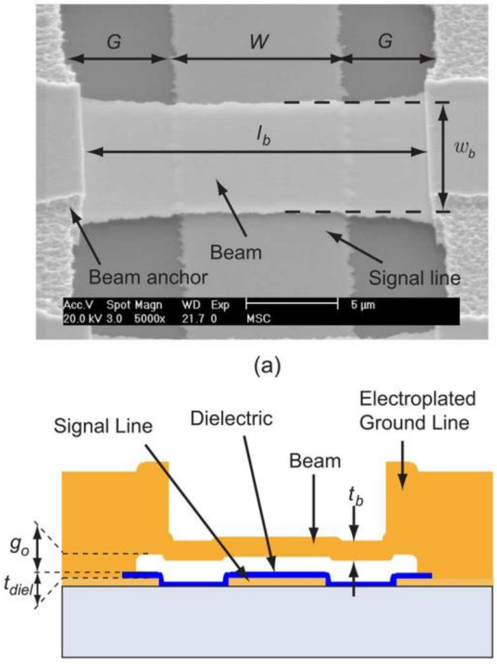

(a)

(b)

Figure 1.1 Capacitive RF MEMS Au beam example from [10] a) top-down SEM image of Au membrane b) cross sectional schematic, t_b = 370 nm

To actuate the device as depicted in in Figure 1.1, the Au microbeam must be pulled down across the air gap, g_0. The attractive force to do this work can be equated in the following way:

$$F_e = -\frac{1}{2}\frac{\varepsilon A V^2}{g^2} \tag{1.1}$$

Where F_e is the electrostatic attractive force, ε is the permittivity of gas between electrode and moving membrane, g is the gap distance, A is the overlap area, and V is the applied voltage. The counteracting restoring force, F_r, is dependent on the membrane stiffness, k, and the deflection of the beam (g_0-g):

$$F_r = k(g_0 - g) \tag{1.2}$$

The minimum pull-down voltage to switch the RF MEMS device from off to on is when the electrostatic force equals the restoring force, or $F_e = -F_r$. Figure 1.2 depicts the operation of an electrostatically-driven switch where an applied voltage will drive the membrane to the dashed position. The pull-down voltage is then:

$$V_{pull-in} = \sqrt{\frac{8}{27}\frac{k g_0^3}{\varepsilon_0 A}} \tag{1.3}$$

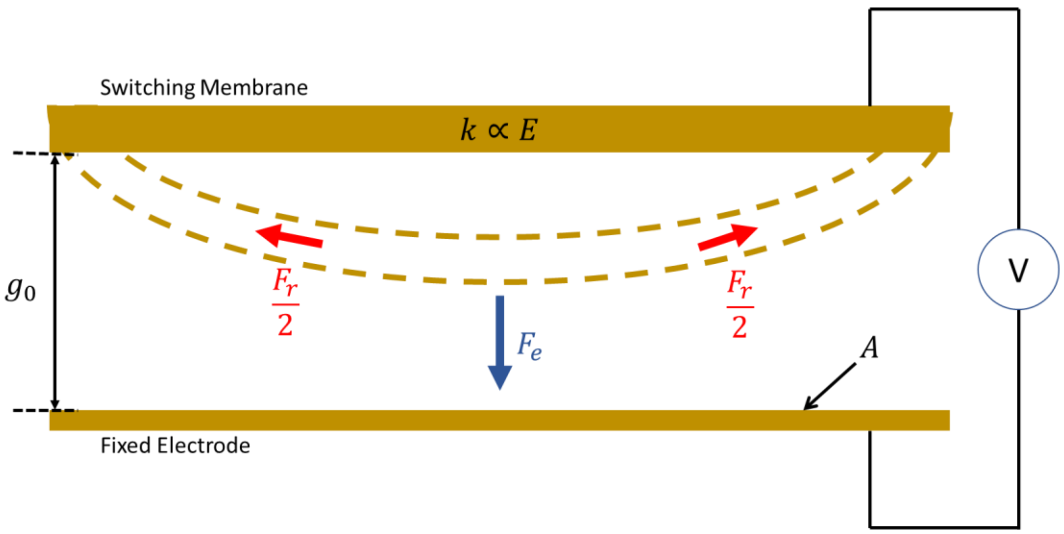

Figure 1.2 Schematic diagram of balance of forces in an electrostatically driven RF MEMS device

The membrane stiffness, k, is proportional to the geometric design (A = area, L = length) and the material properties (Young's Modulus, E):

$$k = \frac{F}{x} = \frac{AE}{L} \tag{1.4}$$

If the stiffness of the switching membrane is reduced, the restoring force for a given deflection is also reduced. Reduced membrane stiffness can result in the membrane failing to return to the open position upon removal of the driving voltage and becoming stuck against the fixed electrode. This common failure mode, known as stiction, results in device failure and poor reliability. One contributor to the reduction in stiffness would be the reduction in the elastic modulus (E) of the membrane material, which is the core motivation for this work. Mulloni et al. have shown the modulus decay effect on stiffness by monitoring the pull-down voltage with time,

Figure 1.3 [13]. They showed that after repeated switching cycles over many hours, it required less and less voltage to actuate the beam on and off.

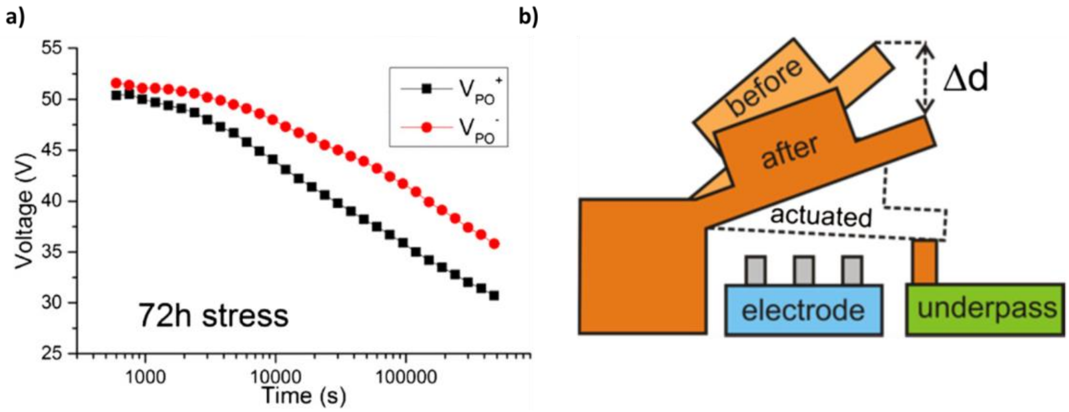

Figure 1.3 Implications of material degradation (modulus decay) with time in RF MEMS device: a) Voltage drop over time due to reduced stiffness b) implying a reduction in restoring force that affects gap distance [13]

The material properties of the moving components are therefore quite critical to overall metal MEMS device performance. There exists a knowledge gap in the material properties of many materials employed in MEMS devices, since many materials at very fine dimensions exhibit novel mechanical size effects where the properties vary significantly from the bulk. For instance high power sputtering of Ni-Mo-W alloys produced 29 μm films with highly-twinned columnar grains [14] where yield strengths measured near 3 GPa, much higher than conventional Ni-alloys. Similarly another group was able to produce LIGA-based (LIGA is a German acronym for Lithographie, Galvanoformung, and Abformung or Lithography, Electroplating, and Molding) Ni-W alloy materials with improved strength and ductility over pure Ni by alloying with 5 to 15% W and applying a high temperature annealing process [15]. Sub-micron thick metal films are especially prone to size effects, where one micropillar compression study showed Au having shear strengths approaching very high fractions of theoretical strength once the pillar diameter was reduced below about 700 nm [16]. It is therefore highly desirable to fill in the knowledge gaps in thin film properties, specifically sub-yield, viscoelastic behavior of metallic materials. Understanding this mechanical response subset will allow improved device designs and ultimately increase product reliability in real devices, such as the RF MEMS switch examples presented here.

1.3 Thin film properties

The definition of what makes a film a "thin film" can vary widely from group to group. Some groups consider a few atomic layers of material a thin film and would use specialized techniques such as molecular beam epitaxy [17] (MBE) or atomic layer deposition [18] (ALD) to grow precise atom-by-atom films. On the other end of the film thickness spectrum, the MEMS industry has developed an electroplating process to deposit 100's of μm of thin films into a highly precise lithographic mold (known as the LIGA process [19]). Many other physical and chemical deposition techniques were developed for applications in between these thickness extremes whose descriptions are beyond the scope of this effort. In the context of this work the important distinction needed to be classified as a thin film is when the film displays unique mechanical size effect phenomena that are not typically observed in bulk materials (or also thick films) of the same type. Specifically, under constant stress or strain conditions there is a more pronounced viscoelastic response in metal thin films than in bulk versions of the same material. This has application implications, such as the stiction failures in micro-machined devices as mentioned earlier.

1.3.1 Sputtering

Thin films can be deposited using a variety of techniques; sputter deposition is one of the most common among these for fabrication of metal films and is heavily used in the MEMS industry. Sputter deposition can be used to deposit both conducting (metallic) and non-conducting (oxides, ceramics) materials. The target material is bombarded with accelerated ions (typically Ar^+) which ejects atoms of the target species. Positive Ar ions are accelerated to the target by applying a large negative voltage to the target with a DC magnetron (or AC source if insulating material). A steady stream of bombarding ions against the target forms and fuels a plasma. The plasma reactions generate a plume of physical vapor of deposition material within the vacuum chamber. Film growth occurs when a substrate is placed in the line of sight of this vapor field. It is often rotated to minimize variations in thickness across the substrate. A schematic derived from [20] is shown in Figure 1.4a which depicts the north and south poles of the magnetron device as well as the relative placement of the substrate to the target. Figure 1.4b shows a Pt plasma formed using 150 W of DC current.

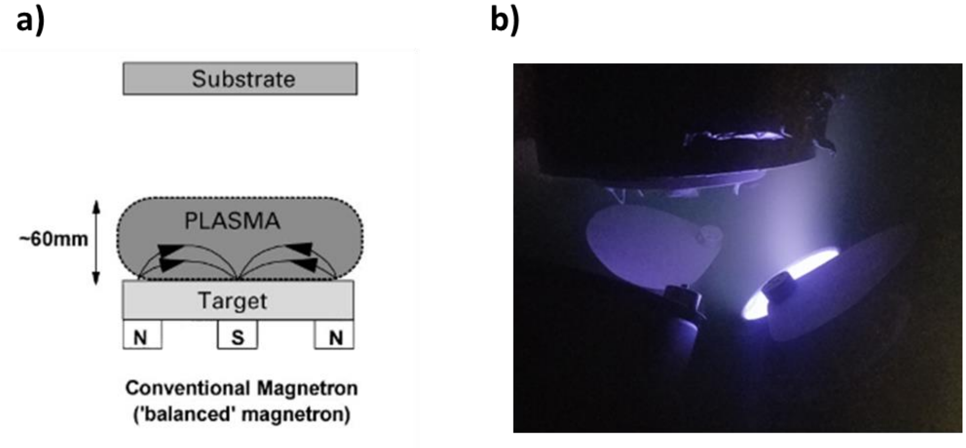

Figure 1.4 a) Schematic diagram of magnetron sputtering system [20] and b) example plasma formed from Pt target from this work

The sputter yield for a given Ar accelerating energy varies for different target materials as shown in Figure 1.5 [21]. The difference in yield for five FCC metals is highlighted in this figure. The yield for a given metal determines the film growth rate relative to deposition of other metals under identical conditions.

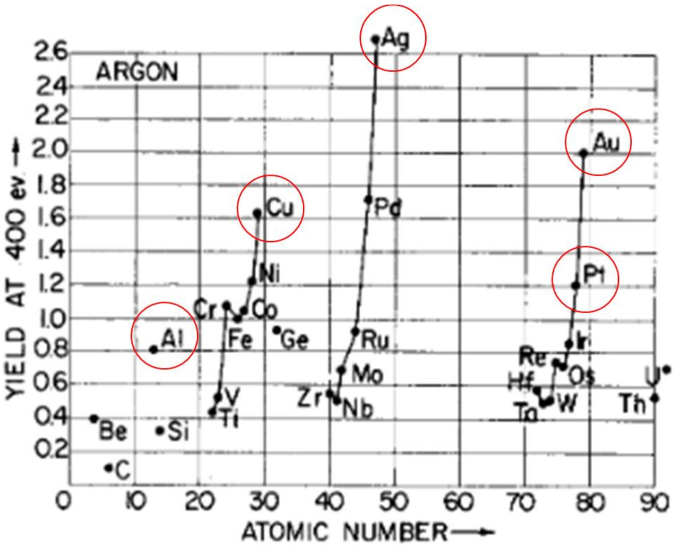

Figure 1.5 Sputter yield for metallic elements using Ar^+ bombardment [21]

1.3.2 Growth modes

Sputtered atoms from a target material become adatoms when they reach the substrate surface. These adatoms follow three general growth modes that depend on the affinity of the atoms to the substrate and other adatoms [22]: 1) Volmer-Weber (VW) isolated island growth when adatoms prefer bonding to other adatoms, 2) Frank-van der Merwe (FM) layer-by-layer growth where adatoms prefer bonding to the substrate, and 3) Stranski-Krastanov (SK) growth where a combination of island and layer-by-layer growth. Figure 1.6 depicts a combination growth mode common during the fabrication of polycrystalline metal films [23]. Coalescence and growth of adatom islands forms the typical columnar microstructure of metallic thin films.

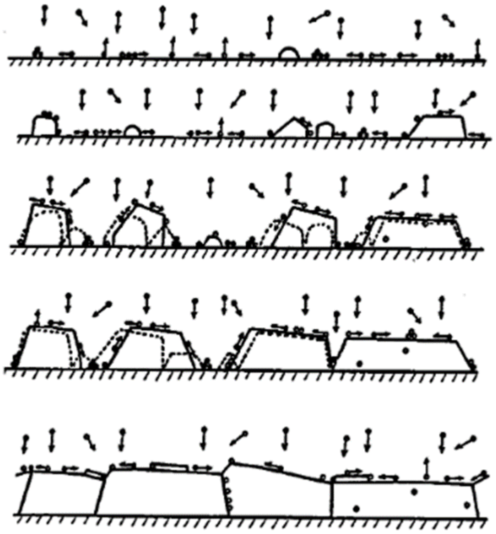

Figure 1.6 Example of film growth process showing island formation, coalescence of islands into continuous film, and film growth adapted from [23]

If the substrate is crystalline, an epitaxial relationship may develop in the growing film, creating a preferred film texture that depends on the orientation of the substrate. In contrast, an amorphous surface will not impart any preferred sites for adatoms during deposition. Without a preferred site for bonding, the adatoms will form crystallites which minimize surface and interfacial energies during coalescence and growth [24]. The lowest energy surface of FCC metals is the tightly packed (111) surface, which explains the (111)-fiber texture orientation that often appears during sputter deposition.

1.3.3 FCC material properties

A summary of material properties of importance to this work is presented in Table 1.1 [25,26]. The properties of the five face-centered cubic metals used for deposition are compared against silicon, the most common MEMS structural material.

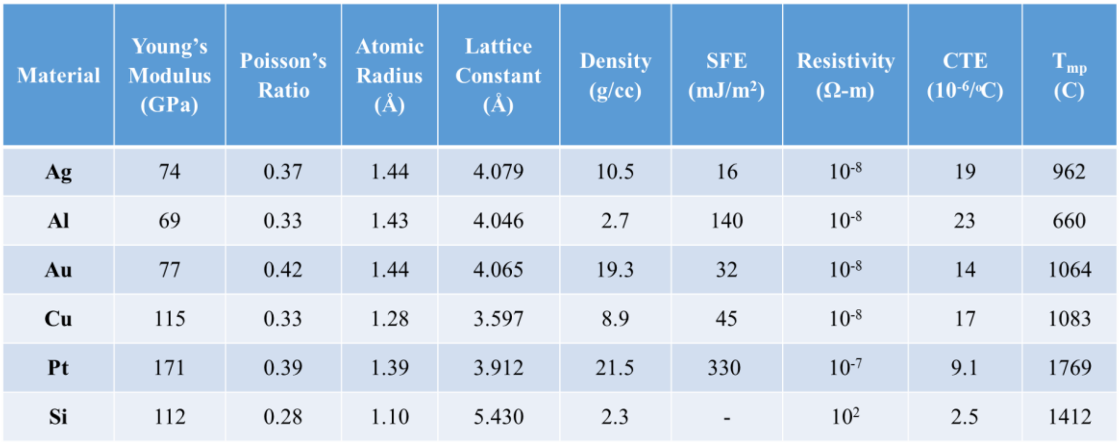

Material	Young's Modulus (GPa)	Poisson's Ratio	Atomic Radius (Å)	Lattice Constant (Å)	Density (g/cc)	SFE (mJ/m^2)	Resistivity (Ω-m)	CTE (10^{-6}/ºC)	T_{mp} (C)
Ag	74	0.37	1.44	4.079	10.5	16	10^{-8}	19	962
Al	69	0.33	1.43	4.046	2.7	140	10^{-8}	23	660
Au	77	0.42	1.44	4.065	19.3	32	10^{-8}	14	1064
Cu	115	0.33	1.28	3.597	8.9	45	10^{-8}	17	1083
Pt	171	0.39	1.39	3.912	21.5	330	10^{-7}	9.1	1769
Si	112	0.28	1.10	5.430	2.3	-	10^{2}	2.5	1412

Table 1.1 Selected material properties for materials used in this work

1.3.4 Thin film strengthening mechanisms

Accurate mechanical properties for thin films are needed for proper design of products and devices. Thin film materials generally exhibit size effect phenomena where the expected mechanical performance differs from bulk variants of the same material. The size effect is derived from the thin film microstructure developed during film growth. Thin films can be strengthened through a variety of dislocation interactions including with solutes (solid solution strengthening), precipitates (precipitation hardening), other dislocations (strain hardening), grain boundaries (Hall-Petch effect), and twin boundaries. Figure 1.7 depicts a schematic of these dislocation interactions with the obstacles listed above [27]. There is also an inherent resistance to dislocation motion, called lattice friction or Peierls force, that exists even in pure crystalline materials. For this work, three mechanisms will be highlighted: lattice friction, dislocation-dislocation interactions, and GB strengthening.

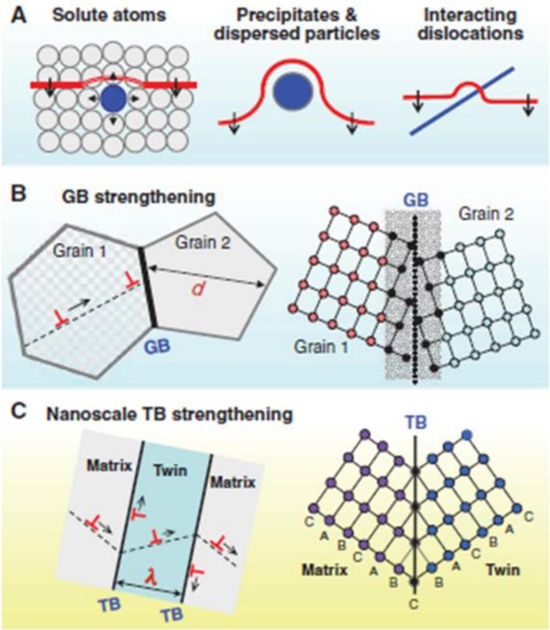

Figure 1.7 Schematic illustration of strengthening mechanisms in metals a) dislocation-obstacle interactions b) dislocation pile-up at grain boundary and c) dislocation-twin obstacle interaction [27]

Lattice friction comes from the periodic nature of a crystalline lattice. In order for a dislocation to advance, it must move from one stable location to another. The stable locations are energy troughs, and the intermediate position is an energy barrier that must be overcome. Ceramic materials have very high lattice friction at room temperature so dislocation motion is very difficult. Lattice friction in BCC metals is low enough that dislocation motion is relatively easy at room temperature, but not so low as to be negligible. Lattice friction in FCC metals is very low due to the presence of close-packed glide planes, so dislocation motion is very easy at room temperature. The lattice resistance in FCC metals is often ignored because other factors dominate the strength.

A strengthening mechanism important to thin films regardless of microstructure is the dislocation-dislocation interaction strengthening effect. The shear stress ($\Delta\tau$) required for dislocations to overcome the dislocation barrier as in the rightmost schematic of Figure 1.7a is given by:

$$\Delta\tau \propto Gb\sqrt{\rho} \quad \textbf{(1.5)}$$

Where G is the shear modulus, b is the burgers vector, and ρ is the dislocation density. A square root dependence on dislocation density was verified experimentally with single crystal Ag materials [28].

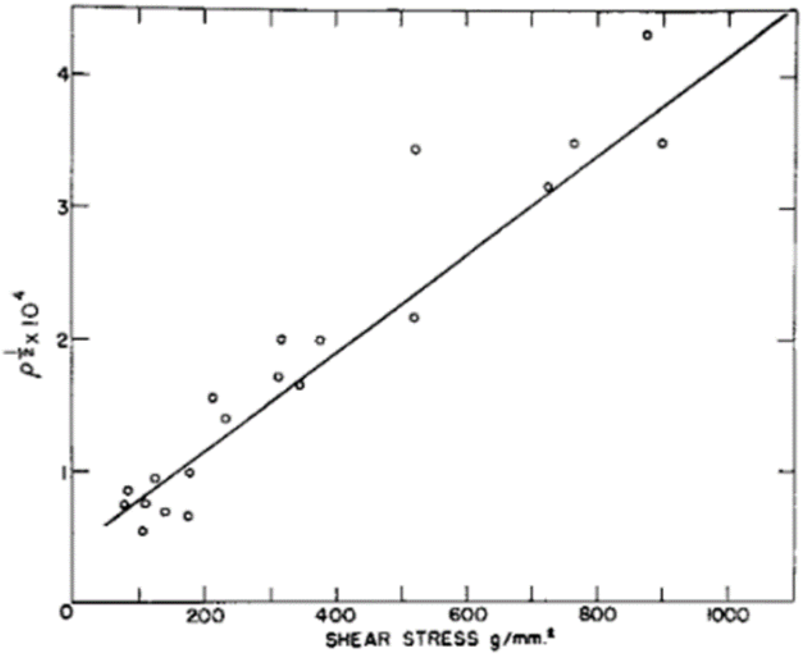

Figure 1.8 Square root dislocation density dependence on applied shear stress in single crystal Ag [28]

As described earlier, sputtered thin films typically form nanocrystalline or microcrystalline columnar grains from the substrate to the surface. This unique microstructure provides very small grain sizes, which can increase the strength of the thin film by increasing the density of grain boundary-dislocation interactions (Figure 1.7b). This strengthening mechanism follows a modified Hall-Petch behavior as follows [26,29]:

$$\sigma_{ys} = \sigma_T + \sigma_{ST} + k_y d^{-0.5} \tag{1.6}$$

Where the yield stress σ_{ys} is proportional to three separate length scales: 1) short term temperature-dependent Peierls lattice forces (σ_T) (< 1 nm), 2) long range athermal dislocation-obstacle stress effects (σ_{ST}) (10-100 nm), and 3) very long-range grain size effects ($k_y d^{-0.5}$) (> 1000 nm). A classical Hall-Petch relation was demonstrated in FCC metal films (Ag, Cu, Al, Ag-Cu) using microtensile testing [30].

1.4 Mechanical test techniques for thin films

The mechanical properties of thin films can be quite different from their bulk counterparts due to size effects of the miniaturized specimens. However, bulk mechanical test techniques do not translate well to measuring thin film properties. Therefore, specialized techniques were developed over the past few decades to characterize the unique mechanical properties of thin, planar materials. They include nanoindentation, substrate curvature measurement, MEMS microtensile tests, and bulge tests. These common thin film techniques will be summarized below.

1.4.1 Nanoindentation testing

Conventional microscale indenting techniques used on bulk materials provide a relative quick and inexpensive analysis of a material's hardness [31]. Instrumented indentation techniques, such as nanoindentation, are not limited to hardness alone. They have been developed to measure thin film properties [32] but with required considerations, most importantly being the necessary presence of a substrate. Hardness and modulus measurements in thin films can be affected by the substrate if the indenter penetrates more than 10% to 25% of the films surface [33]. Hence, special precautions in sample preparation and post-test data analysis are needed when nanoindenting on thin films where the film thickness is sub-micron. However, nanoindentation techniques are quite popular and can determine hardness, elastic modulus, residual stress, time-dependent behavior, and fracture toughness [32]. Figure 1.9 shows a nanoindenter schematic along with a typical load vs displacement (indentation depth) plot. Inspection of Figure 1.9b shows three parameters readily extracted from an indentation plot. Hardness is proportional to the load (P) divided by the indenter area (A):

$$H \propto \frac{P}{A} \tag{1.7}$$

Time-dependent creep response is measured by monitoring the indentation depth with a constant load. The indenter sinks into the material with a strain rate dependent on depth (h):

$$\dot{\varepsilon} = \frac{1}{h}\frac{dh}{dt} \tag{1.8}$$

During the unloading of the tip, the elastic springback of the material is proportional to the effective modulus (E_r) which is a combined modulus of both the thin film (E_s) and indenter (E_i) and their respective Poisson's ratios:

$$\frac{1}{E_r} = \frac{1-\nu_s^2}{E_s} + \frac{1-\nu_i^2}{E_i} \tag{1.9}$$

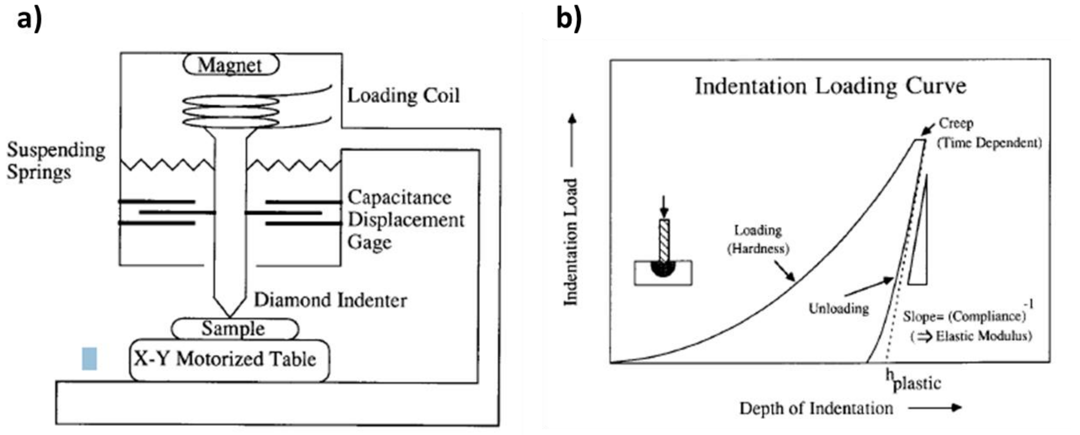

Figure 1.9 Nanoindentation test technique from [34] a) schematic of nanoindenter unit b) Load vs indentation depth with highlighted mechanical properties

Nanoindenting is a useful technique but comes with some concerns regarding overall thin film properties. By definition it is a site-specific, highly localized technique that can measure the properties of very small regions at a time. Therefore, an indent over a grain will measure different properties than an indentation on a grain boundary, for example. A user would need to average many indents across many different microstructural regions of the film to begin to quantify the mechanical properties of the complete film. In addition, the substrate effects mentioned earlier should be incorporated into each nanoindentation measurement, especially for relatively deep indents.

1.4.2 Wafer curvature testing

The Stoney equation was developed over a century ago to calculate the curvature induced by application of a stressed thin film over a relatively thicker substrate [35]. The technique allows determination of the biaxial stress state (σ_f) of the applied thin film by measuring the curvature before and after film deposition [36]:

$$\sigma_f t_f = \frac{E_s h^2}{6(1-\nu_s)R} \tag{1.10}$$

Where t_f is film thickness, E_s is substrate modulus, ν_s is Poisson's ratio of substrate, h is the substrate thickness, and R is the measured curvature after film deposition. This equation is a widely used technique to ascertain both tensile and compressive stress properties of the overlay film if a uniform coating is applied to a relatively smooth and flat substrate.

Heating up the film/substrate composite will change the stress state of the film and thus change the curvature. In-situ wafer curvature tests during thermal cycling can be used to monitor the biaxial stress state of the film with temperature in the following manner.

$$\Delta\sigma_f = \frac{E}{(1-\nu_f)}\Delta\alpha\Delta T \tag{1.11}$$

Where $\Delta\alpha$ is the difference in coefficient of thermal expansion for the film and substrate. Through monitoring of the stress conditions of a 1 μm thick, fine-grained (D ~ 0.1 μm) Cu film from 25 °C to 450 °C, Thouless et al. gained insight into the film's stress relaxation mechanisms during heating and cooling cycles [37]. The thermal cycle and measured stress state of this Cu film is shown in Figure 1.10 with suggested relaxation mechanisms within each stress-temperature regime.

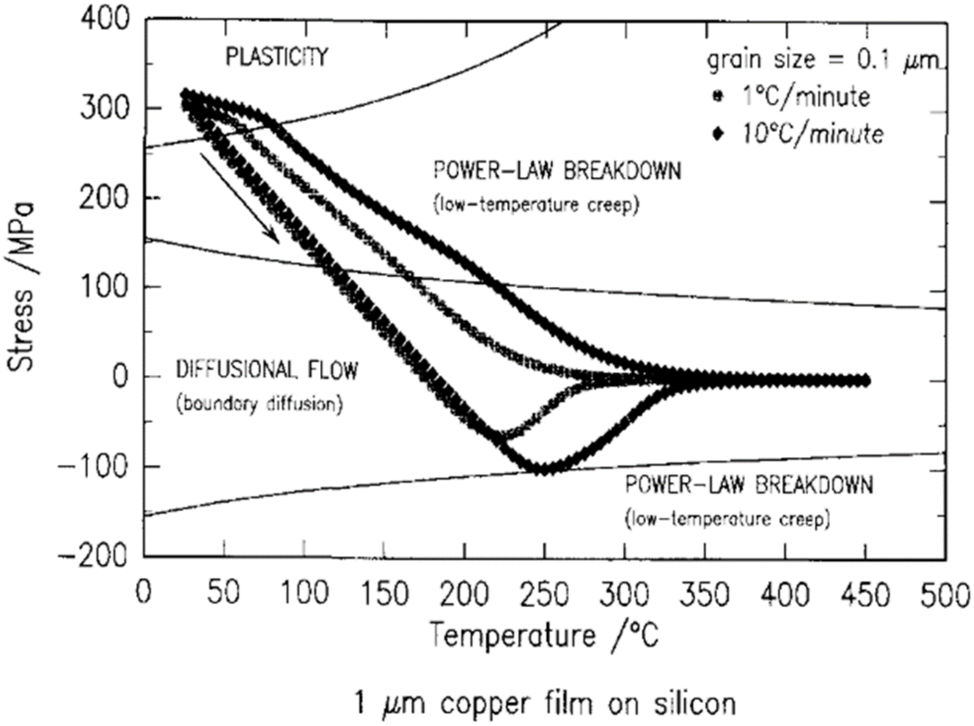

Figure 1.10 In-situ stress monitoring of Cu film during thermal cycling using the substrate curvature technique from [37]

One drawback of the wafer curvature technique is the inability to de-couple thermal strains from mechanical strains, as evidenced directly in Figure 1.10. Independent contributions from applied stress and temperature on the stress state of the film are impossible with this technique.

1.4.3 SEM/TEM in-situ microtensile testing

Monitoring the deformation process in real time is routine for bulk samples using conventional uniaxial mechanical testers and digital image correlation (DIC) strain analysis. In-situ, micro- and nano-scale monitoring of thin film deformation is not nearly as widespread, but is becoming more prevalent with the advent of MEMS-based mechanical testing platforms [38–40]. The thin film under investigation is usually co-fabricated as a tensile coupon with the standard silicon-based MEMS micromachining operations necessary to create the test platform. This prevents specimen damage during mounting using more traditional techniques. In addition, the highly precise lithographic process for machining the MEMS components allows for excellent alignment and sample gripping. An example micro-tensile tester is shown in Figure 1.11a where the specimen is co-fabricated with the MEMS platform [40]. Example SEM and TEM in-situ mountings are shown in Figure 1.11b and c, respectively.

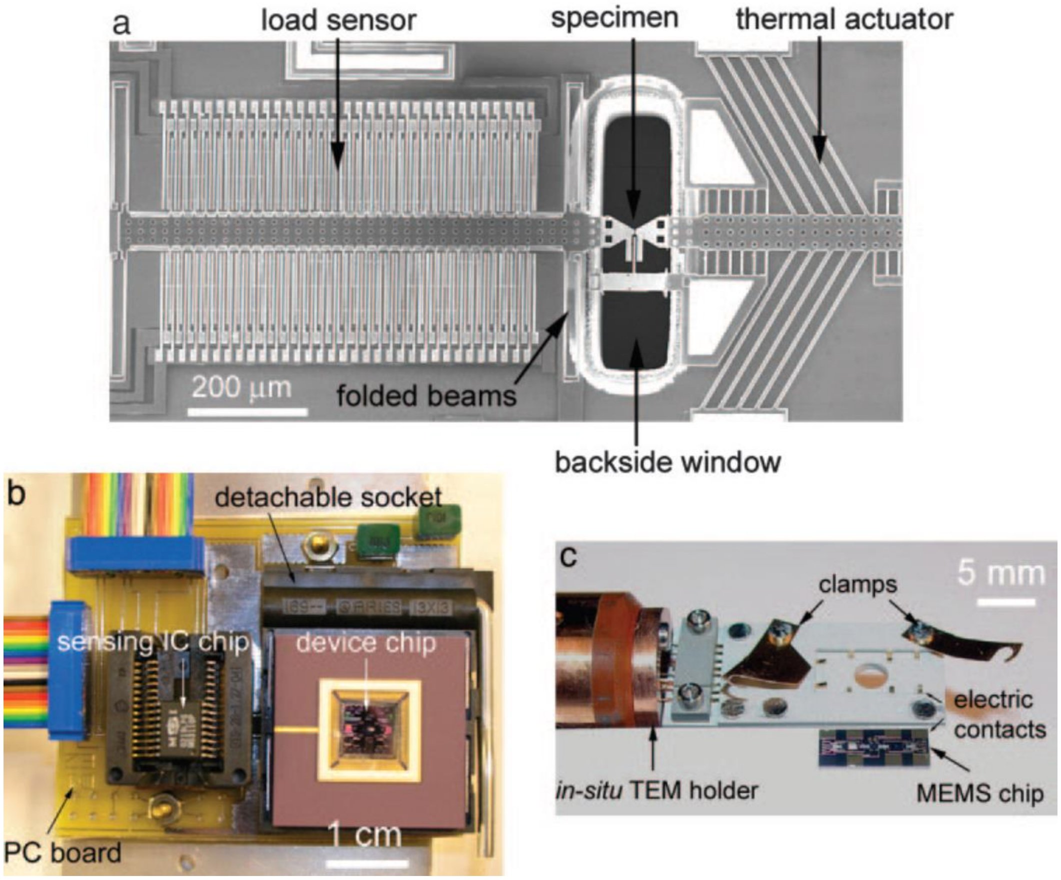

Figure 1.11 In-situ MEMS platform for thin film microtensile tests [40] a) MEMS testing device b) SEM in-situ mount and c) TEM in-situ mount

1.4.4 Bulge testing

The bulge test technique is used in this present work to measure the anelastic properties of metallic thin films. The technique works by applying a pressure to one side of the film which generates a deflection or bulge [41–43]. The bulged film's applied pressure and deflection height are converted into stress-strain data. The deflection can be measured capacitively if the film is conductive [6,7] or optically using a laser interferometer [44,45]. The bulge technique requires the film composite to be in a state of tension, as a compressive or buckled film cannot be easily measured through capacitance or optical methods. One advantage of this technique is that it is possible to test free-standing metal films, which is not possible with many conventional thin film measurement techniques, such as nanoindentation. Another advantage of the bulge technique is the de-coupling of thermal strains from mechanical strains, which is inherently impossible with substrate curvature techniques. Finally, the bulge specimen is much simpler and easier to handle than a microtensile test specimen. More details of the specifics of this technique are in Chapter 2.

1.5 Time-dependent recoverable deformation in thin films

A non-instantaneous (i.e., time-dependent) deformation response to the application of a load is the core focus of this work. Time-dependent deformation processes can be broadly classified into two categories: 1) creep deformation under constant stress that causes a gradual increase in strain and 2) stress relaxation under constant strain that causes a gradual decrease in stress in the material. In bulk materials these deformation processes are predominantly permanent and tend to occur at high temperatures (e.g., $\approx T > 0.5\ T_m$). In thin film materials, these processes can have a pronounced effect on material performance even at low temperatures, such as the reduction in springback force in an RF MEMS cantilever operating below 100 °C.

1.5.1 Commonly proposed mechanisms for time-dependent deformation

Crystalline material deformation can be controlled by a variety of mechanisms depending on the stress, strain rate, and temperature environment during deformation.

Plastic flow is thought of as a kinetic process determined by the density and flow velocity of "deformation carriers". Deformation carriers include gliding dislocations, diffusion of atoms within the grain or grain boundary, grain boundaries sliding, and mechanical twinning [46]. A collection of deformation mechanism maps are available in the literature that indicate what type of mechanism will dominate depending on the applied stress, temperature or strain rate [46,47]. For example, Figure 1.12 presents the expected deformation mechanisms in bulk pure Ag, with Figure 1.12b and c showing the adjustment and extension of mechanism zones after altering the dislocation density and grain size, respectively. For reference, the bulge testing conditions presented later in this study reside in the sub-yield (i.e. elastic) boxed region of these figures. The boxed region was placed based on an applied shear stress of 50 MPa, assuming a Ag shear modulus of 26.4 GPa, and bulge test temperature of 80 °C.

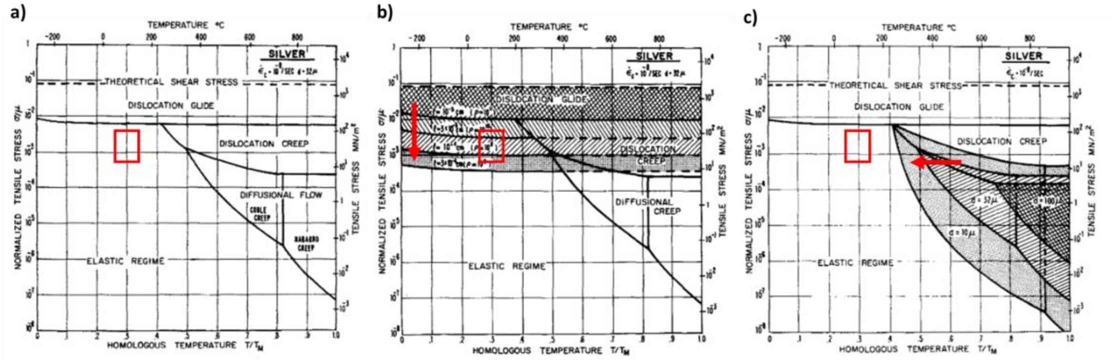

Figure 1.12 Deformation mechanism maps from [47] of a) pure Ag b) pure Ag with dislocation density effect and c) pure Ag with grain size effect. Red boxed area represents typical environment of bulge anelastic test

1.5.1.1 Low-temperature plasticity by dislocation glide

Low-temperature deformation processes in metals are dominated by slip and twinning. Face-centered cubic metals generally deform by dislocation-based slip processes with mechanical twinning generally occurring only at very low temperatures. The dislocation movement can be hindered by obstacles such as solutes, precipitates, grain boundaries, and other dislocations. This hindering effect strengthens the material by pinning dislocations at obstacles and preventing further slip deformation. Various strengths or activation energies (ΔF) of obstacles are listed in Table 1.2 [46]. In this table b is the Burgers' vector, μ is the shear modulus, l is the dislocation spacing, and $\hat{\tau}$ is the shear strength without thermal contributions.

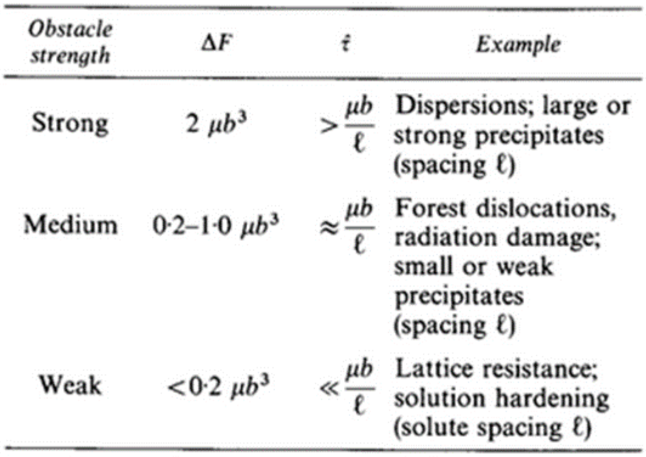

Obstacle strength	ΔF	$\hat{\tau}$	*Example*
Strong	$2\ \mu b^3$	$> \frac{\mu b}{\ell}$	Dispersions; large or strong precipitates (spacing ℓ)
Medium	$0{\cdot}2$–$1{\cdot}0\ \mu b^3$	$\approx \frac{\mu b}{\ell}$	Forest dislocations, radiation damage; small or weak precipitates (spacing ℓ)
Weak	$<0{\cdot}2\ \mu b^3$	$\ll \frac{\mu b}{\ell}$	Lattice resistance; solution hardening (solute spacing ℓ)

Table 1.2 Characteristics of obstacles from [46]

The strain rate ($\dot{\gamma}$) from dislocation-obstacle interaction is given as [46]:

$$\dot{\gamma} = \dot{\gamma}_0 \exp\left[\frac{-\Delta F}{kT}\left(1-\frac{\sigma_s}{\hat{\tau}}\right)\right] \qquad \textbf{(1.12)}$$

Discrete obstacles such as precipitates or other dislocations will provide high energy barriers to dislocation movements and/or bowing. Lattice resistance (Peierls force) also provides a friction for dislocation movement, but to a smaller extent. Figure 1.13a and b depict dislocation movements against higher barrier discrete obstacles and lower barrier lattice resistance, respectively [46]. Deformation by these low temperature mechanisms is typically assumed to be instantaneous and non-recoverable in bulk metals.

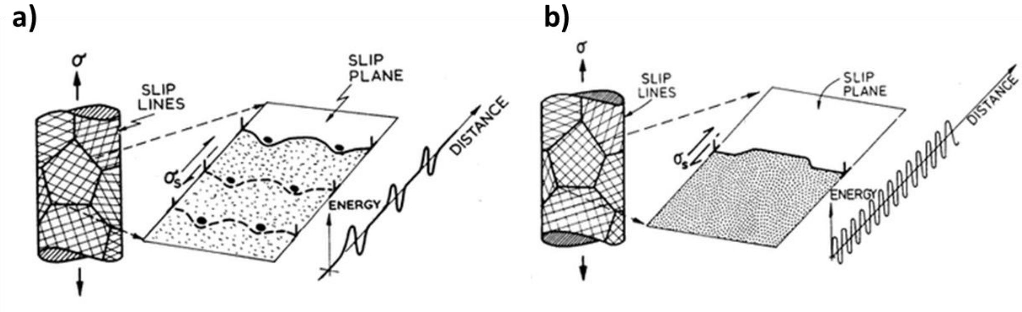

Figure 1.13 Low-temperature obstacles for dislocation motion a) discrete obstacles and b) Peierls lattice resistance [46]

1.5.1.2 Power-law creep by dislocation glide or glide-plus-climb

At higher temperatures (~ T > 0.3 T_m), many bulk metals exhibit time-dependent, non-recoverable power-law creep that follows [46]:

$$\dot{\gamma} \propto \left(\frac{\sigma_s}{\mu}\right)^n \tag{1.13}$$

where n has a value between 3 and 10. Via this deformation mechanism dislocations can propagate by glide and glide plus climb. Dislocations have enough energy to climb over obstacles through the process of vacancy diffusion. The glide plus climb process is considered "high-temperature" creep when lattice diffusion provides the driving force for climb and "low-temperature" when dislocation core diffusion drives the climb operation. This process can occur in thin films as well. During high temperature wafer curvature tests (between 180 °C and 400 °C), Hwang et al. determined a power-law creep mechanism was driving the deformation in stress relaxation experiments on 1 μm thick Cu films [48].

1.5.1.3 Diffusional flow

At even higher temperatures, atomic diffusion processes begin to control the time-dependent deformation rate in response to an external stress. Diffusion-controlled deformation is either dominated by lattice or grain boundary diffusion depending on the temperature. In both cases the strain rate is proportional to the grain size (D). At lower temperatures, grain boundary diffusion or Coble creep is given as [26,49]:

$$\dot{\gamma} \approx \frac{50\sigma D_{gb} b^4}{kTD^3} \quad \textbf{(1.14)}$$

Where D_{gb} is the diffusivity constant in the grain boundary, D is the grain size, b is the Burgers vector, k is the Boltzmann constant. At higher temperatures, lattice-based diffusion, or Nabarro-Herring creep, dominates the deformation as:

$$\dot{\gamma} \approx \frac{7\sigma D_v b^3}{kTD^2} \quad \textbf{(1.15)}$$

Where D_v is the diffusivity constant through the lattice. Grain boundary diffusion mechanisms are more prevalent in fine-grained materials, as noted by the increased grain size sensitivity in Coble creep strain rates (D^3 vs D^2). A model showing both lattice and boundary diffusional responses during high temperature deformation is shown in Figure 1.14[46].

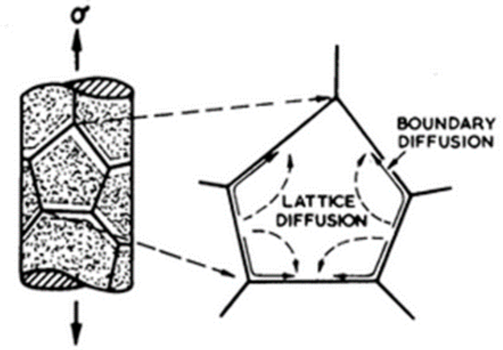

Figure 1.14 Diffusional deformation model showing Coble creep (boundary diffusion) and Nabarro-Herring creep (lattice diffusion) [46]

1.5.1.4 Grain boundary sliding

For many thin film experiments, grain boundary sliding has been proposed as the likely time-dependent deformation mechanism [50]. This is not a pure mechanism in its own right but requires accommodation mechanisms such as diffusional flow or dislocation climb [26]. As described previously these two base mechanisms are fundamentally high temperature processes, so in bulk materials grain boundary sliding would be expected only in high temperature deformation environments. However, in nanocrystalline material experiments ($D \approx 10$ to 50 nm) [51–57], low temperature (~ room temperature) grain boundary sliding has been attributed to time-dependent deformation. The increased volume of grain boundaries in these ultrafine nanocrystalline materials has also been attributed to the inverse Hall-Petch effect where the materials weakens with further reduction in grain size.

1.5.2 Recoverable thin film deformation

In thin films, significant recovery of deformation due to creep and stress relaxation have been reported, both anelastic recovery [6,7,58] and plastic recovery [59,60]. The distinction between low-strain anelastic recovery and high-strain plastic recovery is depicted in Figure 1.15. The focus of this work is anelastic or viscoelastic recovery (blue curve, regime ii), where the film is deforming in ‘sub-yield’ conditions. In contrast, a plastic recovery processes (red curve, regime i) are shown as time-dependent recovery of yielded thin films. The following sections will present work in each regime and some of the proposed mechanisms that drive each recovery process, highlighting the differences between instantaneous and non-instantaneous mechanical responses possible in thin films [61].

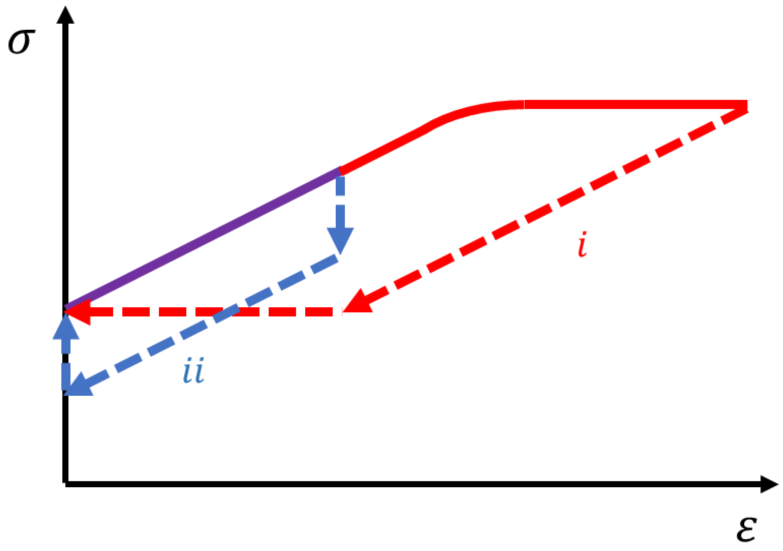

Figure 1.15 Thin film recovery processes showing i) plastic recovery and ii) anelastic or viscoelastic recovery (stress relaxation experiment)

	Recoverable	Instantaneous	Linear
Instantaneous elasticity	Yes	Yes	Yes
Instantaneous plasticity	No	Yes	No
Anelasticity	Yes	No	Yes
Recoverable plasticity	Yes	No	No

Table 1.3 Different types of mechanical behavior

1.5.2.1 High-strain time-dependence (recoverable plasticity)

Recent work in the field of nanocrystalline materials regarding the time-dependent plastic mechanical behavior has led to competing theories describing the deformation mechanism including both recoverable and irrecoverable processes. Rajagopalan et al. found 50 to 100% plastic recovery of Au and Al sub-micron thin films using a MEMS tensile testing technique [59]. The effect was only seen in nanocrystalline films with grain sizes in the 50 - 65 nm regime and was not present in larger-grained films of the same overall thickness. This work argues that the films contained an inhomogeneous distribution of grain sizes whereby an applied global stress will only generate dislocations in the larger grains at grain boundary sources, causing plastic deformation. The smaller grains will be void of dislocation formation and propagation and only elastically deform from the global strain. Recovery is driven by leftover residual internal stresses due to inhomogeneous deformation. It is suggested that the resultant backstresses force dislocations back to their origin upon removal of the external load.

An alternative investigation into nanocrystalline copper films by Ghazi found similar plastic recovery phenomenon in films containing roughly 35 nm grain sizes [62]. Using the bulge test technique, they found that the recovery from plastically-deformed films demonstrated both a fast and a slow recovery rate upon removal of stress. Unlike the previous dislocation-based mechanism for recovery, they postulate a diffusion-based mechanism is responsible for driving the recovery process. In their model this diffusion is due to Coble creep of atoms from grain boundaries to pores within the sputtered copper film. However, similar to the Rajagopalan work, the driving force for recovery or reversing the Coble creep is postulated to be inhomogeneous buildup of residual stress within the film grain structure.

1.5.2.2 Low-strain time-dependence (anelasticity)

Low-strain anelasticity is time-dependent deformation that has no permanent set or plasticity. During a constant strain test, an anelastic material will exhibit stress relaxation, but upon removal of the strain the material will recover with time as depicted in the right portion of Figure 1.16.

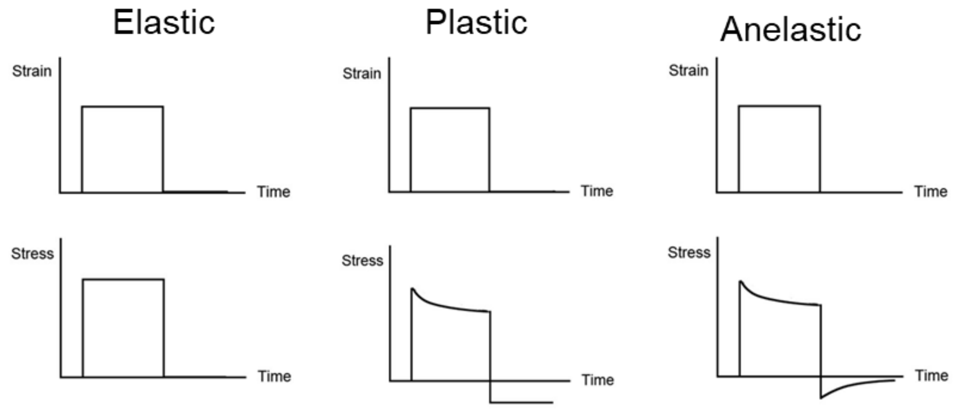

Figure 1.16 Elastic, plastic (viscoplastic), and anelastic response to a constant strain

A mechanical analog of an anelastic material is one which has an instantaneous strain due to the applied stress represented by a spring in series with time-dependent deformation represented by a spring-plus-dashpot. Figure 1.17 represents this analog of a sputtered metal film on a purely elastic substrate [63]. This analog is representative of the bulge testing presented here, where samples are composed of anelastic metal films adhered to purely elastic SiN_x substrates.

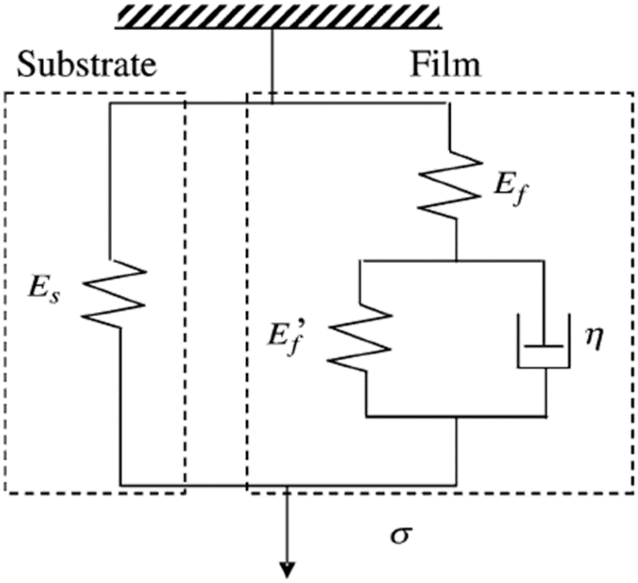

Figure 1.17 Mechanical analog of anelastic deformation of a substrate and metal film [63]

Examples of time-dependent recoverable plastic deformation in section 1.5.2.1 described metal thin films strained beyond the yield point and the associated observations of full plastic recovery. Although important for furthering the understanding of small-scale viscoplastic behavior, a MEMS designer is unlikely to design a component that exceeds the practical elastic limit. From a pragmatic viewpoint that means the low-strain, anelastic or viscoelastic time-dependent behavior is more important for real world devices, including RF MEMS chips.

Anelastic recovery was studied in Al-(1 wt%) Cu thin films with strains from 0.05% to 0.8% [58]. Using both microbeam bending and micro tensile tests (Figure 1.18a and c, respectively), they could measure recoverable creep strain as shown respectively in Figure 1.18d. Upon removal of the stress the beam recovers most of the bending strain after over 3 hours of rest, Figure 1.18c. The recovery process is not attributed to inhomogeneous distribution of strain as hypothesized in the prior high-strain recovery examples, but more to backstresses generated during extension of existing dislocation line segments. Although their work was on thicker films (~5 um) and larger grains (4 – 20 um), they could show that the presence of grain boundaries had negligible effect on the extent of anelastic recovery.

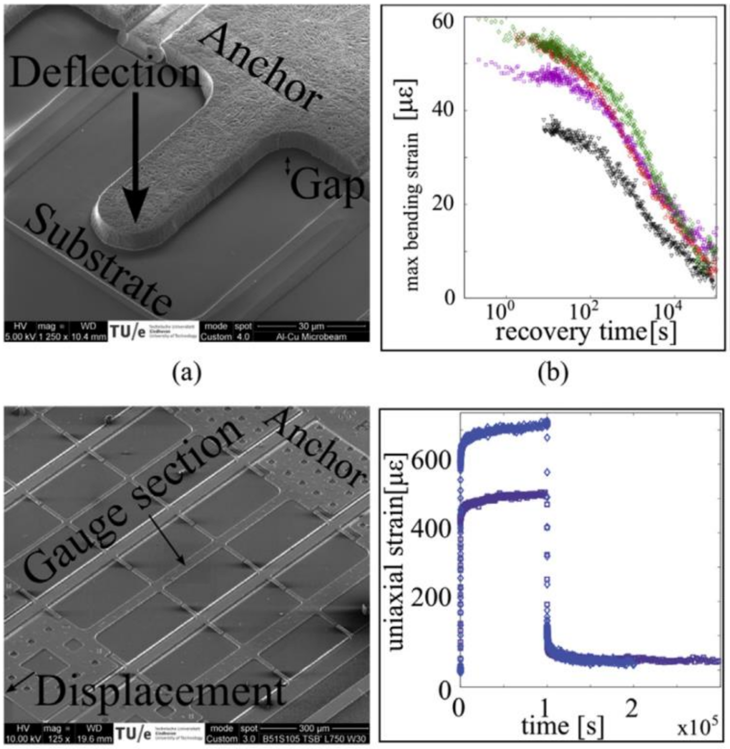

(a) (b)

(c) (d)

Figure 1.18 Low-strain anelastic recovery of Al-Cu microbeams

An alternative theory for describing the anelastic recovery in low-strain environments was presented by Kalkman et al. where they utilized a dynamic bulge test to measure the time-dependent mechanical response of sub-micron W, Al, and Au films [51]. They found the W film exhibited no time-dependent behavior across testable frequencies while Al and Au films showed considerable modulus decay as the frequency of oscillations was reduced. Based on the characteristic time constant measured for Al and Au thin films they suggest grain boundary sliding as the dominant mechanism driving the anelastic behavior. The very small grain size of the measured films account for the significant contribution of grain boundary sliding even if this mechanism is more typically found at high temperatures in bulk materials.

Early work in our group measuring low-strain anelastic behavior in FCC Au films attributed the effect primarily due to so-called “pre-yield microplasticity.” Experimental studies have shown that dislocations begin moving at relatively low shear stresses (10^{-6} to 10^{-5} of the shear modulus, G), where they still have enough energy to overcome the Peierls energy barrier [64]. The observed stress relaxation in gold thin films was attributed to a double kink dislocation propagation mechanism, due to the similarities in calculated activation energies with the literature (0.1 to 0.2 eV for FCC metals) [8].

In internal friction experiments, Choi and Nix also suggest a dislocation-based process is driving the anelastic recovery of Cu thin films [63]. Measured activation energies of 1.47 eV suggest the dislocation bowing and extension process is limited by jog drag and vacancy diffusion. Recovery is driven by built-up dislocation line tension in the bowed dislocations.

1.5.2.3 Anelastic dislocation bowing

Anelastic processes observed in this work require a non-permanent (i.e. recoverable) dislocation-based mechanism to describe the deformation. Many of the bulk plasticity mechanisms discussed previously are unlikely candidates because they do not result in stored elastic energy that can drive reversibility. Bowing of a pinned dislocation, however, meets this criterion. Consider a dislocation pinned by two obstacles (A and B) as in Figure 1.19 that can bow in response to sub-yield stresses. If the dislocation bows beyond a certain critical radius it becomes unstable and either breaks away from the pinning points or becomes a Frank-Read source. However, if the radius is small then the line will retract once the applied stress is removed, fully recovering the strain.

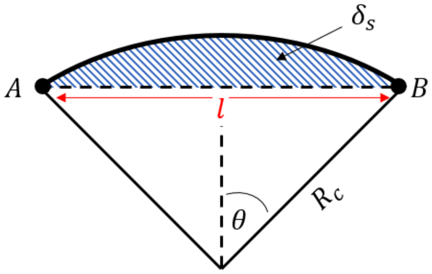

Figure 1.19 Bowing dislocation from pinning point A to B under applied stress

The bowing extent is related to the curvature of the dislocation line (R_c), the shear modulus (G), the burgers vector b, and the applied shear stress:

$$R_c = \frac{1}{2}\frac{Gb}{\sigma} \tag{1.16}$$

The dislocation sweeps across an area δ_s that is dependent on the unloaded pinning distance (l) between points A and B:

$$\delta_s = \frac{1}{12}\frac{l^3}{R_c} \tag{1.17}$$

The anelastic strain developed in the material is proportional to the number of bowing dislocations per volume (N_v), the swept area, and the Burgers vector:

$$\varepsilon = b\delta_s N_v \tag{1.18}$$

The shear modulus (G) decay due to dislocation bowing is then proportional to the dislocation density (ρ) and the pinning distance (l) by [61]:

$$\frac{\Delta G}{G} = \frac{1}{6}\rho l^2 \tag{1.19}$$

This modulus decay is also equivalent to the number of dislocations per unit volume (N) and the cube of the pinned distance (where α is near unity) [65]:

$$\frac{\Delta G}{G} = \frac{-Nl^3}{6\alpha} \tag{1.20}$$

A bowing dislocation generates a backtension (τ) which can be responsible for anelastic recovery of strained materials upon unloading [66]:

$$\tau = \frac{Gb}{2R_c} \tag{1.21}$$

Time- and temperature-dependence are provided by the Peierl's barrier that the bowing dislocation must overcome.

2. Experimental details

This chapter describes the fabrication, characterization and mechanical test techniques used to study the viscoelastic properties of metallic thin films. The first portion describes the creation of a standard test sample used in this research, including the geometry and composition of the substrate. Second, the deposition process used to grow thin films upon this substrate is described. Next there will be a discussion of the laboratory techniques used to characterize the microstructural features of each thin film test sample. Finally, a summary of the mechanical test technique, the bulge test, will be provided. All time-dependent, viscoelastic test results presented in the subsequent chapters used the same experiment set up detailed in this chapter.

2.1 Sample design and fabrication

The bulge test sample is extracted as a die from a (100)-oriented silicon wafer. This wafer is 525 μm thick with 200 nm of SiN_x on the top and back side of the wafer. The SiN_x is amorphous and acts as both a deposition substrate and wet etch stop. Silson Ltd (www.silson.com) provided the wafers pre-coated with SiN_x using Low Pressure Chemical Vapor Deposition (LPCVD), see Figure 2.1. The back-side SiN_x coating was masked off to allow exposure of a rectangular silicon region during the Potassium Hydroxide (KOH) wet etching process. The masking process delineated the rectangular cavities needed to generate the thin bulge membrane and also score lines to allow for easy separation into square dies. The wafer was approximately 4 inches in diameter (100 mm), with twelve 20 mm by 20 mm dies on each wafer. KOH etching of Si is an anisotropic process that exposes the {111} planes that lie at an angle to the surface of a (100) wafer. The rectangular mask was therefore oversized in such a way to generate a 12 mm by 3 mm SiN_x membrane on the front side of the wafer at the end of the KOH etch process. The oversize was calculated to account for the 54.74° anisotropic etch angle of single crystal silicon and the 525 µm wafer thickness.

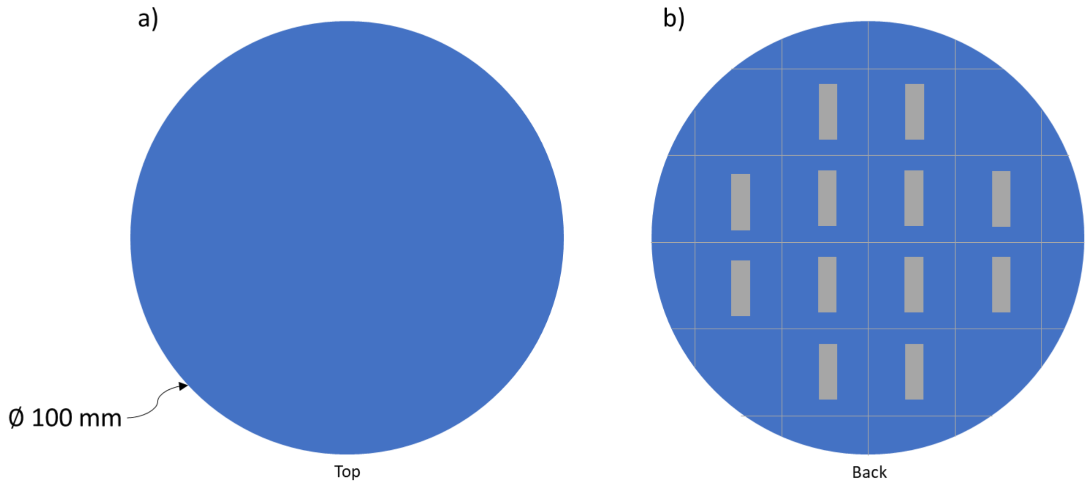

Figure 2.1 Si wafer for bulge test samples with a) full SiN_x coating on the top side and b) masked SiN_x coating on the back side

The crisscrossing score lines shown in Figure 2.1b are used to break the wafer into bulge dies. The dies (or alternatively as a whole wafer) are submerged in a 50:50 solution of deionized water and KOH at 80 °C. At this temperature and etchant concentration the exposed silicon is shown to etch at approximately 1 µm/min in the (100) direction [67,68]. Therefore, a complete etch of 525 µm thick exposed silicon wafer would take about 8.75 hrs. For this research, a whole wafer was typically submerged for ~ 16 hours which resulted in complete etching of the exposed rectangular silicon and negligible removal of the SiN_x etch stop. After removing the wafer from the KOH mixture, it was submerged in a bath of de-ionized water to remove any KOH residue and to clean the surfaces of any potassium salts that came out of solution. Careful handling is required as the 12 mm by 3 mm free standing SiN_x membrane is only 200 nm thick and extremely fragile from this point forward. Figure 2.2a-b represents this wet etching process after dies are removed from the wafer. Relevant bulge sample dimensions used for this research can be extracted from this figure. This process creates the SiN_x membrane that will be the substrate for film deposition, Figure 2.2c and Section 2.2.

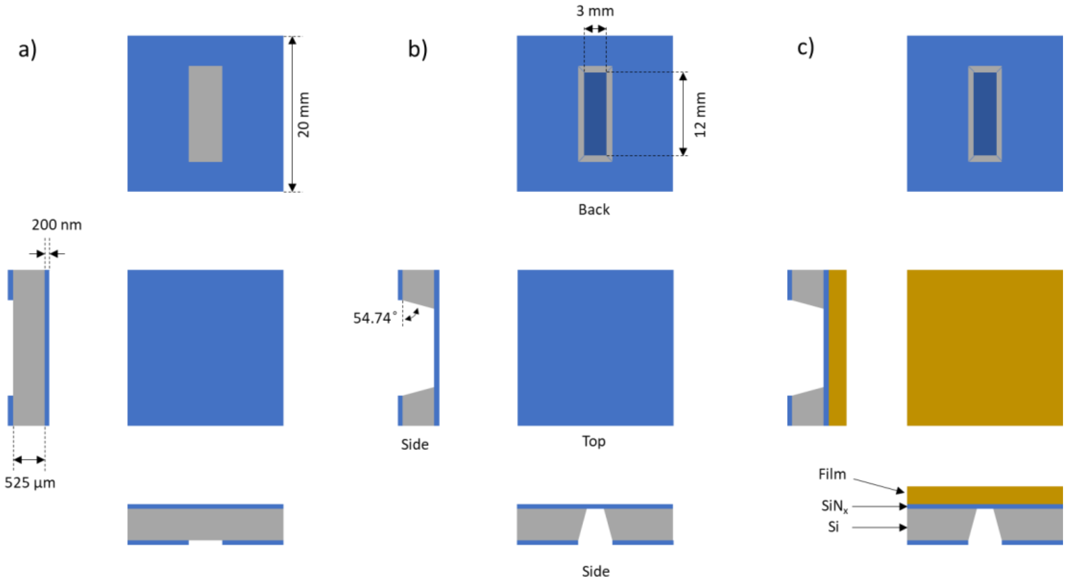

Figure 2.2 Bulge test samples a) as-diced b) as-etched c) as-coated

In some cases, the silicon backing was not completely etched away to allow for epitaxial growth of single crystal metal films on a silicon substrate (see Section 2.2.3). In this special case, a drop gauge was used to estimate the remnant silicon backing after submersion in the KOH:H_2O mixture. After sufficient etching in KOH, Reactive Ion Etching (RIE) dry etching techniques were used to remove the wet etch-resistant SiN_x on the top side. Using a Technics 800 RIE with a mixture of O_2 and CF_4 gas and an RF plasma, it was possible to remove the amorphous SiN_x layer without damaging the underlying silicon. In this way a free-standing silicon membrane could be used to allow metal to deposit directly onto a (100) Si surface, instead of the conventional amorphous SiN_x surface which was used for most of this research.

2.2 Thin film deposition process

The following sections will detail the PVD sputtering conditions to fabricate bulge samples for viscoelastic testing. A discussion of adhesion layers and why they were not used in this study will be provided. Then highlights of the polycrystalline films deposited at Lehigh will be presented, followed by details of a single crystal film grown by the Max Plank Institute for Intelligent Systems of Stuttgart, Germany.

2.2.1 Adhesion layers

An adhesion layer is commonly used to help one thin film material attach to a substrate material where it might have difficultly adhering without the presence of this intermediary adhesion layer. Highly reactive species such as Ti and Cr are routinely used as adhesion layers between substrate and metal film, with thicknesses from a few nm up to many tens of nm depending on the application. Studies on adhesion performance have typically been done by testing the fracture strength of the film composites, where the energy to form a crack between the overlayer and the substrate is determined [69,70]. In addition an adhesion layer can be used as a diffusion barrier between substrate and overlayer metal [71]. Researchers have found unwanted device performance in multilayer memristor switch devices when the Ti adhesion layer diffused through the metallic overlayer contact, corrupting device performance [72]. Although typically much thinner than the overlayer film, the adhesion layer can alter the mechanical and chemical state of the film composite, thus film deposition can require special considerations.

For this study at Lehigh, an adhesion layer was not used. All metal films were deposited directly onto the SiN_x substrate without an intermediary layer. There are two primary reasons for this: 1) An adhesion layer (Ti or Cr) would likely diffuse through the metal structure during the high temperatures needed for grain growth and 2) the presence of an adhesion layer tended to prevent or alter the columnar growth of metal grains during growth. Figure 2.3a shows a representative cross section of films used in this study (with green representing adhesion layer), with columnar growth from substrate-to-surface with no adhesion layer present between film and SiN_x. Unwanted growth conditions such as interruption of grain columns or diffusion of adhesion layer species through grain boundaries are shown in Figure 2.3b and c, respectively.

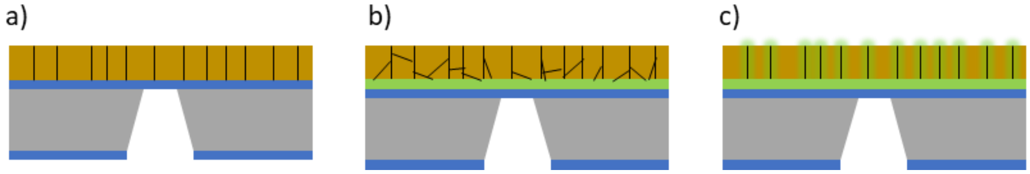

Figure 2.3 Schematic effect of adhesion layer a) none b) non-columnar growth c) GB diffusion

A core facet of this work is studying the grain size dependence of viscoelastic properties of thin metallic films and the presence of diffuse Ti/Cr atoms or the irregular grain growth due to the adhesion layer's presence would introduce unwanted variables.

2.2.2 Polycrystalline film growth

Metallic, polycrystalline films were deposited with a Direct Current (DC) magnetron sputtering chamber (AJA International ATC 2200 Sputtering System). This sputtering chamber has three 2'' sputter guns that can be aimed at a centrally-located substrate. Typical base pressures reached by the vacuum system are 10^{-7} to 10^{-8} torr. Substrate rotation during sputtering was set at 21.37 rotations per minute for all samples. The sputter gas used was high purity Ar gas with a standard process pressure of 5 millitorr (10^{-3} torr). The deposition rate was controlled by adjusting the power applied to the sputter gun, which was typically set in the range of 150 to 300 W for all metals. Sample substrate bias was not used for any film deposition in this study. Elevated substrate temperature was provided by a halogen lamp heater with feedback control provided by the sputter system heating unit (AJA International model SHQ 2001-C). Sputter rates were calculated by measuring film thickness (see Section 2.3.1) after a set amount of time. A summary of process conditions is shown in Table 2.1.

Material	Target (2")	Power (W)	T (°C)	RPM	Bias (V)	Base Pressure (torr)	Process Pressure (torr)	Sputter Gas	Height (in)	Gun Angle (°)	Thickness (nm)	Rate (nm/s)
Ag	99.99% Ag	150	100 125 150 175 200	21	none	10^{-8}	10^{-3}	Ar	4	61.3	500	0.9
Al-(< 1 wt%) Mg	99.999%(Al) 99.99% (Al 95.5- Mg 4.5)	300 300	100 150 200	21	none	10^{-8}	10^{-3}	Ar	4	61.3	500	0.233
Au	99.999% Au	150	100 175 300 400	21	none	10^{-8}	10^{-3}	Ar	4	61.3	670	0.833
Cu	99.999% Cu	150	100 200 300	21	none	10^{-8}	10^{-3}	Ar	4	61.3	500	0.37
Pt	99.99% Pt	150	150 200 300 500	21	none	10^{-8}	10^{-3}	Ar	4	61.3	500	0.423

Table 2.1 Sputter process conditions

If required, the bulge sample dies described in Section 2.1 were cleaned before loading into the chamber with common laboratory solvents such as acetone, isopropyl alcohol, and methyl alcohol. De-ionized water was typically used as a final step to remove any organic residue from the solvent cleaning.

The step-by-step process flow for generating bulge samples is listed next:

1. Clean sample using solvents and de-ionized water if need be
2. Load sample into main sputter chamber through load lock
3. Pump system until vacuum approximately $10^{-7} – 10^{-8}$ torr
4. Flood Ar process gas into main chamber to reach 10^{-3} torr
5. With sample rotating, turn on lamp heater with desired substrate temperature

6. Allow system temperature to reach steady state thermal conditions
7. Sputter clean target for ~ 30 s with gun shutter closed
8. Open gun shutter and sputter for desired time/thickness

There were four pure elemental films in this study that required only one gun for the sputtering process (Ag, Au, Cu, and Pt). The fifth film set (Al-[<1wt%] Mg) required co-sputtering of an Al and an Al-Mg target, thus necessitating two guns for the film growth. The Al film was alloyed with Mg to mitigate any irregular grain growth that might occur in a pure Aluminum film at elevated substrate temperatures due to its low melting point. Mg was added since it readily forms a solid solution with Al at low weight percent Mg [73]. Mg solute atoms at the Al matrix grain boundary are expected to act as a solute drag on grain boundary expansion and attenuate rapid grain growth during elevated temperature depositions [74].

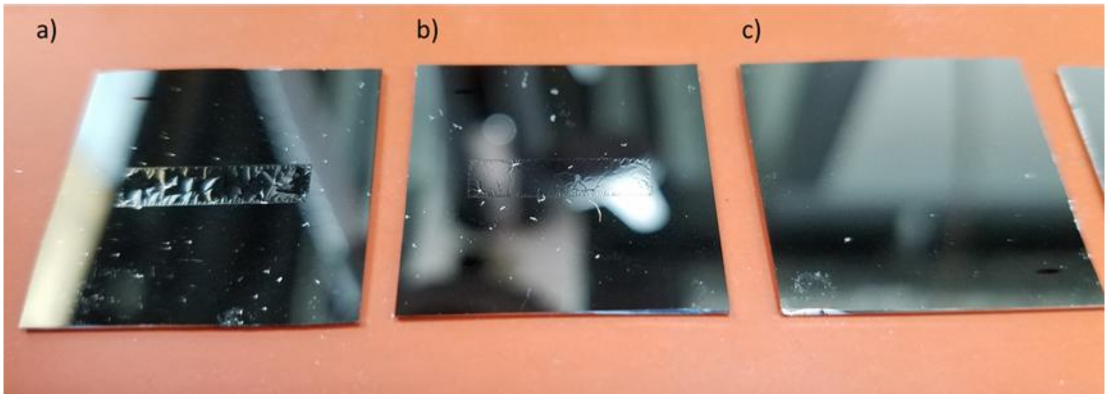

Figure 2.4 Stress state of sputter bulge coupons: a) compressive (buckled) b) near zero and c) tensile

It can be seen in Table 2.1 that all films were sputtered at 100 °C and above. The first, and primary, reason for this is that the Lehigh bulge test method requires the film/nitride composite membrane to be in a state of tension. If the overall stress state of the composite is compressive, the film will buckle and be unusable as a bulge sample, see Figure 2.4a. By depositing the metal at elevated temperature, the film and substrate will be at equal temperature before growth begins. After film deposition and upon cooling the difference in thermal expansion coefficients between the metal and the Si substrate will force the metal film into a state of tension, see Figure 2.4b,c. This thermally induced stress state can be estimated in the following:

$$\sigma_{\alpha} = M_{biaxial}\varepsilon_{\alpha} = \frac{E}{(1-\nu)}(\Delta\alpha_{CTE})(\Delta T) \tag{2.1}$$

Where M_b is the biaxial modulus and α is the coefficient of thermal expansion for substrate and overlayer film.

The second reason for depositing at elevated temperatures is to ensure each film has been effectively annealed at a temperature that is higher than the bulge test temperature, which was typically 80 °C. Thermally stabilizing each sample in the sputtering chamber eliminates any unwanted microstructure changes that might have occurred in an 80 °C bulge mechanical test.

2.2.3 Single crystal film growth

The prior section covered polycrystalline films grown on a free-standing SiN_x membrane. To study the effect of a film lacking grain boundaries, a single crystal film was needed. The sputtering chamber at Lehigh cannot create such a film due to vacuum and temperature requirements needed to grow a 20 mm by 20 mm thin film single crystal. Prepared bulge substrates were sent to the Max Plank Institute for Intelligent Systems in Stuttgart, Germany for single crystal growth. The SiN_x

substrate used for polycrystalline growth was removed so the film could grow epitaxially on the silicon (100) surface. As discussed previously, a partial wet etch of the cavity under the SiN_x membrane, Figure 2.5a, left a thin free-standing silicon membrane. The SiN_x top-side layer was then removed using RIE (Figure 2.5b). The samples were then coated via UHV sputtering with Ag at Max Planck to 500 nm thickness following a recipe proven to create a single crystal film. The Ag/Si membrane composite was submerged in the KOH wet etch process again to remove the silicon underneath the Ag film. Any exposed silicon around the perimeter of the chip was protected with Apiezon W wax as an added precaution. The wax was removed with toluene after the silicon underneath the film was etched.

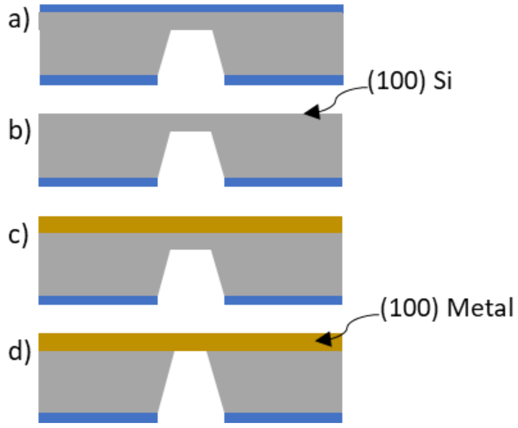

Figure 2.5 Single crystal process flow

2.3 Thin film characterization techniques

The bulge test samples required a multitude of laboratory test techniques to classify the microstructure, composition, and geometry of each deposited metal film.

The following sections will introduce the lab techniques used to parameterize each film.

2.3.1 Film thickness measurements

The bulge test measures a hoop stress in each metal film (Section 2.4) which depends strongly on the thickness of the sample. Sub-micron film thickness measurements can be attained through a variety of techniques. If density ρ is known, and film mass m and deposition area A are measured, the thickness can be estimated by $t = \frac{m}{(A*\rho)}$. Other straightforward techniques include mechanical and optical profilometry methods that measure the step height from film surface to substrate. If a cross section of the film can be made by breaking the substrate or milling through the film using conventional FIB techniques, most SEMs can measure the film thickness with high accuracy.

For this research, the most-used method for thickness determination was the X-Ray Reflectance (XRR) technique (Panalytical Empyrean XRD Unit). This non-destructive technique accurately measures low-roughness films up to about 500 nm which is within the range needed for these particular specimens. An example measurement is shown in Figure 2.6, where the spacing of fringes correlates to the thickness of the film. The interesting feature of this technique is that it can also determine information about buried layers, such as the 10 nm adhesion layer underneath a 100 nm copper film as was the case for Figure 2.6.

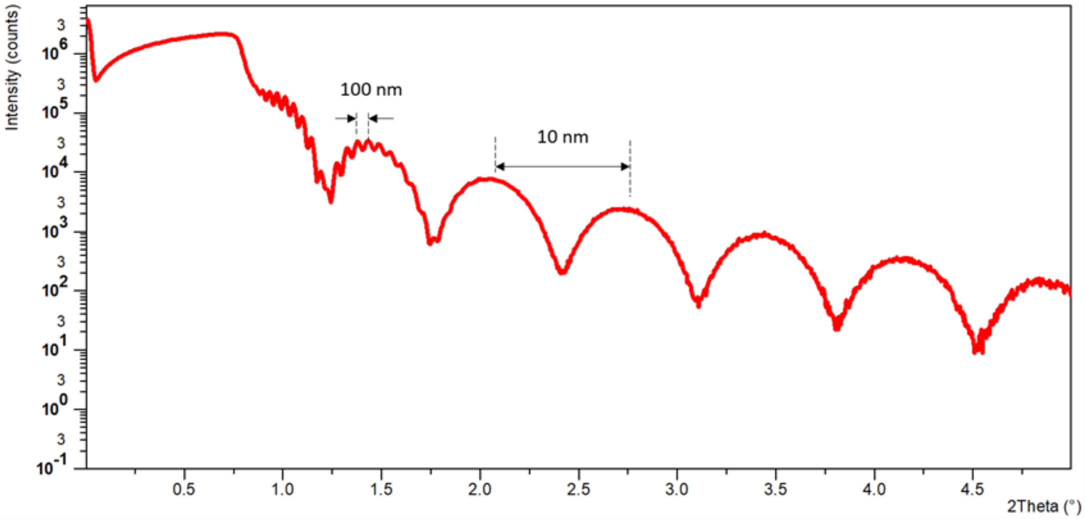

Figure 2.6 XRR thickness measurement example

2.3.2 Crystallinity and texture analysis

The sputtering process tends to generate highly textured metallic films. Most FCC materials will orient in a (111)-oriented fiber texture. The extent of texturing can affect the anisotropic properties of the film, and specifically the time-dependent mechanical properties for this body of work. To measure texture an X-ray Diffraction (XRD) gonio powder scan was performed on each metal film using the Panalytical Empyrean XRD unit, scanning from 20° to 80° 2-theta. Each FCC metal had four or five low order planes that would diffract within this range. The relative peak intensities were then compared to bulk polycrystalline powder scans to determine the relative texturing extent.

The single crystal Ag film can be thought of as an extremely textured film. This film had large enough grains (i.e. one) to be a candidate for Electron Backscatter Diffraction (EBSD) studies, whereas all the polycrystalline films were finer than the resolution limit of the EBSD technique. The Ag single crystal film was measured via EBSD analysis and XRD texture analysis to determine the orientation of the single crystal film.

2.3.3 Dislocation density measurements

2.3.3.1 CMWP XRD method

The two prominent X-ray line profile analysis techniques used to determine dislocation density are a line broadening evaluation technique known as the Williamson-Hall method [75] and a Fourier transform of the line broadening by Warren-Averbach [76]. Recent methods to build on these techniques have been developed including Multiple Whole Profiling (MWP) fitting and Convolutional Multiple Whole Profile (CMWP) fitting [77,78]. The CMWP method allows XRD patterns to be evaluated in terms of crystallite size, dislocation densities, and dislocation character. It is deconvoluted from instrumental effects and any overlapping peak effects that hinder MWP fitting methods. The raw XRD 2-theta data is fit to the following equation:

$$I_{theoretical} = BG(2\theta) + \sum_{hkl} I_{MAX}^{hkl} I^{hkl}(2\theta - 2\theta_0^{hkl}) \quad \textbf{(2.2)}$$

Where $BG(2\theta)$ is the background signal, I_{MAX}^{hkl} is peak intensity, $2\theta_0^{hkl}$ is the peak center and I^{hkl} is the portion of the signal containing broadening effects from instrument effects, crystallite size, and dislocation density, and any planar faults:

$$I^{hkl} = I_{instr.}^{hkl} + I_{size}^{hkl} + I_{disl.}^{hkl} + I_{pl\,faults}^{hkl} \tag{2.3}$$

The fitting parameter for $I_{disl.}^{hkl}$ provides the dislocation density for the material being tested. An online, front-end CMWP fitting program was used in this work to evaluate the dislocation densities of each metal film. (eCMWP, http://csendes.elte.hu/cmwp/) An example fitting trace is shown in Figure 2.7. The measured data (green) is fit using equation (2.2) as shown by the red trace. The error shown in blue is the difference between measured and fit data.

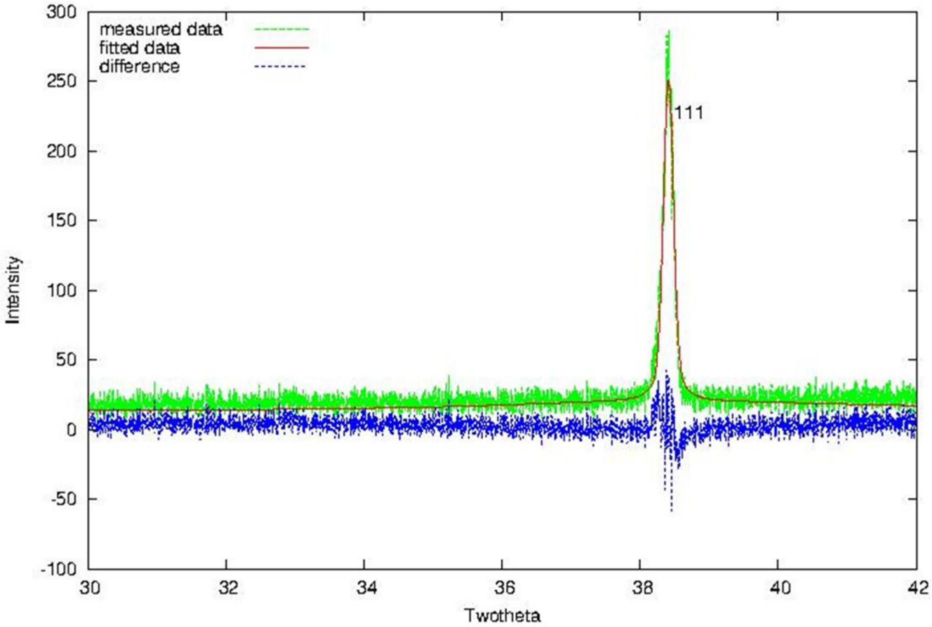

Figure 2.7 Example CMWP fitting function of thin film XRD 2-theta scan

For the CMWP analysis a hybrid monochromator was used to attenuate $K_{\alpha2}$ incident x-rays from the Cu X-ray source leaving only 0.150598 nm $K_{\alpha1}$ impinging on each sample. A ½° divergence slit and 4 mm mask were used on the incident beam and a PIXcel3D detector with 0.04 rad soller slit on the diffracted beam. It is common to correct for instrument broadening in CMWP analysis but this procedure is not necessary in sputtered thin films [79].

2.3.3.2 TEM measurements using Ham's method

To compliment the CMWP XRD measurements, a site-specific dislocation density measurement was performed using TEM imaging. Plan view samples were made by carefully removing a sputtered thin film from the substrate with tweezers and attaching it to a 90° SEM sample mount with conductive copper adhesive, as shown in Figure 2.8. An extraction needle was used to remove a portion of the metal film, followed by a FIB-thinning process to create a TEM transparent foil. The thickness of the foil was measured by rotating the sample mount so the film thickness was oriented edge-on to the incident SEM beam.

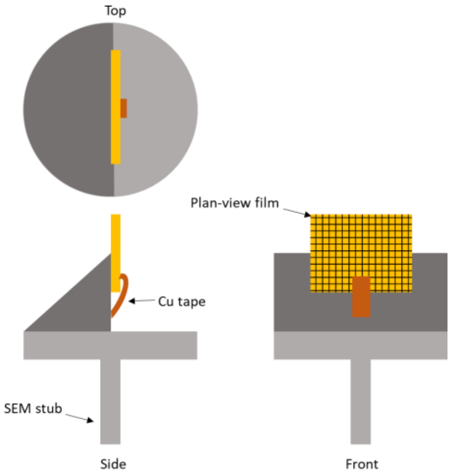

Figure 2.8 Plan view sample mount for TEM study

Ham's intersection method was used to measure the dislocation density of a specific grain using TEM images that meet dislocation diffraction conditions [80]. A mesh is superimposed over a grain that meets dislocation contrast requirements. The total length (L) of the mesh is measured using ImageJ software. The number of intersections (m) between the mesh and dislocation lines are counted, also using ImageJ. Knowing the foil thickness (t), the dislocation density can then be estimated using:

$$\rho = \frac{2m}{Lt} \qquad \textbf{(2.4)}$$

A schematic of the Ham method is shown in the work by Miyajima in Figure 2.9 [81]. The red circles represent the intersection of dislocation lines with the overlaid mesh on a single grain of interest.

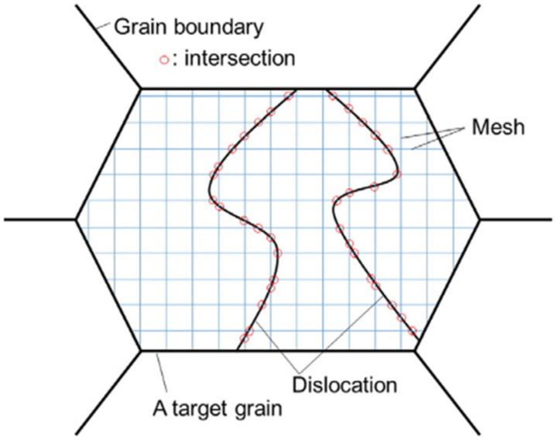

Figure 2.9 Ham's intersection method for TEM dislocation density analysis [81]

2.3.4 Electron microscopy

Electron microscope techniques were used extensively for imaging in this work. Field Effect Scanning Electron Microscopes (FESEM) used to measure plan-view grain size include the Zeiss Leo 1550 VP and FEI Scios SEM/FIB dual-beam. The average grain size was measured using the lineal intercept method as described in ASTM standard E112-13.

The Focused Ion Beam (FIB) beam of the Scios SEM was used for cross sectional imaging and TEM sample prep.

A JEOL 2000 and JEOL 1200x were used to image both cross sectional and plan-view TEM images of sputtered films. Dislocation density calculations were performed on TEM images tilted in such a way to permit dislocation line contrast.

Additional SEM techniques such as Energy Dispersive Spectroscopy (EDS) and EBSD were used to compliment the imaging studies. EDS was used to verify the < 1wt % concentration of Mg in the Al-Mg alloy film. EBSD was unsuitable for grain mapping of polycrystalline thin films due to the fine grain structure, but was used to determine the crystal structure of the single crystal film.

2.4 Bulge test technique overview

2.4.1 Gas pressure bulge test

The time-dependent mechanical properties of all thin films presented in this work were measured using the bulge test method [7,42,44]. This method utilizes gas pressure to bulge or inflate a thin film from one side, while measuring the deflection capacitively on the opposite side. For the Lehigh system this capacitive measurement necessitates that the film is conductive, or a very thin metallic coating can be applied as long as it doesn't influence the behavior. The bulge sample is situated at the intersection of two vacuum chambers as shown in the cross-sectional schematic of Figure 2.10. Both vacuum chamber 1 and 2 are pumped to millitorr range and isolated from each other via Valve 2.

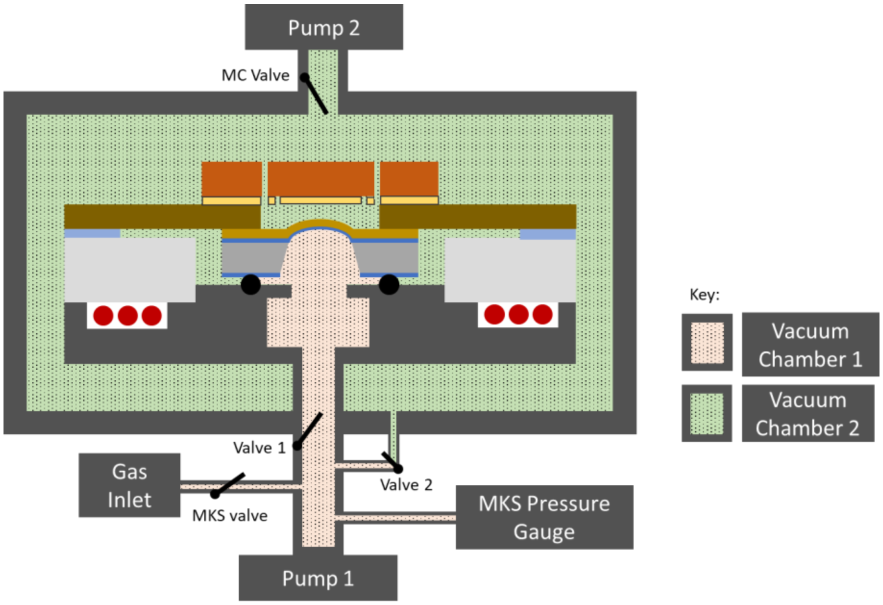

Figure 2.10 Experimental setup of bulge system

An enlarged view of the sample holding unit of the bulge system is shown in Figure 2.11. A series of springs (not shown) apply downward pressure on the printed circuit board, Be-Cu spacer layer, and bulge sample against the O-ring seal. This seal isolates one vacuum chamber from the other. The circuit board contains a 6 mm by 6 mm square metal contact that acts as the fixed electrode of the bulge capacitor. This bulge unit contains a coiled heater (www.watlow.com, 0.125'' dia, 24'' long, 30 W/in^2 cable heater) that allowed the bulge testing up to a maximum of 100 °C.

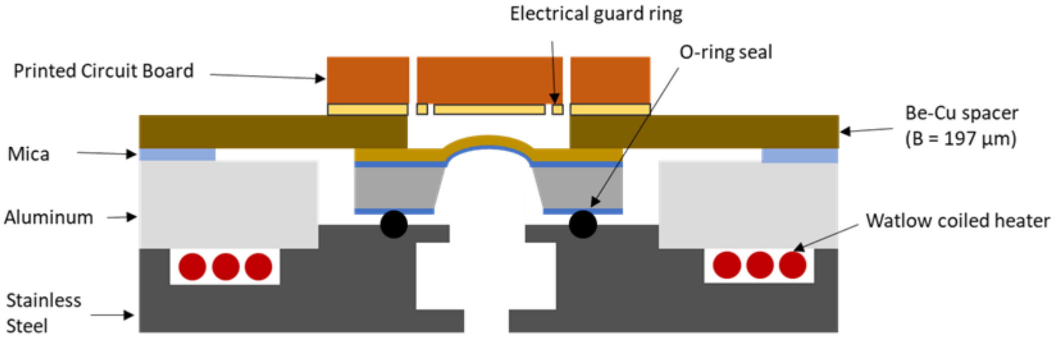

Figure 2.11 Enlarged bulge test setup with callouts

A pressure of N_2 gas was applied into vacuum chamber 1 via an MKS solenoid valve. The pressure differential causes the film, which is at the interface between to vacuum chambers, to inflate or bulge. The applied pressure is measured by a capacitive pressure gauge (Baratron 0-1000 torr range) and controlled by a MKS Type 250 unit. A Labview PID (proportional-integral-derivative) feedback program controls the MKS gas inlet valve to reach a desired bulge pressure as measured by the Baratron pressure gauge.

2.4.1.1 Bulge lock-in measurement:

The Lehigh bulge unit measures film deflection via a sensitive capacitance measurement. This measurement is accomplished by comparing the output current of a bulge capacitor (C_0) against a reference capacitor (C), using a lock-in amplifier to collect and amplify the signal ($V_{lock\text{-}in}$) to the Labview controlling program (Figure 2.12).

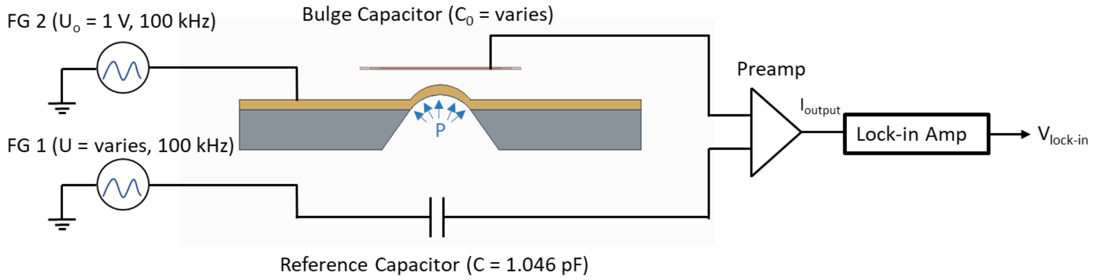

Figure 2.12 Bulge capacitor data collection method

As pressure is applied to bulge the thin film, the capacitance increases by closing the gap between the fixed electrode and the curved film. The increase in capacitance is compared against the reference signal and is measured via the lock-in. This lock-in signal is the summation of the bulge and reference capacitor currents ($I_{outputs}$) multiplied by a k constant:

$$V_{lock-in} = k \cdot I_{output} = k(U \cdot C - U_0 \cdot C_0) \qquad \textbf{(2.5)}$$

where U or U_0 is the function generator voltage and C or C_0 is the capacitance. When the signals from each capacitor are equal, the output signal from the pre-amp is zero due to constructive interference. In this case of electrical balance ($V_{balance}$) the following holds true:

$$C_0 = \frac{C \cdot U}{U_0} \qquad \textbf{(2.6)}$$

This balance condition is shown graphically in Figure 2.13. A linear increase in lock-in signal is measured as the system shifts from either side of the balance conditions.

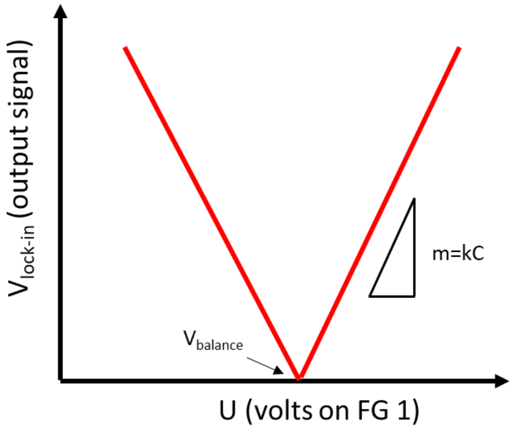

Figure 2.13 Bulge k constant extraction

By holding the function generator signal on the bulge capacitor constant (U_0 = 1 V), it is possible to extract the k constant for the bulge set up by measuring the change in lock-in signal ($\Delta V_{lock\text{-}in}$) with changes in voltage on the reference capacitor function generator (ΔU):

$$V_{lock-in,2} - V_{lock-in,1} = k[C(U_2 - U_1) - C_0(U_{02} - U_{01})] \quad \textbf{(2.7)}$$

Since C was set at 1.046 pF we can calculate k:

$$\frac{\Delta V_{lock-in}}{\Delta U} = m = k \cdot C \quad \textbf{(2.8)}$$

Now that k has been calculated for the bulge setup, bulge experiments will require only the collection of the $V_{lock\text{-}in}$ to determine how the bulge capacitance (C_o) is changing with applied pressure.

2.4.1.2 Variable capacitance measurement:

A typical capacitor consists of two planar electrodes of area A separated by an electrode gap, d:

$$C = \varepsilon_0 \frac{A}{d} \tag{2.9}$$

Where $\varepsilon_0 = 8.85 \times 10^{-12}$ F/m. A bulged film produces one electrode that has curvature, and this curvature changes depending on the applied pressure. To account for this non-standard capacitance an integration of electrode gap d was needed. Figure 2.14 provides an overview of the curved bulge electrode and all mathematical relations used to measure bulge capacitance. This figure incorporates important bulge system dimensions such as fixed electrode edge length (b), electrode spacing (B), membrane width (D), bulge height (H), bulge curvature (R), and film thickness (t).

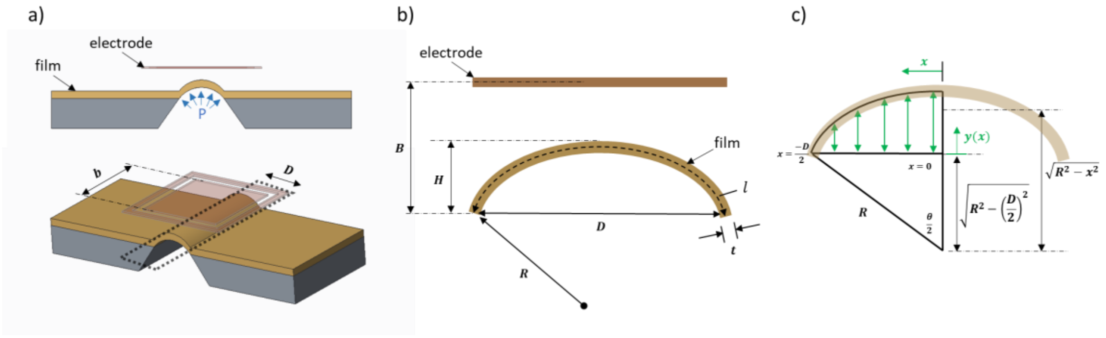

Figure 2.14 Variable capacitance a) bulged film b) cross section and c) mathematical relations

The height of any given point along the bulged film can be calculated using:

$$y(x) = \sqrt{R^2 - x^2} - \sqrt{R^2 - \left(\frac{D}{2}\right)^2} \tag{2.10}$$

By integrating the variable capacitance gap across the full width (D) of the membrane we can calculate the capacitance of the bulge system:

$$C_0 = \varepsilon_0 b \int_{\frac{-D}{2}}^{\frac{D}{2}} \frac{dx}{B - y(x)} \tag{2.11}$$

This integration then yields:

$$C_0 = 4\varepsilon_0 b \frac{\sqrt{4R^2 - D^2} \cdot \tan^{-1}\left(\frac{D}{\sqrt{4B\sqrt{4R^2 - D^2} - D^2}}\right)}{\sqrt{4B\sqrt{4R^2 - D^2} - D^2}} \tag{2.12}$$

It also follows from Figure 2.14c that the height of a bulged film is related to the radius of curvature (R) and the width of the membrane (D) in the following way:

$$H = R - \sqrt{R^2 - \frac{D^2}{4}} \tag{2.13}$$

A measured change in $V_{\text{lock-in}}$ corresponds to a change in capacitance of the bulge capacitor:

$$V_{lock-in,2} - V_{lock-in,1} = \Delta V = k(U_0 \Delta C_0) \tag{2.14}$$

This change is proportional to a change in height of the bulge membrane:

$$\Delta C_0 \propto \Delta H \tag{2.15}$$

With known geometric constants D, b, and B we can plot arbitrary bulge heights (H) against a change in bulge capacitance (C_0) across a range of curvatures (R).

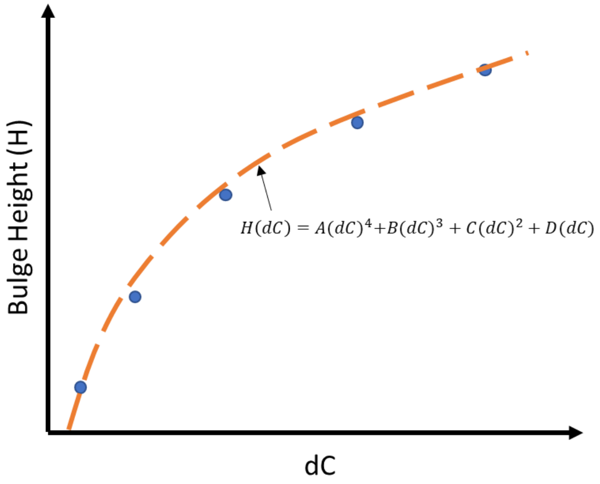

Figure 2.15 Bulge height vs dC fitting

A four-term fitting function of the following form was used to describe this relationship:

$$H(dC) = A(dC)^4 + B(dC)^3 + C(dC)^2 + D(dC) \tag{2.16}$$

2.4.1.3 Converting electrical signal to film mechanics

The bulge experiment converts a lock-in voltage signal into a change in capacitance which is proportional to the height of the bulged membrane (H). This term is the key for extracting the stress and strain state of the bulged film. If plane strain conditions (Section 2.4.2.2) are present in a bulged film, the required deflection pressure, film stress, and film strain can be calculated using H [41]. The bulge pressure for a rectangular film is:

$$P = 2\sigma_0 t \frac{H}{a^2} + \frac{4M_{ps}tH^3}{3a^4} \qquad \textbf{(2.17)}$$

Where a = D/2, σ_0 = residual biaxial stress, and M_{ps} = plane strain modulus. The Lehigh bulge system required a correction factor when using equation (2.17) to convert measured bulge height H into a P. This correction factor accounted for how tight the bulge user clamped down the spring-loaded system during sample mounting. This correction factor ($-\Delta H_{correction}$) calibrated the height data to a simulated response and typically varied between 10 and 20%. This correction is shown in Figure 2.16.

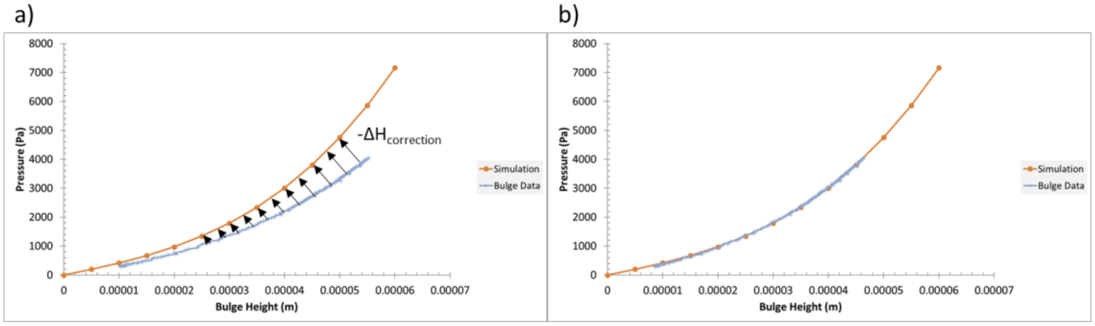

Figure 2.16 Bulge data height correction factor a) as-measured and b) calibrated

The hoop stress is then given by:

$$\sigma_{xx} = \frac{Pa^2}{2Ht} \qquad \textbf{(2.18)}$$

The film strain is calculated in the following manner:

$$\varepsilon_{xx} = \frac{2H^2}{3a^2} + \varepsilon_0 \qquad \textbf{(2.19)}$$

Where ε_0 is the residual plane strain of the film. By plotting σ_{xx} vs ($\varepsilon_{xx} - \varepsilon_0$) we can determine the stress-strain condition of a bulged film [44].

$$\sigma_{xx} = \left(\frac{E}{1-\nu^2}\right)(\varepsilon_{xx} - \varepsilon_0) + \sigma_0 \qquad \textbf{(2.20)}$$

This stress-strain condition is plotted in Figure 2.17. The blue line represents the residual stress that is present in an as-deposited thin film and the red lines are the hoop stresses generating during bulge experiments. The dashed red lines represent strains where the film plastically deforms and then is unloaded elastically. The difference in elastic slopes is due to the difference in loading; residual stress is equal-biaxial so the biaxial modulus E/(1-υ) applies, whereas during bulge testing the stress is plane strain so the appropriate elastic modulus is E/(1-υ^2). All films presented in this study were bulged well within the elastic limit, mostly to ~ 0.1% strains, and so the dashed region (plastic) is not considered further.

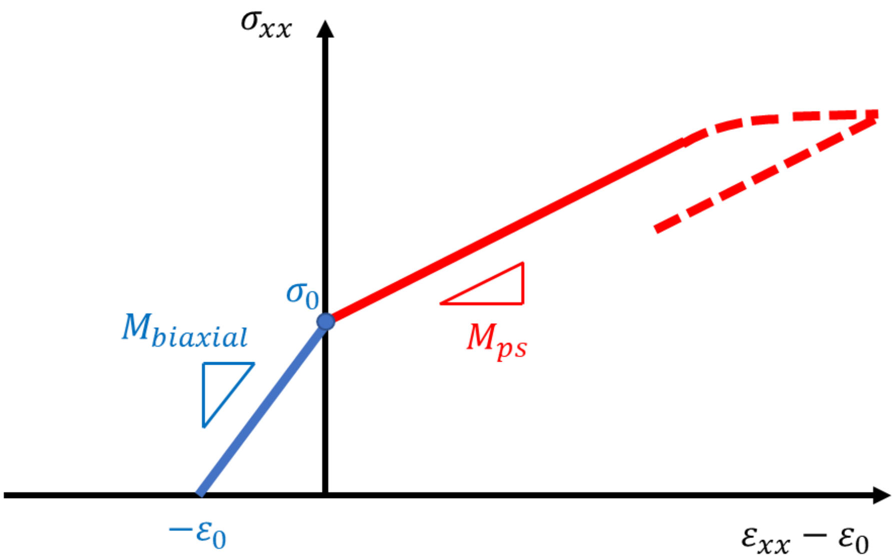

Figure 2.17 Stress-strain condition of bulged film

2.4.1.4 Labview feedback control

All bulge experiments required a pressure ramp loading/unloading test and an iso-strain relaxation test. The bulge height (H) is controlled by adjusting calculated capacitance (C) with a change in gas pressure (ΔP) through the MKS gas inlet valve. The Labview program estimates the electrode spacing as $(B - \frac{2}{3}H)$. Thus, a capacitance for a given height is recorded as:

$$C = \varepsilon_0 \frac{bD}{\left(B - \frac{2}{3}H\right)} \tag{2.21}$$

Converting to a height estimate:

$$H = \frac{3}{2}\left(B - \frac{\varepsilon_0 bD}{C}\right) \tag{2.22}$$

After performing a pressure ramp test the residual stress (σ_0) and plane strain modulus (M_{ps}) are extracted. These terms can then be inserted into the Labview feedback control for an iso-strain (relaxation) test. A constant height is maintained by small changes in pressure to account for stress relaxation:

$$\Delta P = \left(\frac{8t\sigma_0}{D^2} + \frac{64tM_{ps}H_0^2}{D^4}\right) \cdot \Delta H \qquad \textbf{(2.23)}$$

The small changes in height (ΔH) are related to the small changes in capacitance that will be measured by changes in the lock-in voltage:

$$\Delta H = (H_0 - H_1) = \frac{3}{2} \cdot \left(\frac{\varepsilon_0 bD}{C_1} - \frac{\varepsilon_0 bD}{C_0}\right) \qquad \textbf{(2.24)}$$

2.4.2 Bulge conditions and assumptions

2.4.2.1 Composite film considerations

All films tested in this study are metal-SiN_x composites. The amorphous SiN_x layer is used as an etch stop during microfabrication and as a substrate for metal deposition. The SiN_x baseline properties were determined by lightly coating (< 10 nm) an etched, free-standing SiN_x membrane with a conductive metal. After performing a series of bulge loading and unloading tests, the properties of the nitride film were extracted. They are summarized in Table 2.2.

Property	Value
Crystallinity	Amorphous
Thickness	200 nm
σ_0	250 MPa
M_{ps}	200 GPa

Table 2.2 SiN_x mechanical properties

All of the bulge stress-strain relations listed in Section 2.4.1 are for the composite film. Since the amorphous SiN_x layer will not show relaxation behavior and exhibits purely elastic deformation for the range of strain used in this study, it is possible to extract the SiN_x fractional contribution from the composite. By knowing the thickness of the metal film, it is also possible to calculate the residual stress of the metal (σ_{metal}) after measuring the residual stress of the composite film ($\sigma_{composite}$) during a bulge ramp test:

$$\sigma_{composite} = \frac{\sigma_{metal} t_{metal} + \sigma_{SiN_x} t_{SiN_x}}{t_{metal} + t_{SiN_x}} \qquad \textbf{(2.25)}$$

The plane strain modulus can be extracted in a similar manner:

$$M_{composite} = \frac{M_{metal} t_{metal} + M_{SiN_x} t_{SiN_x}}{t_{metal} + t_{SiN_x}} \qquad \textbf{(2.26)}$$

2.4.2.2 Necessary plane strain conditions for bulge test

Plane strain conditions in a bulged rectangular film can only be met if the length to width aspect ratio is 4:1 or greater [41]. To meet this requirement and ensure plane strain conditions in the bulged capacitor area, the freestanding portion has a length of 12 mm and width of 3 mm, Figure 2.2b. The plane strain, or hoop, conditions will be met in the central region of the length of the film and will be violated near the ends of the long ends. The 6 mm by 6 mm fixed electrode is situated to only measure within the hoop stress conditions and avoid the more complex stress conditions near the ends of the rectangular film.

Once hoop stress conditions are met the following assumptions are made:

$$\varepsilon_c, \varepsilon_t, \sigma_c, \sigma_l \neq 0;\ \varepsilon_l, \sigma_t = 0 \tag{2.27}$$

The strains in the film are graphically depicted in Figure 2.18.

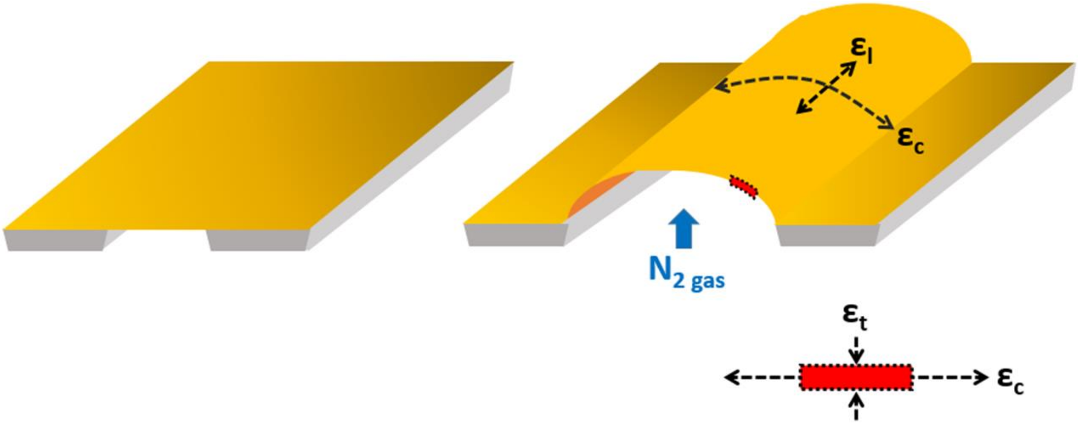

Figure 2.18 Hoop strain schematic in bulged film

The longitudinal strain is zero due to geometric 4:1 aspect ratio:

$$\varepsilon_l = 0 = \left(\frac{1}{E}\right)\sigma_l + \left(\frac{-\nu}{E}\right)\sigma_c + \left(\frac{-\nu}{E}\right)\sigma_t \tag{2.28}$$

This allows a simple relation between stresses:

$$\sigma_l = \nu\sigma_c \tag{2.29}$$

Plugging into the hoop strain equation:

$$\varepsilon_c = \left(\frac{1}{E}\right)\sigma_c + \left(\frac{-\nu}{E}\right)\nu\sigma_c + \left(\frac{-\nu}{E}\right)\sigma_t \tag{2.30}$$

And finally converting to hoop strain with plane strain modulus:

$$\sigma_c = \left(\frac{E}{1-\nu^2}\right)\varepsilon_c = M_{ps}\varepsilon_c \tag{2.31}$$

2.4.2.3 Bulge testing @ 80 °C

All bulge tests for this work were performed at 80 °C which was controlled by a Cole Palmer J-Type heater controller. This controller applied DC voltage to the Watlow coiled heater until the bulge test fixture was heated to a stable 80 °C, which usually took about an hour with the chamber under roughing vacuum conditions. Two thermocouples monitored the temperature of the bulge test, one on the heater itself and one on the Be-Cu spacer surface, which was the closest a thermocouple could be mounted to the bulge film sample. The purpose of running all tests at elevated temperature was to maximize the relaxation extent for each film so trends would be more apparent. Prior work has shown increased viscoelastic relaxation at elevated temperatures [7].

2.4.3 Bulge ramp and relaxation testing

The bulge test method requires two experimental tests to measure the relaxation behavior of thin metallic films. The strain control and measured stress response for each are depicted in Figure 2.19. The first test is a "ramp test" where the film is strained just beyond the 0.1% (ε = 0.001) iso-strain relaxation point and quickly unloaded (Figure 2.19a,c). This ramp is performed at 4 torr/s using the Labview controlling program, corresponding to a hoop strain rate of approximately $5 \times 10^{-5} s^{-1}$ for each bulge test. The extracted data is converted into a stress-strain response and film properties can be extracted: specifically, the residual stress (σ_0) and the plane strain modulus (M_{ps}). The residual stress is determined as a y-intercept of the stress axis and the modulus is calculated from the linear slope of the unloading segment.

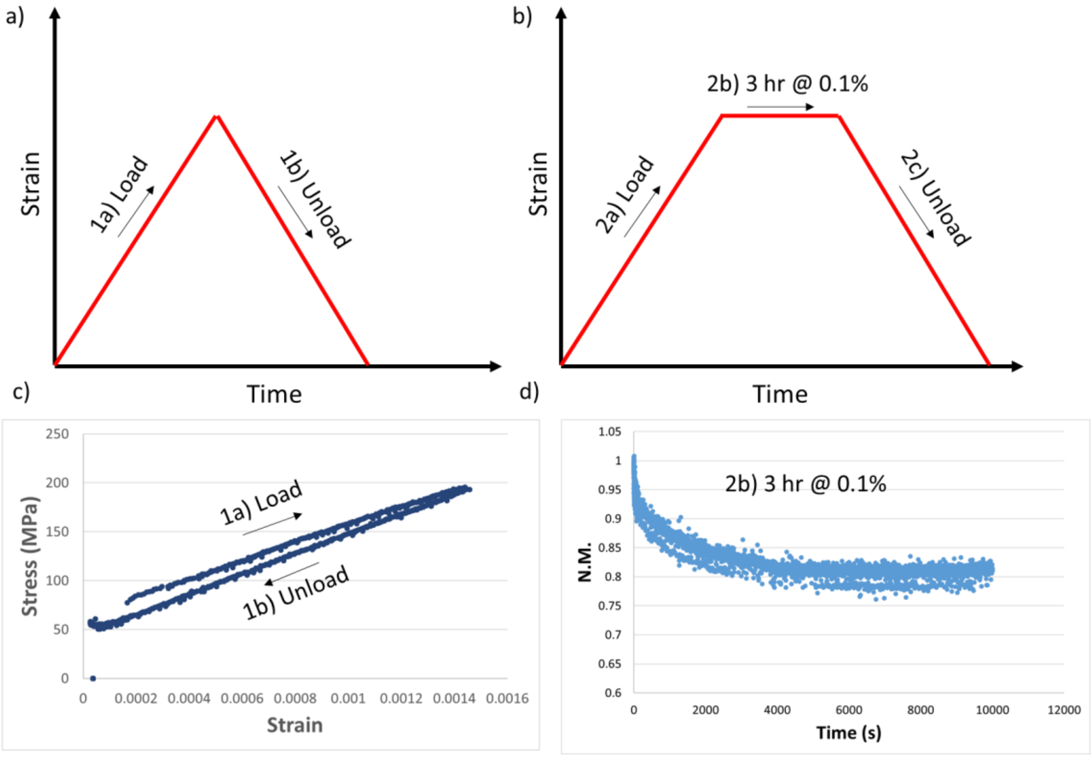

Figure 2.19 Bulge ramp and iso-strain test. Strain response for a) ramp and b) relaxation test. Stress response from c) ramp and N.M. decay during d) relaxation test.

The second test for each film is a stress relaxation test, where the film is loaded up to the iso-strain condition of 0.1%, held for 10,000 seconds, and then unloaded (Figure 2.19b,d). During the holding period the Labview feedback loop maintains the bulge height (H) by controlling the pressure allowed through the MKS inlet valve. The metallic film relaxes, and the drop in stress is recorded with time. The plane strain modulus decays with time $M_{ps}(t) = \frac{\sigma(t)}{\epsilon}$ and can be normalized by dividing by the initial, unrelaxed modulus, $M_{ps}(t=0) = \frac{\sigma(t=0)}{\epsilon}$

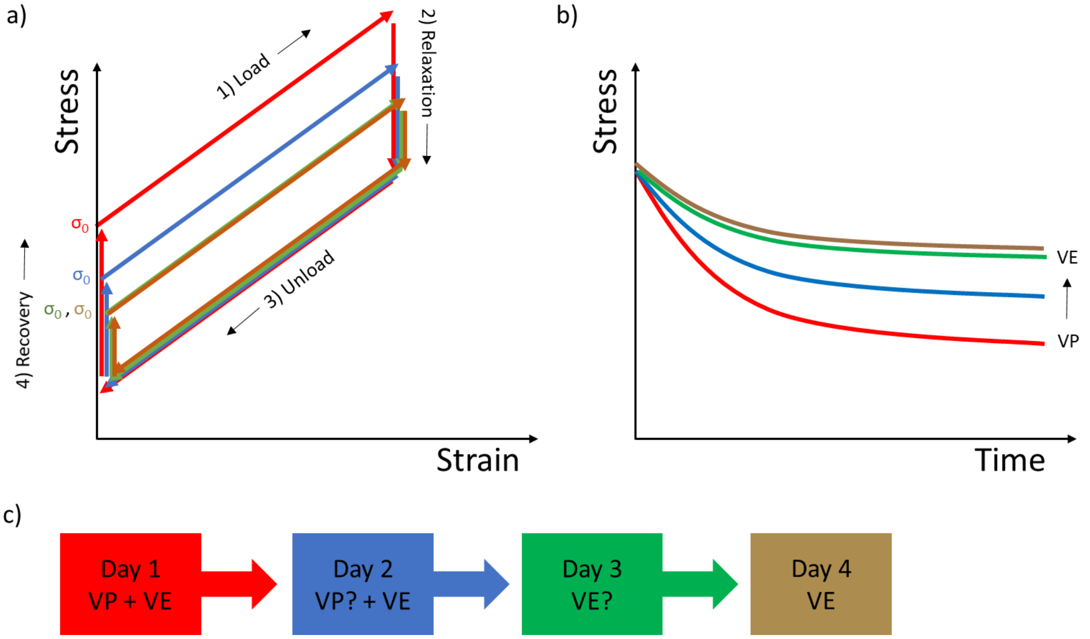

Figure 2.20 Typical bulge test results from viscoplastic (VP) to viscoelastic (VE)

Figure 2.20a,b depicts the typical stress-strain and stress-time responses for FCC metal films undergoing 0.1% iso-strain relaxation testing. Each film is tested once per day with ~ 24 recovery period between tests. Initially a combined viscoplastic and viscoelastic response is present in each metal film. By the fourth day a steady state, purely viscoelastic response is measured in each metal film. A bulge operation would follow Figure 2.20c until the stress relaxation responses overlapped and the film reached steady state conditions as seen between the overlapping relaxation curves in Figure 2.20b.

3. Grain size dependence in FCC metal films

Conventionally, fine-grained materials are highly resistant to plastic deformation due to a very high density of grain boundary/dislocation interactions, as described by the Hall-Petch relation. This strengthening mechanism is independent of other mechanisms like solid solution strengthening and work hardening. While the Hall-Petch effect is known to apply to thin films with regard to calculation of yield strength, it is not known if this same mechanism affects viscoelastic stress relaxation. This portion of the study is designed to determine if a similar intrinsic grain size effect is present in metallic thin films under anelastic stress conditions. Toward this end, the stress relaxation behavior of five face centered cubic metals is investigated by bulge testing at a test temperature of 80 °C. The five FCC metal films are Ag, Al(Mg), Au, Cu, and Pt. The grain size was varied from tens of nanometers to many hundreds of nanometers by adjusting the substrate temperature during deposition.

Ideally, only the grain size of the films would be affected by changing deposition temperature, thereby unambiguously correlating any changes in relaxation to grain size. Unfortunately, elevated temperature deposition can cause changes in surface roughness (e.g., from grain boundary grooves) and crystallographic texture. Also, metal films undergo thermal contraction upon cooling from an elevated deposition temperature. When adhered to a silicon substrate, significant thermal stresses can be generated that cause room temperature residual stresses and possibly even plastic deformation. Thus the potential differences in roughness, texture, residual stress, and dislocation structure among the films must be evaluated and their potential influences on relaxation must be assessed. Only then can the effects of grain size on relaxation be clearly identified.

3.1 Polycrystalline films

The primary area of research in this study is comparing viscoelastic deformation behavior of sub-micron FCC metal films produced via the sputtering process. This deposition process typically produces polycrystalline, columnar films and nearly all of the specimens used in this investigation will be of this configuration. The substrate temperatures during sputtering were varied from 100 °C to a max of 500 °C. The range of temperatures chosen depended on three factors. The first factor was how close the process temperature was to the metal's melting temperature, generally keeping the maximum temperature below half T_{mp} (in Kelvin units). The second factor was to select only process temperatures where the deposited metal surface roughness was smooth and maintained an approximate mirror finish, thus minimizing any potential effect of grain boundary grooving on stress relaxation. The temperature at which roughness was considered an issue was determined experimentally through trial and error. The last temperature concern was to prevent sputter chamber damage when depositing high melting point materials (e.g. Pt). A substrate temperature of 500 °C was selected as the safest practical maximum temperature before risk of damaging sputter system components.

3.1.1 Characterization of grain structure

The characterization of each film requires electron microscopy (SEM & TEM) and X-ray diffraction (XRD) techniques. The following subsections will present the results of these characterization techniques for each FCC metal film.

3.1.1.1 SEM microscopy

The columnar nature of sputter deposition means the grain size can be represented by a diameter of the x-y surface of each film. These plan-view surfaces were recorded for all metals in this study and are presented below [Ag (Figure 3.1), Al(Mg) (Figure 3.2), Au (Figure 3.3), Cu (Figure 3.4), and Pt (Figure 3.5)]. Each image was taken using a Zeiss 1550 Field Effect Scanning Electron Microscope (FESEM) with an in-lens secondary electron (SE) detector. The magnification varies between 10,000X to 75,000X.

a) Ag @ 100C b) Ag @ 125 C

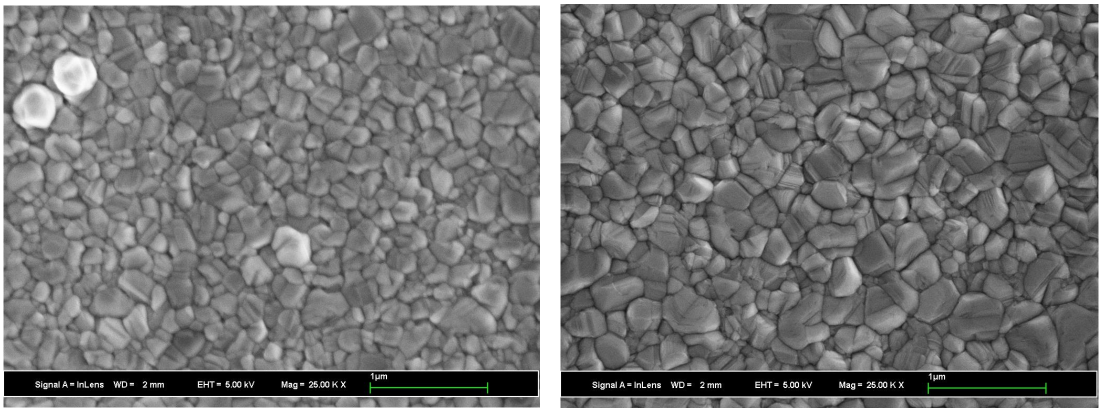

c) Ag @ 150C d) Ag @ 175C

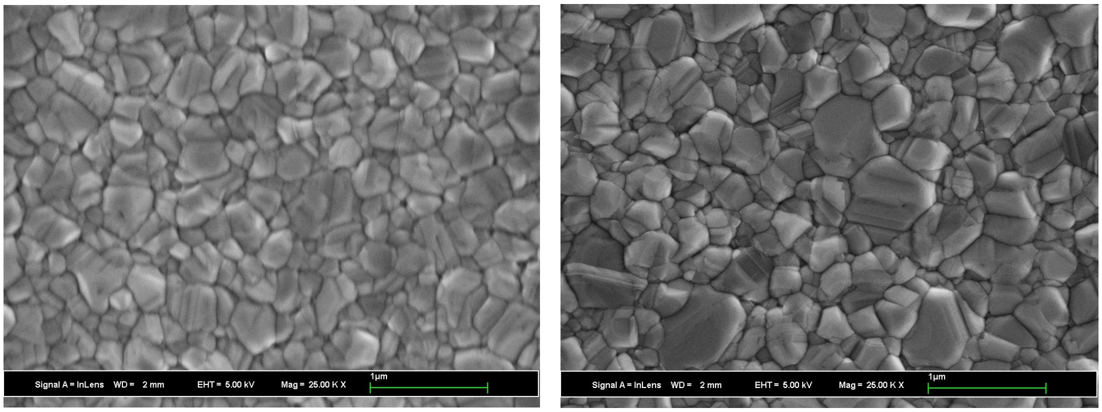

e) Ag @ 200C

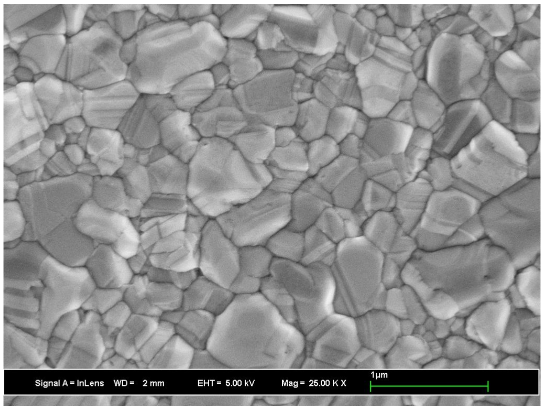

Figure 3.1 Ag film plan view SEM images

a) Al (Mg) @ 100C b) Al (Mg) @ 150C

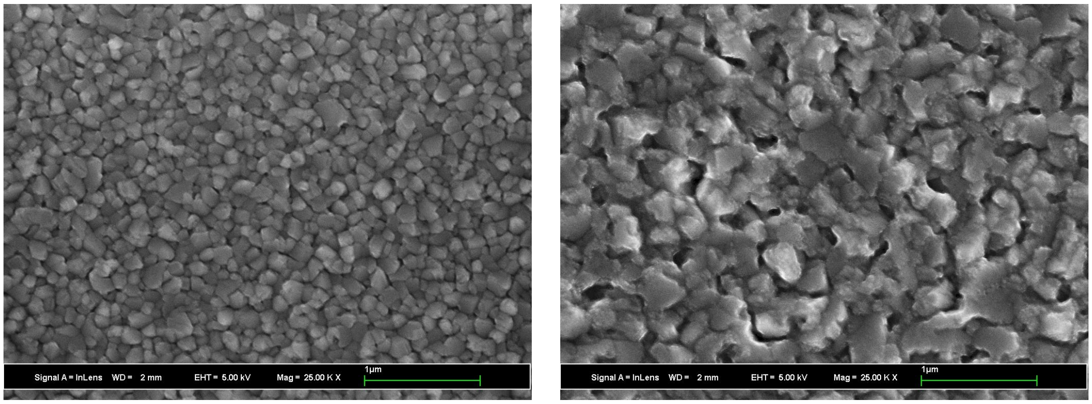

c) Al(Mg) @ 200C

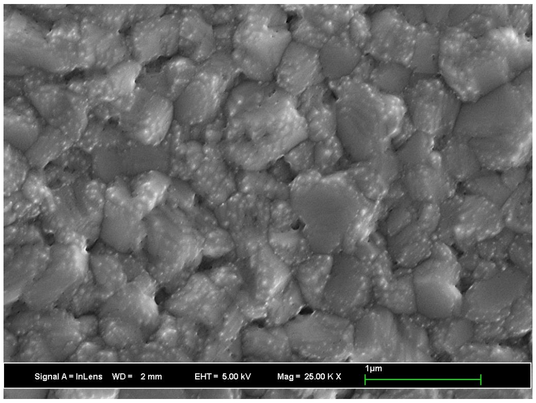

Figure 3.2 Al(Mg) film plan view SEM images

a) Au @ 100C

b) Au @ 175C

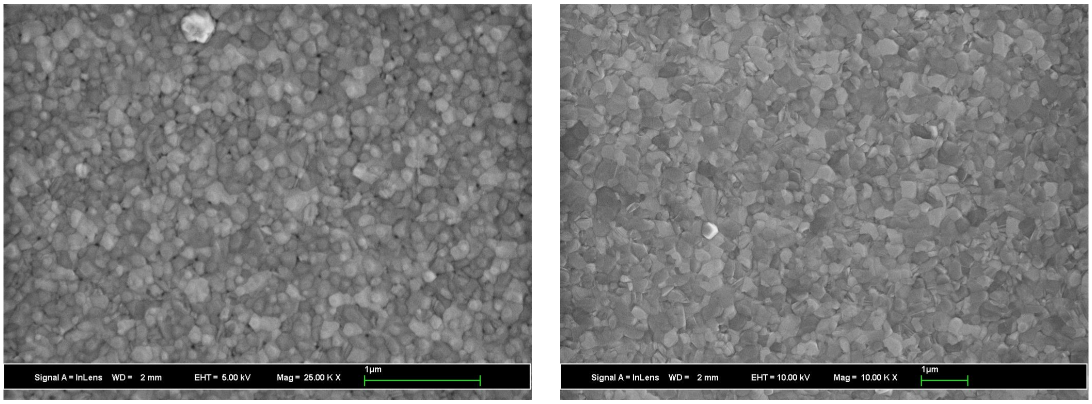

c) Au @ 300C

d) Au @ 400C

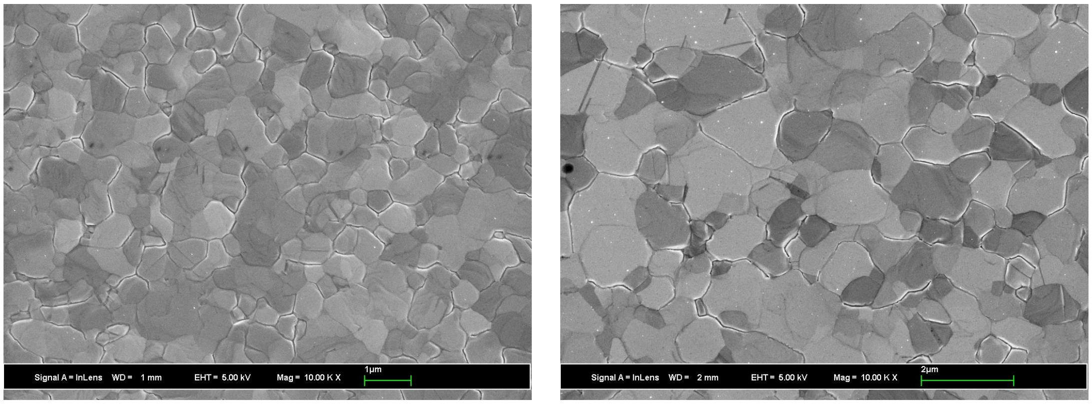

Figure 3.3 Au film plan view SEM images

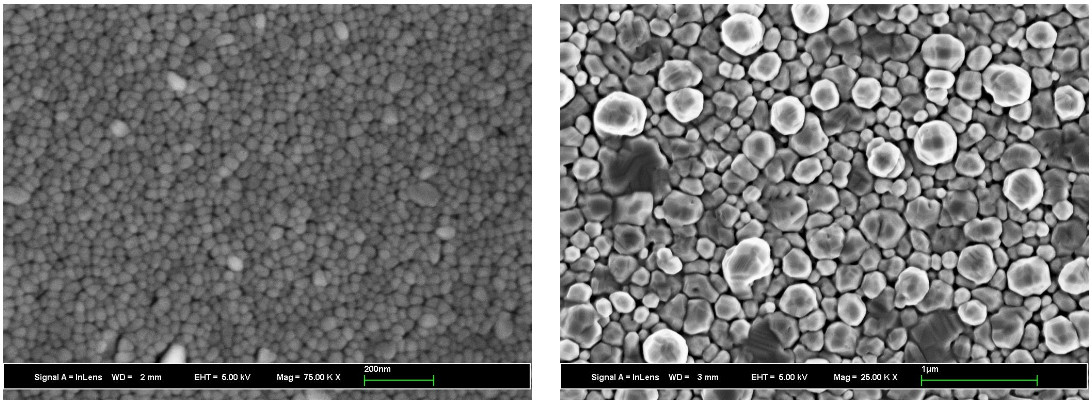

a) Cu @ 100C

b) Cu @ 200C

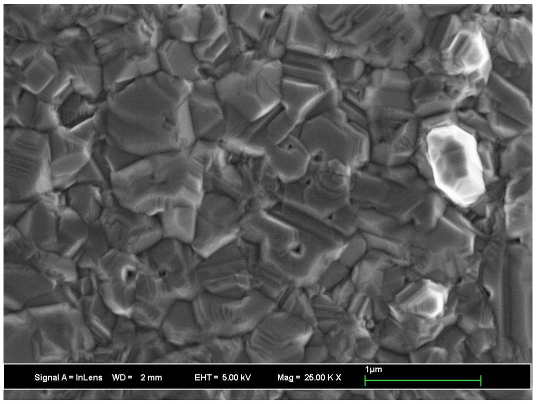

c) Cu @ 300C

Figure 3.4 Cu film plan view SEM images

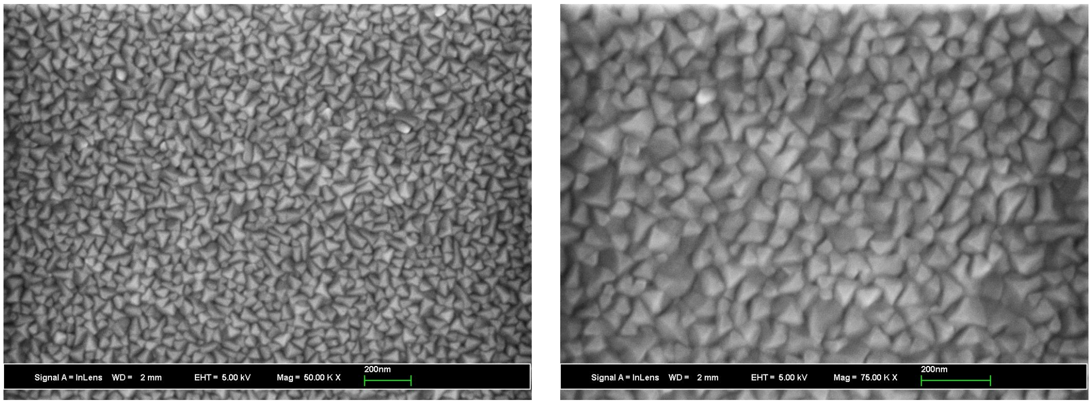
a) Pt @ 150C

b) Pt @ 200C

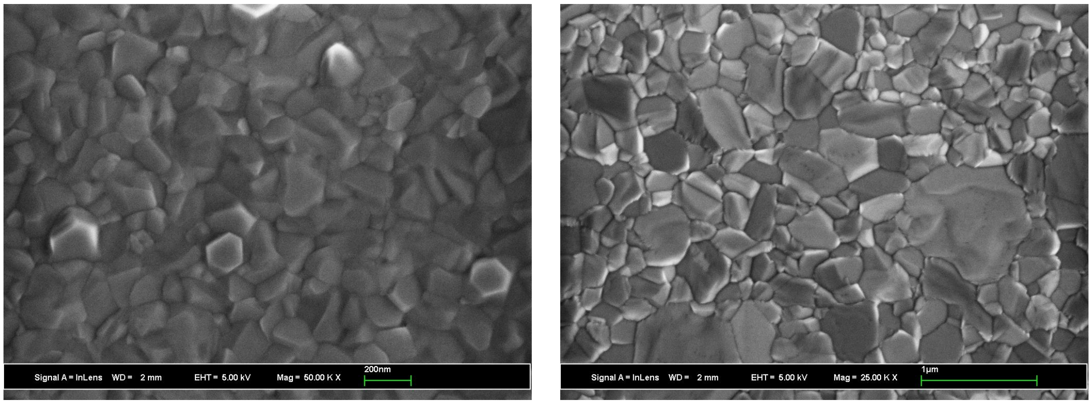
c) Pt @ 300C

d) Pt @ 500C

Figure 3.5 Pt film plan view SEM images

3.1.1.2 Lineal intercept average grain size

The grain size information was extracted from each plan-view image using the ImageJ software package. Four lines were drawn across each image, counting the grain boundary intersections with each line. The average grain size, D, could be estimated as a circular diameter following the calculation of $D = \frac{Line\ Length}{GB\ Intersections}$. This follows the lineal intercept method of ASTM E112-13. An example image with four intercept lines is shown in Figure 3.6.

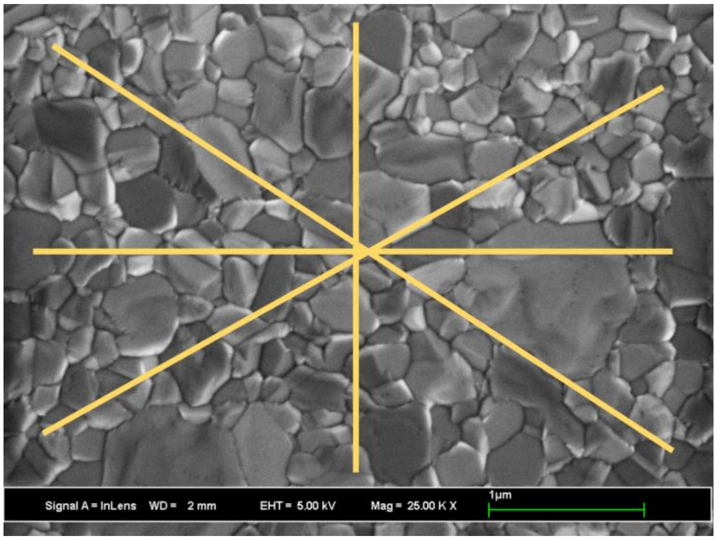

Figure 3.6 Example ImageJ procedure using modified lineal intercept method

The results of each metal average grain size measurement are tabulated in Table 3.1. The grain size is plotted against sputtering temperature in Figure 3.7. Each FCC metal shows a linear increase in grain size with sputter temperature. The Au and Pt film could be sputtered at relatively higher temperatures because they maintained smooth surface finishes during high temperature deposition while Ag, Al(Mg), and Cu films began to roughen above the maximum temperatures listed in Table 3.1.

Material	Thickness (nm)	Sputter Temperature (C)	Average Grain Size (nm)
Al- (<1%) Mg	500	100	111.8
		150	278.4
		200	371.8
Ag	500	100	168.05
		125	210.01
		150	223.38
		175	312.8
		200	334.5
Au	670	100	122.9
		175	284.0
		300	658.7
		400	878.4
Cu	500	100	31.9
		200	191.4
		300	412.5
Pt	500	150	44.8
		200	60.4
		300	151.5
		500	264.1

Table 3.1 Average grain size for all FCC metal films

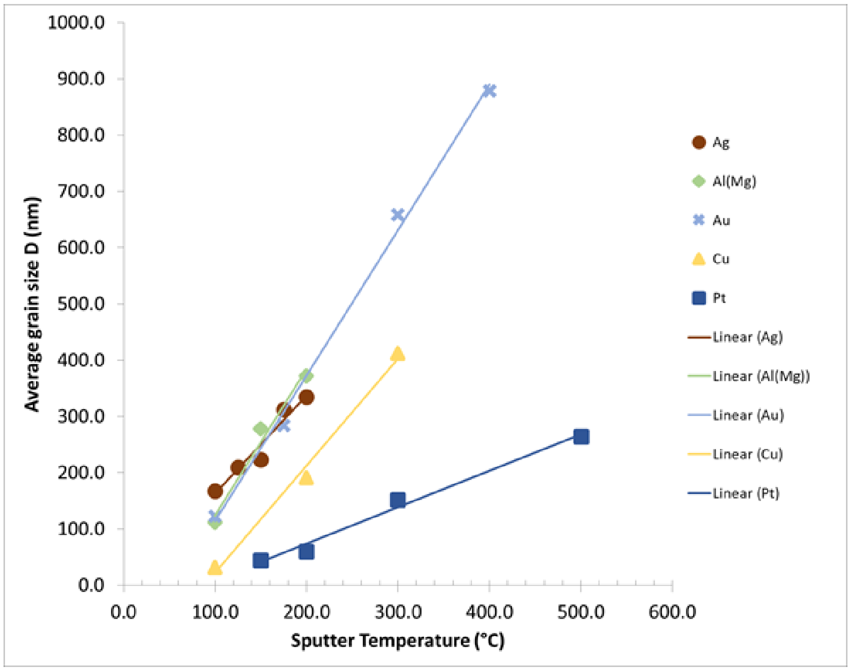

Figure 3.7 Average grain size measurements with sputtering temperature

3.1.1.3 FIB analysis

The Focused Ion Beam (FIB) of a Scios SEM/FIB dual beam was used for creating TEM samples (Section 3.1.1.4) and for verifying the columnar nature of grain growth for the FCC film set of this study. Figure 3.8 shows the cross-sectional FIB images taken for coarse-grained polycrystalline metals and the single crystal film. Columnar growth is evident for each film from SiN_x (bottom of each figure) substrate to the film surface on the top. It is also clear from these images that the Al(Mg) and Pt films show no evidence of growth twinning, Au and Cu films show moderate twinning, and Ag polycrystalline films show the highest density of twinning. The single crystal film shows a mostly single crystal film with some twins. The qualitative amount of growth twinning depends on the stacking fault energy (SFE) of the depositing species with the lower SFE materials (Au, Cu, Ag) having the highest twin densities, as expected [27,82].

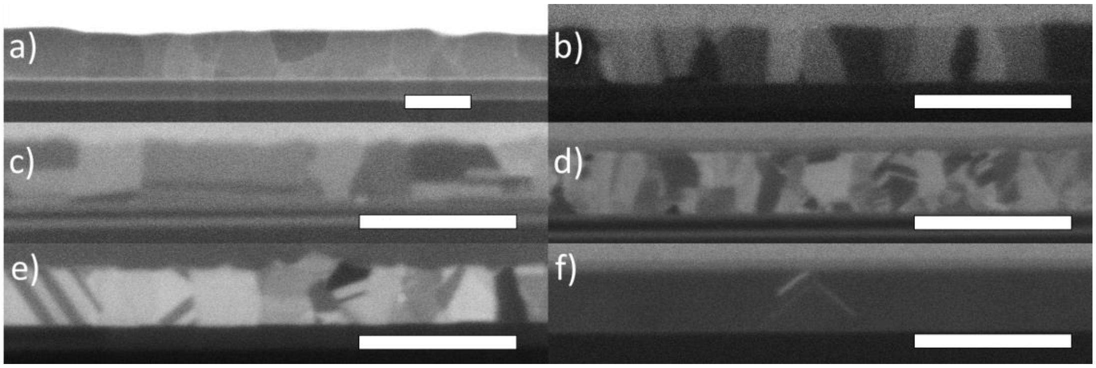

Figure 3.8 FIB cross sections a) Al(Mg) b) Pt c) Au d) Ag e) Cu f) Ag single crystal. Scale bars 500 nm (small) and 1 micron (large)

3.1.1.4 TEM analysis

Transmission electron microscopy (TEM) was used to study dislocation density and to analyze the cross-sectional and plan-view images at a finer scale than can be achieved via SEM imaging. Plan view TEM images of the Al(Mg) samples are shown in Figure 3.9. The Al(Mg) foils were thinned to about 150 nm thick, which was sufficient for 120 kV electron transmission. The Al(Mg) 100 °C fine sample and 200 °C coarse sample are shown in this figure at the same magnification. The grain size difference is obvious, and there is no evidence of growth twins seen in either sample. This matches the lack of twin formation evidence as seen in SEM imaging of the high-SFE aluminum samples.

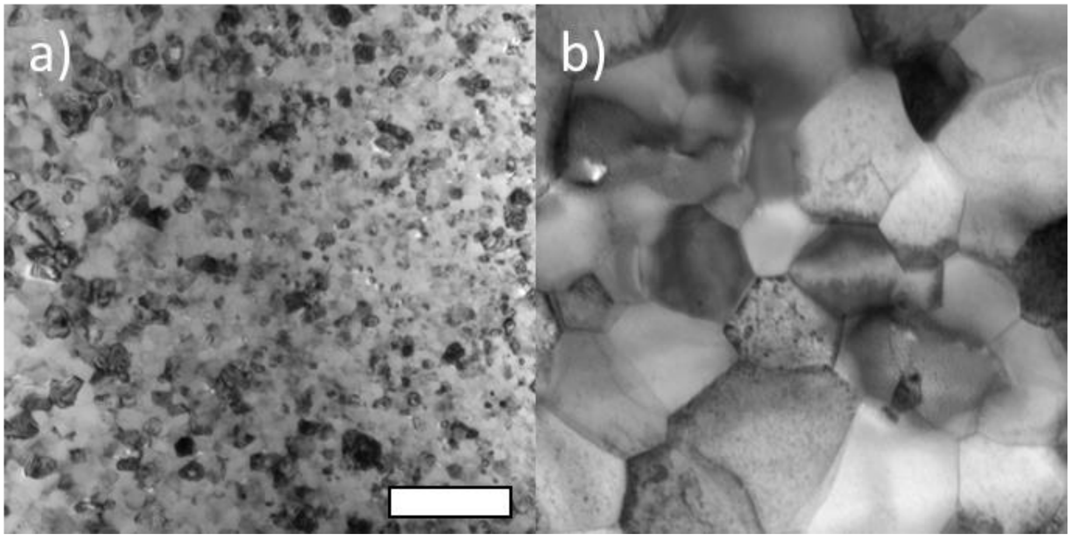

Figure 3.9 Plan View Al(Mg) TEM images of a) 100 °C b) 200 °C. Scale bar 500 nm

Au plan view TEM samples are shown in Figure 3.10, with a Au 100 °C fine sample and a Au 400 °C coarse sample. These samples were thinned to about 50 nm to allow for 200 kV electron transmission in the TEM. Twins are evident in both films with a few growth twins clearly visible in Figure 3.10b.

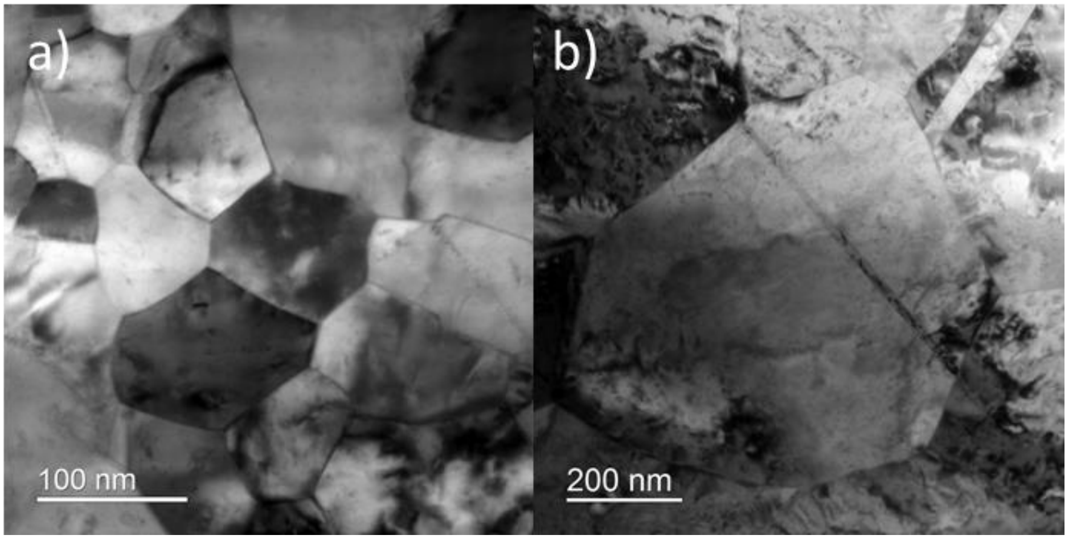

Figure 3.10 Plan view Au TEM images of a) 100 °C b) 400 °C

Cross-sectional TEM images were prepared for the three metal films with the lowest SFE: Ag, Au, and Cu. The comparison of these films is shown in Figure 3.11 with the SiN_x substrate on the bottom of each figure for reference. The Ag film appears to contain a higher density of growth twins than the Au and Cu, which have comparable densities of twins in these images. More in depth TEM work would be needed to quantify the twin density beyond the subjective analysis presented here.

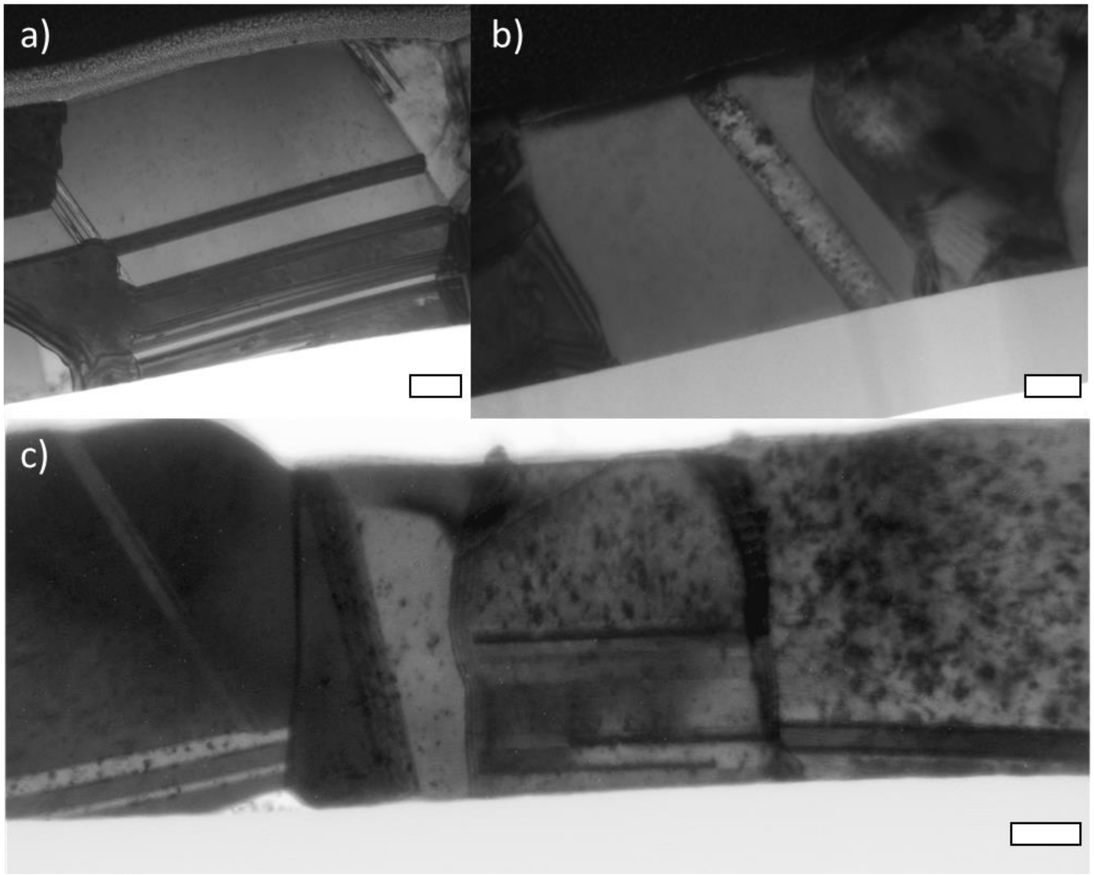

Figure 3.11 Cross-sectional TEM images of a) Ag 200 °C b) Cu 200 °C and c) Au 400 °C. Scale bars 100 nm

3.1.1.5 Texture analysis

During film growth, the nucleated adatom islands with the densest packed planes are the first to coarsen and consume other islands [23]. For FCC metals this typically leads to a preferred orientation with a higher fraction of one orientation than would be expected in a conventional polycrystalline material. The preferred orientation is known as texture, and many sputtered FCC films will have a (111)-fiber oriented texture.

The texture of all films was measured via XRD powder scans. An example of 2-theta scans from each metal film is shown in Figure 3.12. As expected, each polycrystalline film shows a high intensity of the (111) peak relative to other crystal orientations. In several cases no other peak is visible. All polycrystalline films were deposited on amorphous SiN_x so no epitaxially orientation is expected, and surface energy minimization should dominate. However, in Figure 3.12e, a (200) preferred orientation for the Ag single crystal film is shown. This film was grown epitaxially on (100) Si surface so a single crystal of this preferred orientation was expected.

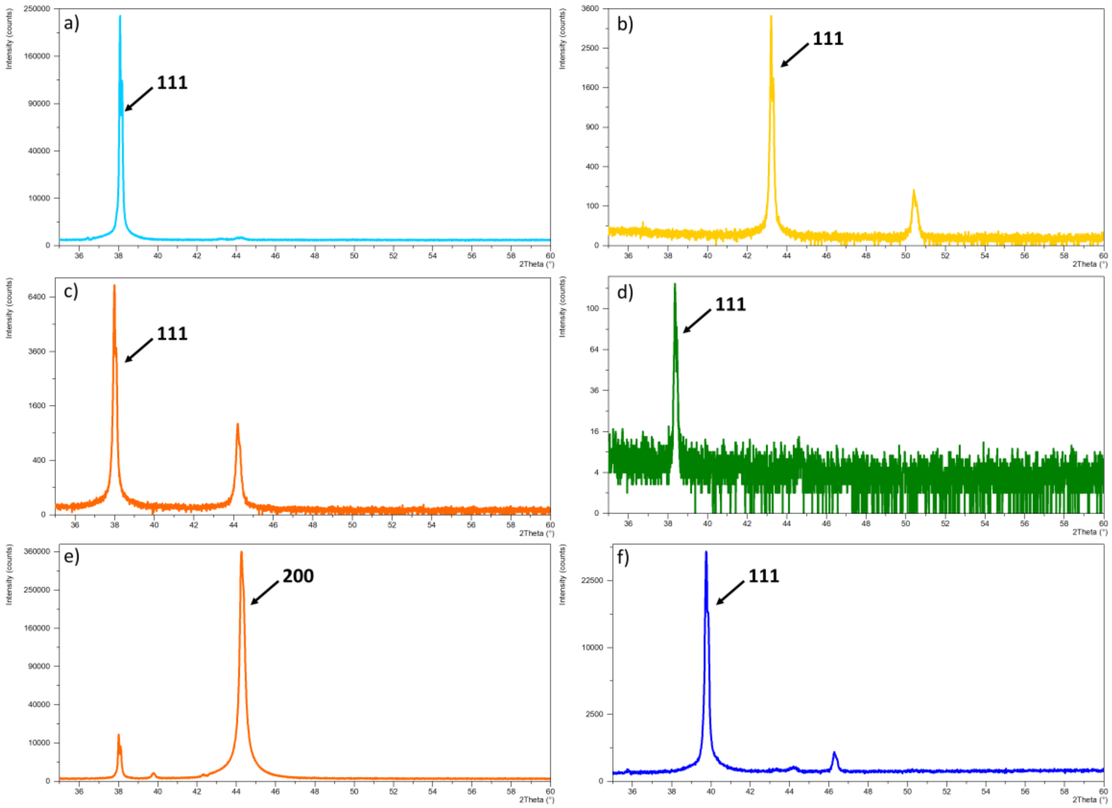

Figure 3.12 XRD powder scans of FCC films a) Au b) Cu c) Ag d) Al(Mg) e) Ag single crystal and f) Pt

The XRD powder scans can be further analyzed quantitatively to gain a more accurate measure of the texture. The diffracting crystal planes were determined using Bragg's Law:

$$d_{hkl} = \frac{\lambda}{2\sin\theta} \qquad \textbf{(3.1)}$$

Where the incident x-ray Cu Kα wavelength is λ = 0.1540598 nm. FCC metal extinction rules dictate that only planes with all odd or all even (hkl) indices will meet diffraction conditions so the {111} and {200} peaks will appear, but not the {100}. Knowing the lattice constant (a) for each material, the (hkl) reflections in the scans can be systematically identified using the following formula:

$$d_{hkl} = \frac{a}{\sqrt{h^2 + k^2 + l^2}} \tag{3.2}$$

Diffraction intensity depends on {hkl} so even in a film with truly random grain orientations the peaks in a 2θ scan will not be the same height. The peak intensities for each scan were therefore normalized by that of the (111) peak for that case for comparison to a random polycrystalline FCC bulk material that was normalized in the same way. This is shown in Figure 3.13 with the random standard shown in grey [83–85] plotted in arbitrary intensity units. The {200} intensities of the scans are all smaller than that of the random film, and the other orientations are nearly non-existent. Therefore all films show a predominant (111) texture, with the Au and Pt films having the highest relative ratio of $\frac{(111)}{(200)}$. The Ag, Al(Mg), and Cu films are also highly (111) textured, but a considerable fraction of the grains in each film have other orientations as well.

While there are differences in texture among the films, no large, systematic dependence on film type or deposition temperature was observed. It is therefore safe to assume that differences in relaxation are very unlikely to be caused by texture differences.

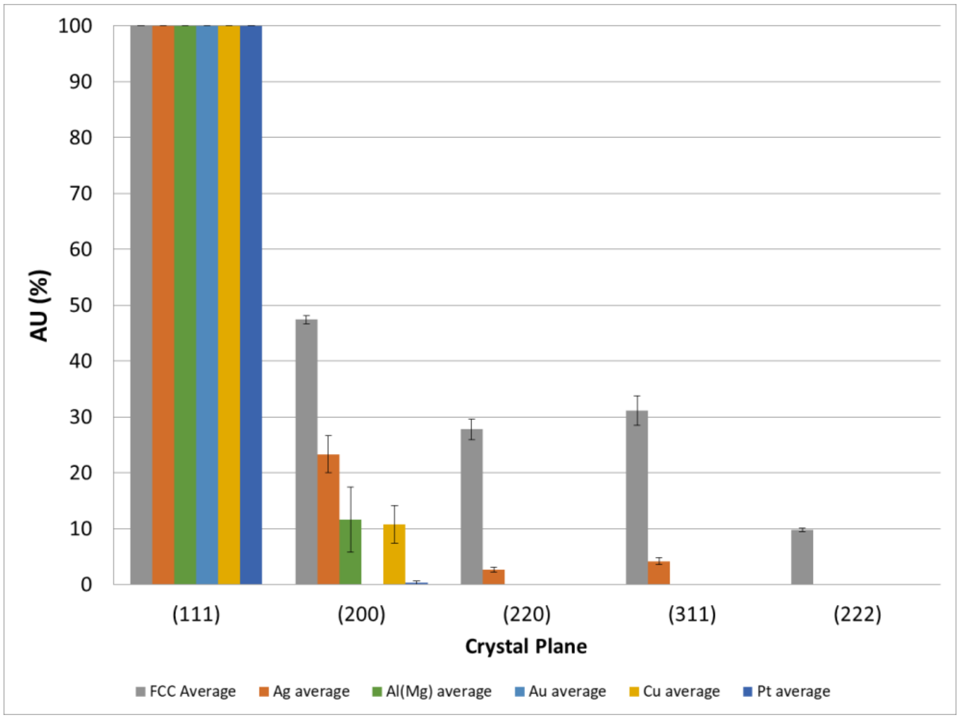

Figure 3.13 Texture comparison between polycrystalline films (colors) and bulk standards (grey)

3.1.2 Polycrystalline relaxation behavior

To classify the time-dependent mechanical response of the FCC metal films a series of bulge tests was performed, once per day for a span of 3 or 4 days. The series of tests included an elastic loading ramp followed immediately by unloading to determine the residual stress (σ_0) and plane strain modulus (M_{ps}) of each film. The next test in the daily test series was the 3-hour relaxation test under a constant hoop strain of 0.1%. A sufficient anelastic recovery process of about 1 day (~24 hrs) was provided between each test series. All tests were performed at 80 °C by heating the bulge chamber with a resistive heater.

3.1.2.1 Conditioning to achieve a viscoelastic state

As-sputtered metallic films have been shown to comprise both unrecoverable (viscoplastic, VP) and recoverable (viscoelastic, VE) components in low-strain environments [6,7]. By running the test series (ramp and iso-strain tests) once per day for a few days, it is possible to exhaust the viscoplastic component of stress relaxation and investigate solely the viscoelastic component. From a practical standpoint, a MEMS designer would need to design precautions for larger relaxations in early cycles (when VP and VE components are active) and plan for persistent, recoverable VE relaxation behaviors over the lifetime of the device. The following figures will describe a typical series of tests performed on a Au film.

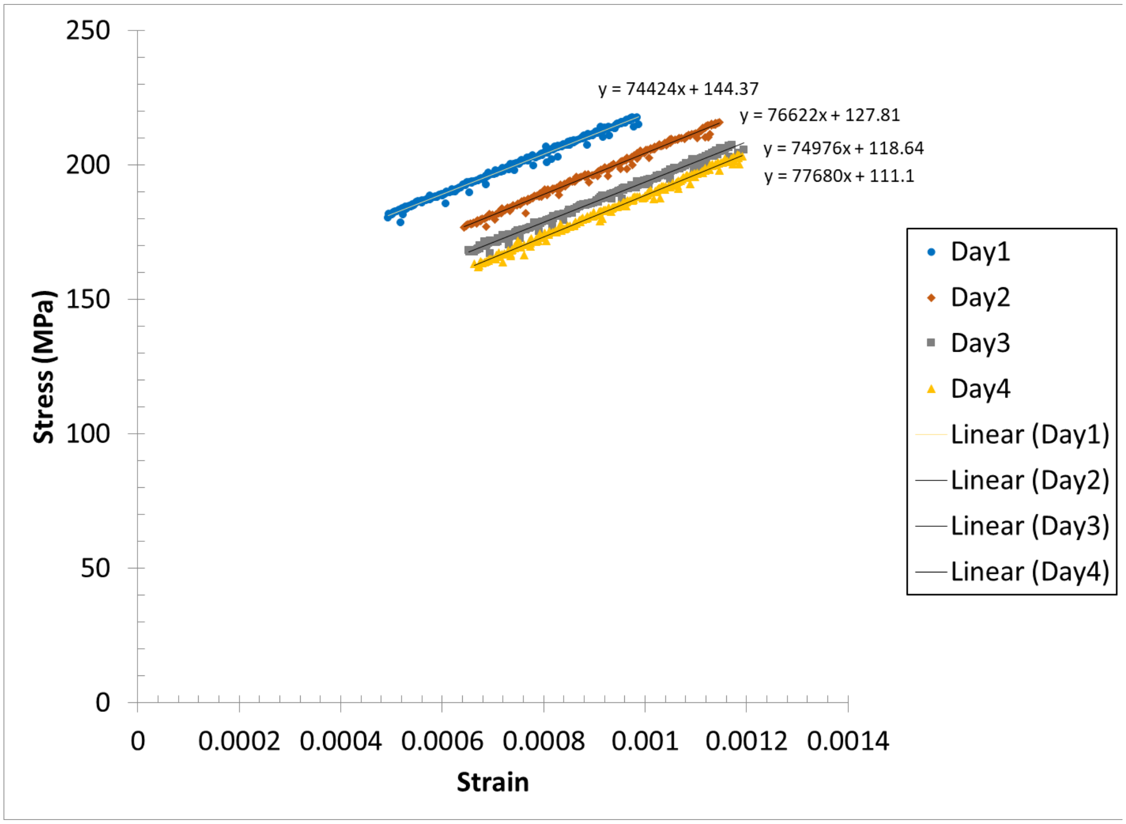

Figure 3.14 Typical elastic stress-strain response of FCC film over 4-day period

The first part of each day's test series, the elastic loading/unloading ramp, is shown in Figure 3.14. This figure represents a linear unloading segment of the full stress-strain curve. Four linearly elastic curves are displayed, one for each day. The slope of the line is the plane strain modulus and the y-intercept is the biaxial residual stress. As expected, the modulus for each film remains relatively constant from each test as indicated by the similar slopes. However, the residual stress is shown to decay from Day 1 to Day 2 until it reaches a nearly steady state between Day 3 and Day 4 as indicated by the similar intercepts in the later tests. The decreasing change of residual stress from one day to the next is due to the exhaustion of the viscoplastic component of relaxation. Most of this exhaustion typically occurs in the testing between Day 1 and Day 3, and only viscoelasticity remains from Day 3 onward. The hysteresis behavior depicted in the schematic of Figure 2.20a is reflected in the stress-strain plots of Figure 3.14. It can then be said that the film recovered fully after the Day 3 ramp and iso-strain relaxation tests and performed nearly identically on Day 4. The Day 3 to Day 4 repetitive mechanical response is the core evaluation metric to compare viscoelastic relaxation behavior for all metal films in this work.

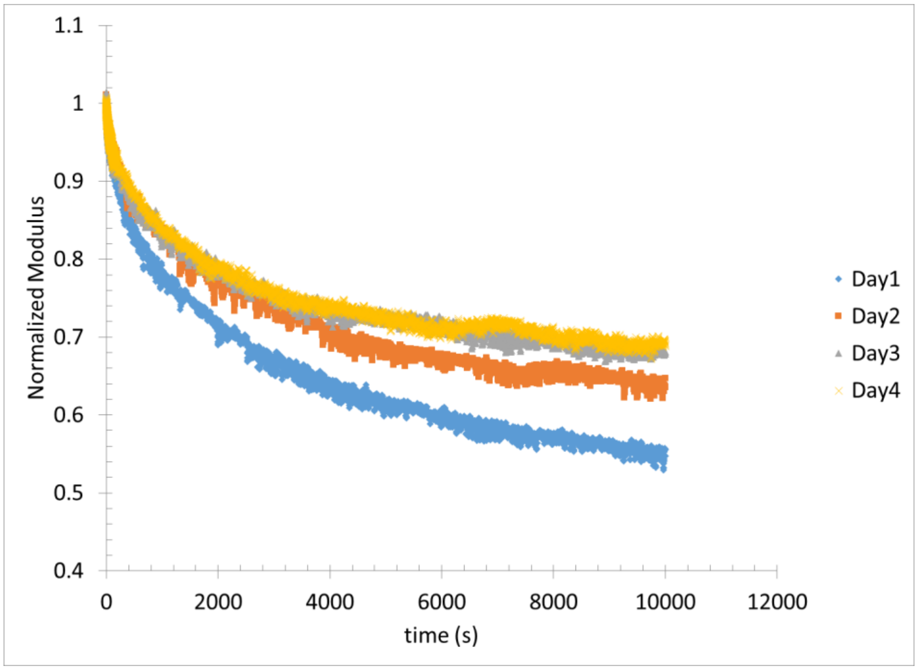

Figure 3.15 Typical iso-strain relaxation response over 4-day period

Typical iso-strain relaxation tests for each day are shown in Figure 3.15. The film is bulged to nominally 0.1% hoop strain and the stress relaxation is measured with time $\sigma_{hoop}(t) = M_{ps}(t) \cdot (0.001)$. The relaxation of the modulus is normalized to the unrelaxed modulus (and labeled Normalized Modulus) and plotted in Figure 3.15. The relaxation response of Day 1 is larger than the following days as this film has yet to exhaust the viscoplastic components of relaxation. By Day 3 and Day 4 only the viscoelastic component remains, as evidenced by the similar relaxation response for these two days. This also follows the schematic of Figure 2.20b,c.

The steady state viscoelastic response of Day 4 in Figure 3.15 will be used for comparison among the five FCC metals discussed in this chapter. The modulus of the film (i.e., the stiffness) is highest at the beginning of an iso-strain test (t = 0 s, NM =1) and decays to a certain point at the end of the test where t = 10,000 s. The extent of modulus decay, or relaxation response metric, is as follows:

$$Extent\ of\ Relaxation = \frac{M_{ps,(t=10{,}000)}}{M_{ps,(t=0)}} = NM_{(t=10{,}000)} \tag{3.3}$$

Where M_{ps} is the plane strain modulus and NM is the normalized modulus. This will be the comparison metric for evaluating the FCC metals under the same loading conditions. Another useful parameter is the percent relaxation of the film after 10,000 seconds which is simply:

$$\%\ Relaxed = 100 \cdot \left(1 - NM_{(t=10{,}000)}\right) \tag{3.4}$$

The logarithmic nature of the stress relaxation curves shown Figure 3.15 can be modeled using a 4-term Prony series, which is a sum of 4 exponential decay functions. All viscoelastic (VE) relaxation responses were fit using the following:

$$NM(t) = 1 - \sum_{i=1}^{4} P_i \left(1 - e^{\frac{-t}{\tau_i}}\right) \tag{3.5}$$

Where P_i is the i'th Prony constant and τ_i is the i'th time constant. The time constants were set at τ = 10, 100, 1000, and 10,000 seconds for each film. The time constants are not evenly spaced in time (i.e. every 2,500 s) and are more heavily weighted in the early relaxation stages. This was done since the relaxation behavior is more rapid in the early stages and the fit is more accurate with this type of weighting strategy. The Prony constants are determined using least square fitting of Prony series equations to normalized modulus relaxation curves.

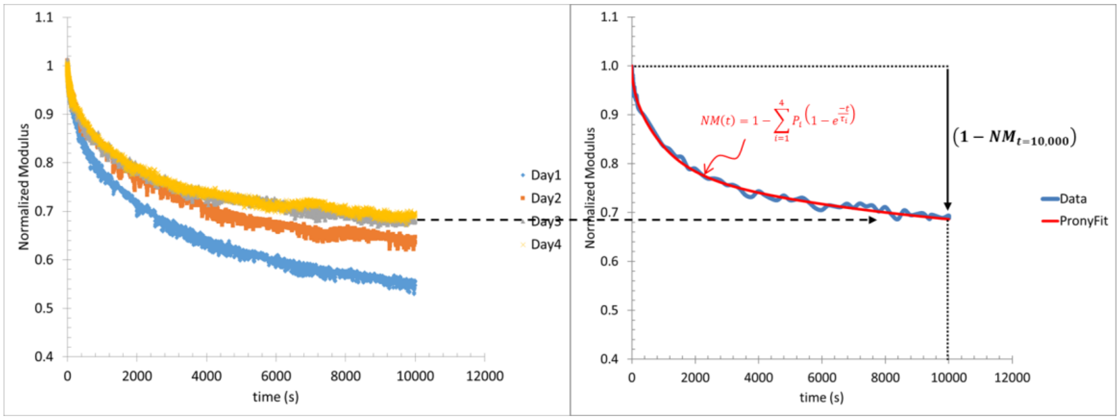

Figure 3.16 Typical 4-term Prony series fit of viscoelastic relaxation curves

Figure 3.16 shows a 4-term Prony series fit of the steady state viscoelastic relaxation from Day 4 in Figure 3.15. The red curve represents the Prony fit and the blue curve is the raw relaxation data from this iso-strain bulge experiment. The amount relaxed is also highlighted at the 10,000 second mark of this figure.

a) Ag

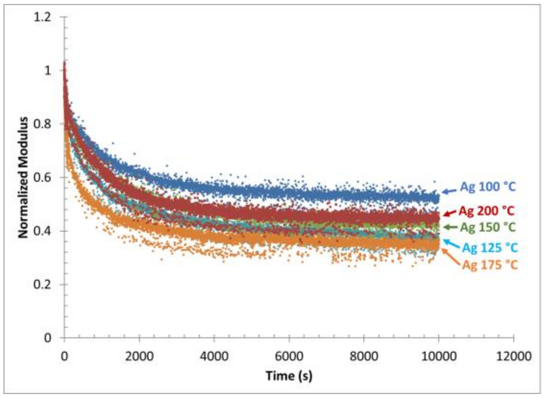

b) Al(Mg)

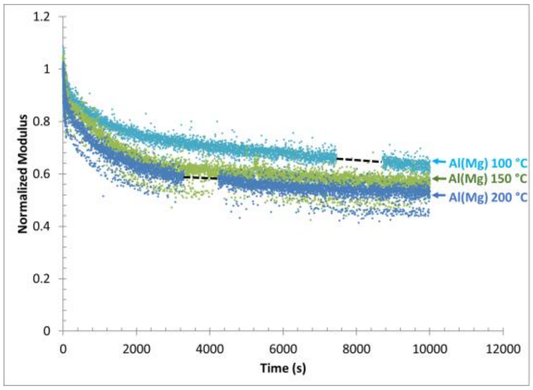

c) Au

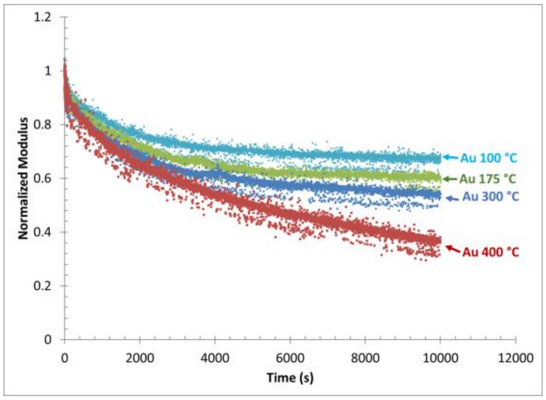

d) Cu

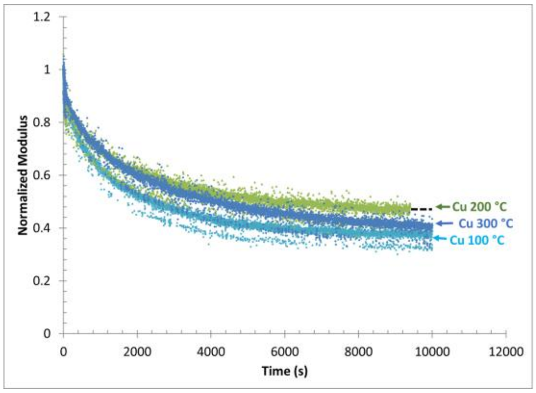

e) Pt

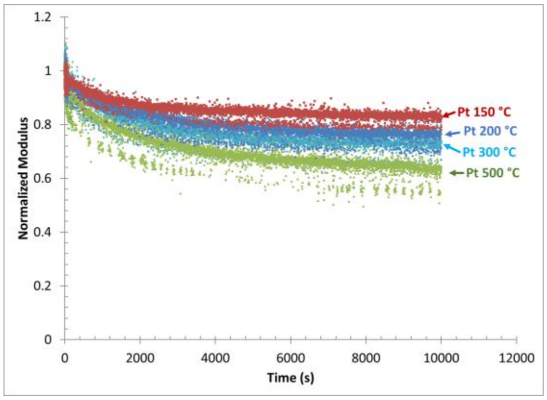

Figure 3.17 Steady state viscoelastic relaxation curves for all FCC metals

a) Ag

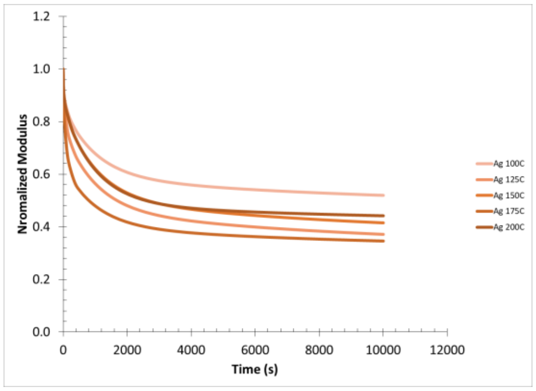

b) Al(Mg)

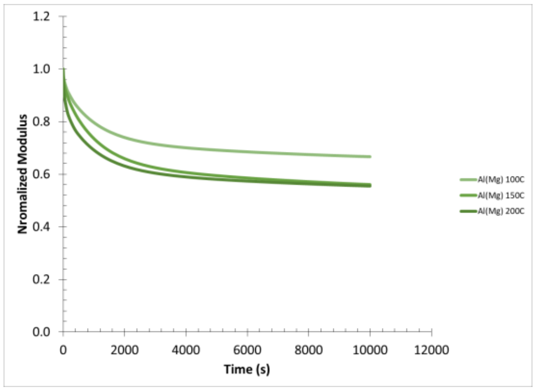

c) Au

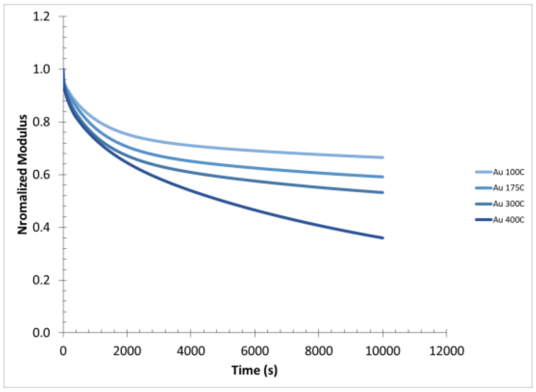

d) Cu

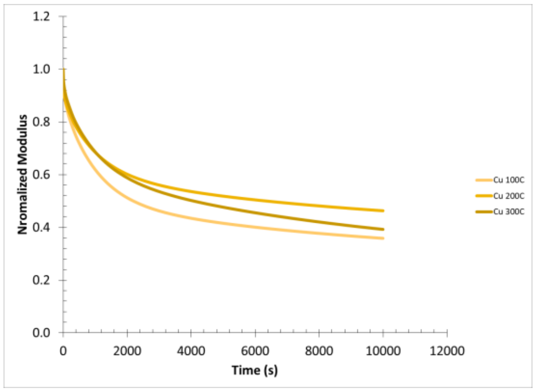

e) Pt

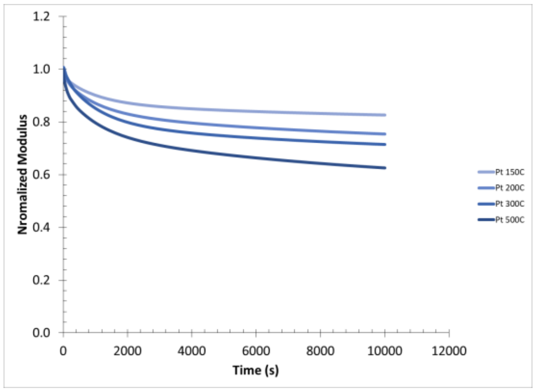

Figure 3.18 Prony fits for viscoelastic relaxation

The steady state viscoelastic relaxation curves for each metal film are depicted in Figure 3.17. Each of these films went through the bulge test series, once per day, until only viscoelastic relaxation was measured. The sputtering temperature is called out next to each curve. The grain size is proportional to the sputtering temperature and so this figure shows that the relaxation of the Ag and Cu films is insensitive to increasing sputtering temperature (and grain size). The Al(Mg), Au, and Pt films appear to follow a trend of increasing relaxation with increasing grain size. Dashed black lines in the Al(Mg) and Cu curves represent spurious electrical malfunctions of the lock-in amplifier, where the data was unusable and was removed from the curve. Dummy data points were added to assist in the subsequent fitting.

The bulge data from iso-strain relaxation tests is fit using the four term Prony series, using Equation (3.5). Fitting to a Prony series enables easier understanding of relaxation behavior by eliminating the presence of noise. All further bulge data curves will be presented as Prony fits to clarify the mechanical response. Figure 3.18 shows the Prony fits for all the relaxation curves from Figure 3.17. The curves are color coded, and an increase in color intensity indicates increased sputtering temperature (and grain size). The Prony series constants extracted from Figure 3.18 are tabulated in Table 3.2.

Material	Sputter T	P_1	P_2	P_3	P_4
		$\tau = 10s$	$\tau = 100s$	$\tau = 1000s$	$\tau = 10{,}000s$
Ag	100	0.07805	0.06416	0.26595	0.11433
	125	0.09079	0.13657	0.30641	0.15073
	150	0.08474	0.06464	0.34008	0.15040
	175	0.09200	0.27193	0.23399	0.08948
	200	0.08097	0.06144	0.36858	0.07406
Al(Mg)	100	0.02454	0.03741	0.20773	0.09996
	150	0.03520	0.03880	0.27990	0.13510
	200	0.05988	0.09604	0.22499	0.10191
Au	100	0.04005	0.01407	0.19341	0.13779
	175	0.04878	0.00450	0.23991	0.18188
	300	0.04656	0.03192	0.23908	0.23834
	400	0.03646	0.06736	0.16759	0.58260
Cu	100	0.07184	0.04876	0.37594	0.22893
	200	0.07583	0.04281	0.27629	0.22486
	300	0.04208	0.05050	0.29685	0.34505
Pt	150	0.01805	0.01104	0.09894	0.07246
	200	0.00258	0.03307	0.12806	0.13099
	300	-0.02043	0.04077	0.18090	0.13212
	500	0.01353	0.06696	0.16216	0.20869

Table 3.2 Prony series constants for relaxation fit

The comparison metric for viscoelastic behavior is extracted from the Prony fits for each film using Equation (3.3). This data point will be the primary means of evaluating any grain size effects in FCC metal films and a core facet of this work. This information along with other extracted film mechanical properties (M_{ps} and σ_0) are tabulated in Table 3.3.

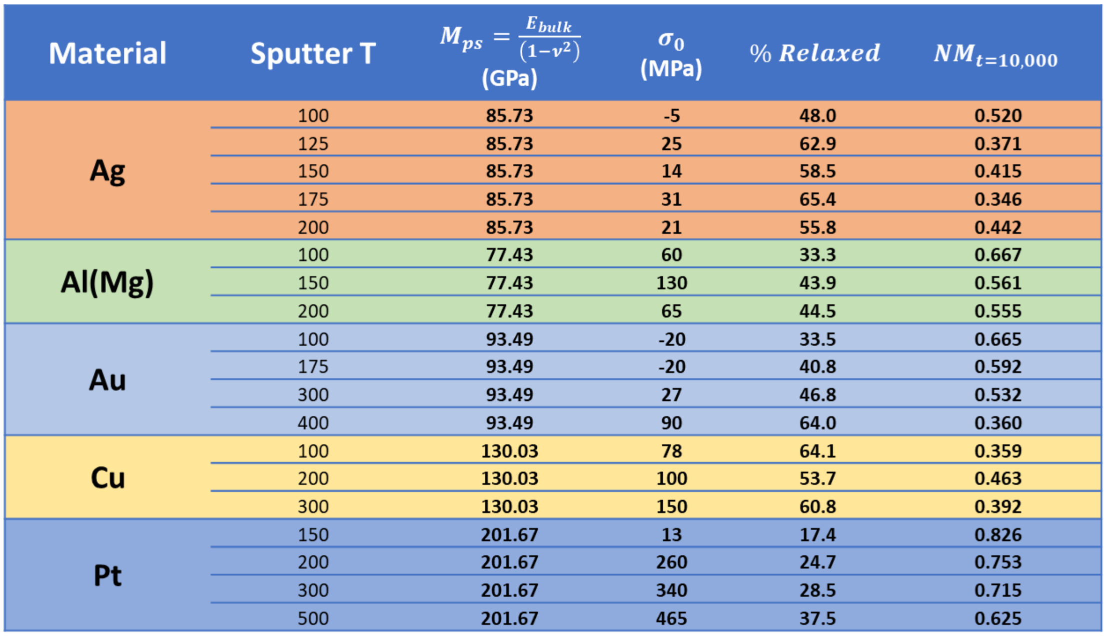

Material	Sputter T	$M_{ps} = \frac{E_{bulk}}{(1-\nu^2)}$ (GPa)	σ_0 (MPa)	$\% \, Relaxed$	$NM_{t=10,000}$
Ag	100	85.73	-5	48.0	0.520
	125	85.73	25	62.9	0.371
	150	85.73	14	58.5	0.415
	175	85.73	31	65.4	0.346
	200	85.73	21	55.8	0.442
Al(Mg)	100	77.43	60	33.3	0.667
	150	77.43	130	43.9	0.561
	200	77.43	65	44.5	0.555
Au	100	93.49	-20	33.5	0.665
	175	93.49	-20	40.8	0.592
	300	93.49	27	46.8	0.532
	400	93.49	90	64.0	0.360
Cu	100	130.03	78	64.1	0.359
	200	130.03	100	53.7	0.463
	300	130.03	150	60.8	0.392
Pt	150	201.67	13	17.4	0.826
	200	201.67	260	24.7	0.753
	300	201.67	340	28.5	0.715
	500	201.67	465	37.5	0.625

Table 3.3 Extracted film mechanical properties from bulge test

3.1.2.2 Residual stress trends

Figure 3.19 shows the steady-state residual stress measured at 80 °C for each film type. The Pt residual stress is strongly dependent on T_{dep}, changing by over 450 MPa from the lowest to the highest temperature. The Ag, Au, and Cu show a weak dependence, changing by 100 MPa or less, while the Al(Mg) shows no clear trend at all. The Ag and Au films deposited at lower temperatures are in compression due to the expansion of the metal films that took place when heating to 80 °C from room temperature. All of the films would be in tension at room temperature, as expected.

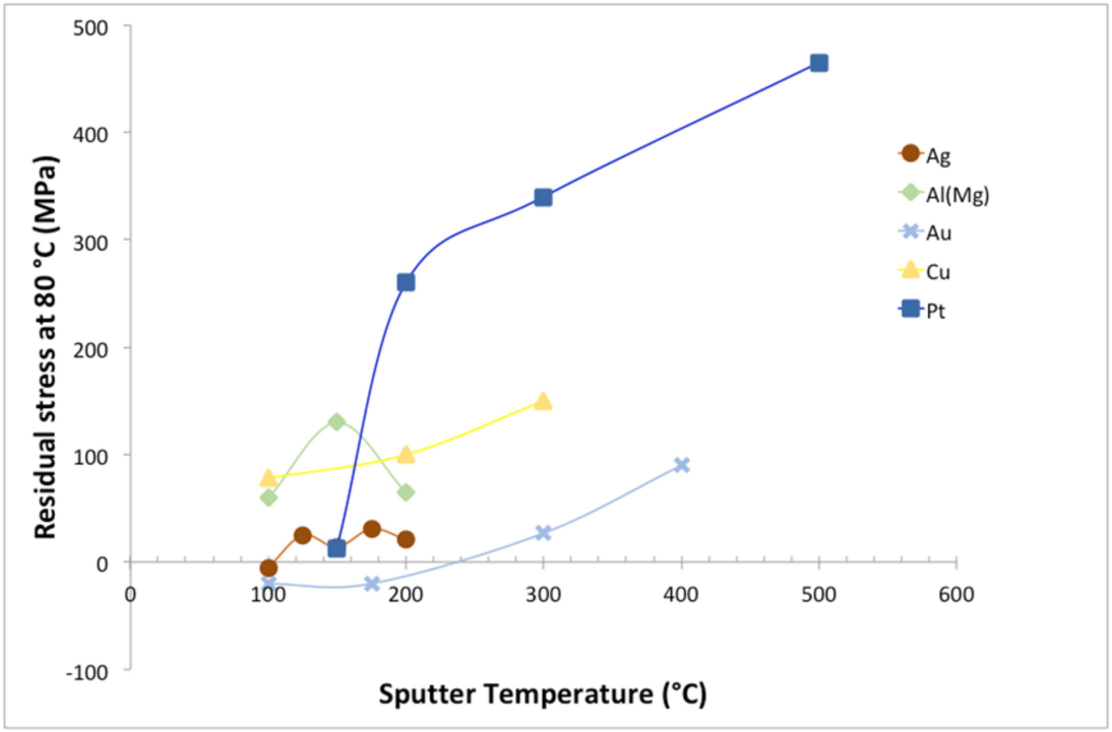

Figure 3.19 Steady-state residual stress at 80 °C as a function of sputter temperature

By plotting the normalized relaxed modulus against the metal residual stress, as in Figure 3.20, it is apparent that the relaxation behavior of the Ag, Au, and Pt films has a negatively sloped linear trend with increasing residual stress. Thus, the highly-stressed Pt has a lower effective modulus than low-stress Pt, for example. At first glance this implies that increasing tensile residual stress enhances relaxation for three of the films and compressive stress contributes to relaxation resistance. This trend is not apparent for Al(Mg), but this may not be surprising since that set of films did not exhibit a clear trend of σ_{res} vs. T_{dep}. The Cu films also failed to show a correlation which is more difficult to explain given that the residual stress rose with increasing T_{dep} just like the Ag, Au, and Pt.

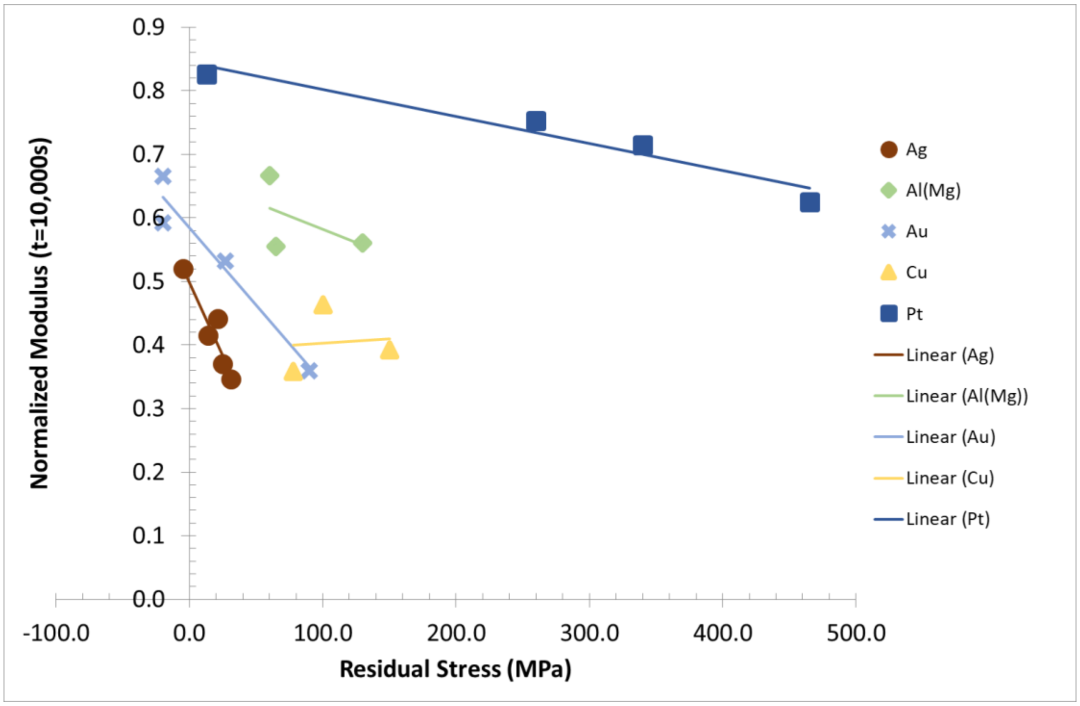

Figure 3.20 Relaxation behavior with film residual stress

Despite the initial appeal of a model in which tensile residual stress aids the relaxation process, there are several reasons why this is very unlikely. First, prior work has shown that the metal film behavior obeys linear viscoelastic elasticity, which means that every applied stress contributes independently to the stress relaxation. This is incompatible with the concept of residual stresses driving relaxation as measured by the bulge test. Second is the lack of correlation between residual stress level and the measured Cu relaxation behavior. There is no obvious reason why Cu would behave differently than the other FCC metals on the list given that its melting point and stacking fault energy values are very similar to Ag and Au. The third, and final, problem with the residual stress model is the linear behavior of the Pt relaxation when the residual stress change was highly non-linear. If the residual stress is driving relaxation, there should be a very large change in behavior of the Pt, particularly between the films deposited at 100 °C and 200 °C. All together, these issues support the idea that residual stress does not affect relaxation in any simple fashion.

It should be noted that although some metal films are in a compressive state (negative σ_0 value) at the 80 °C test temperature, the composite film is maintained in tension due to the SiN_x layer which is always in a state of tension. The metal residual stresses of Table 3.3 were extracted using the rule of mixtures.

3.1.2.3 Relaxation vs. grain size

Given that differences in roughness, texture, and residual stress cannot account for the observed differences in relaxation, grain size and dislocation structure remain as the most likely factors. In a previous study of pure Au, the normalized modulus was found to scale linearly with D^2. Here, a range of exponents is considered as there is no clear model to motivate a D^2 proportionality, per se. The iso-strain relaxation extent ($NM_{t\,=\,10,000\ s}$) is therefore plotted against various combinations of grain size, D, to the n^{th} power where n ranges from n = -½, ½, 1, 2, 3. The case of n = -½ corresponds to a Hall-Petch trend while the other exponents are closer to the prior finding of n = 2.

Cu and Ag failed to show a clear trend with D^n regardless of n. Linear regression assuming n = -½ and n = 3 was poor for the other three materials as expressed by the correlation coefficient, R^2. The cases of n = ½, 1, and 2 showed reasonable linear trends for the relaxation behavior of the Au, Al(Mg), and Pt films. Figure 3.21 shows the linear relationship between NM and D^n where n ranges from ½ to 2. Data from Table 3.1 and Table 3.3 was used to construct these plots. Figure 3.21 suggests that Al(Mg), Au, and Pt films show a D^n relaxation response while Ag and Cu films appear to have relaxation behavior that is independent of grain size.

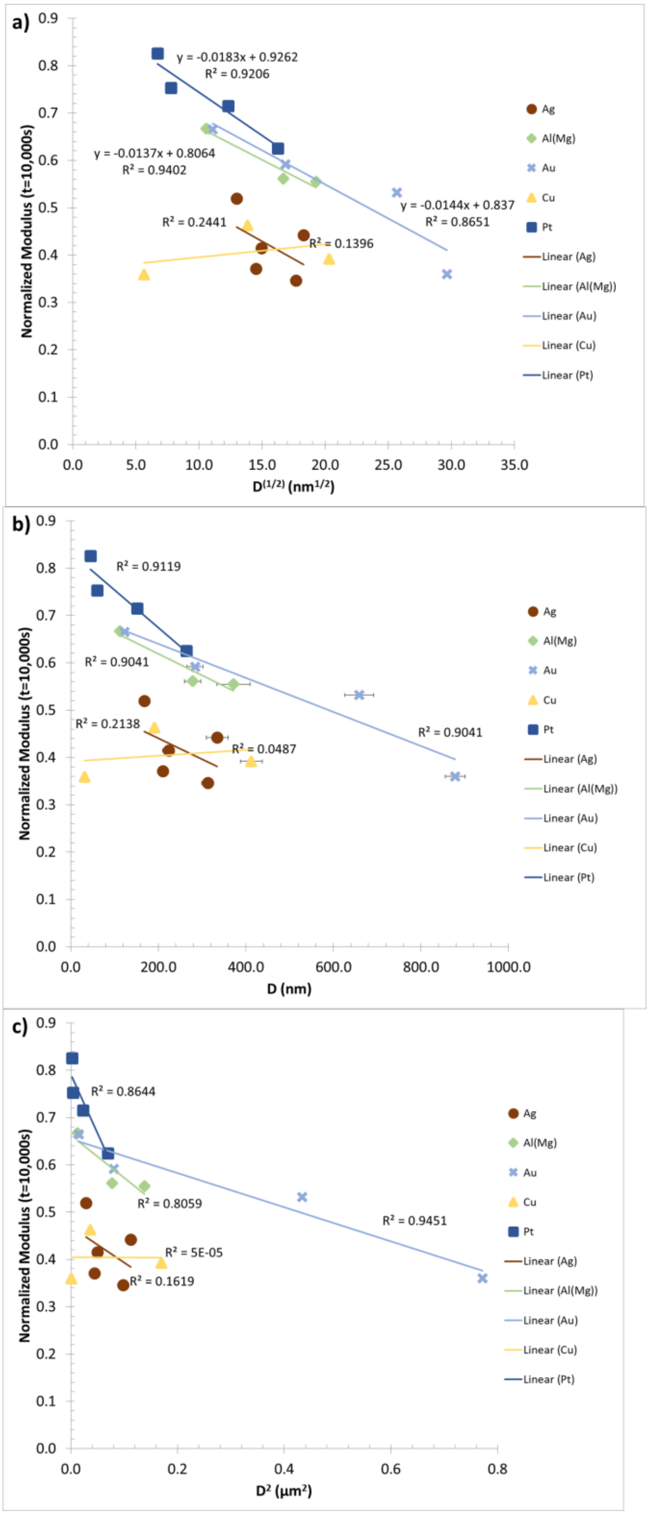

Figure 3.21 Relaxation behavior with D^n with a) n = ½ b) n = 1 and c) n = 2

The linear fits between relaxation and D^n grain size of Figure 3.21 shows certain trends among FCC metals that will be highlighted. The extraction of fitting parameters such as the slope and the R^2 value of the linear fit is displayed in Table 3.4. The grain size dependent metallic films (Al(Mg), Au, and Pt) have very similar slopes and high R^2 values when fit to $D^{1/2}$ suggesting this as a plausible linear relationship between relaxation and grain size. However, the fits when $n = 1$ and $n = 2$ show high R^2 values as well, suggesting a range of n values for FCC metals that show grain size dependence. This implies that some FCC metal films will show increased relaxation with grain size D^n, but not all FCC metals will have the same n values. For Al(Mg), Au, and Pt polycrystalline films the relaxation dependence is linearly proportional to D^n where n can range from ½ to 2. For Ag and Cu polycrystalline films, the relaxation behavior was shown to be independent of planar grain size. These results indicate that there is not a single, clear dependence on D that exists for all FCC materials. In turn, this implies that the mechanism behind the grain size effect is not an inherent feature of metallic materials like the Hall-Petch effect. Instead, it is likely that the changing grain size is accompanied by some other change in microstructure for the Al(Mg), Au, and Pt, but not for the Ag and the Cu. The likelihood of direct grain boundary strengthening is explored further in the next section.

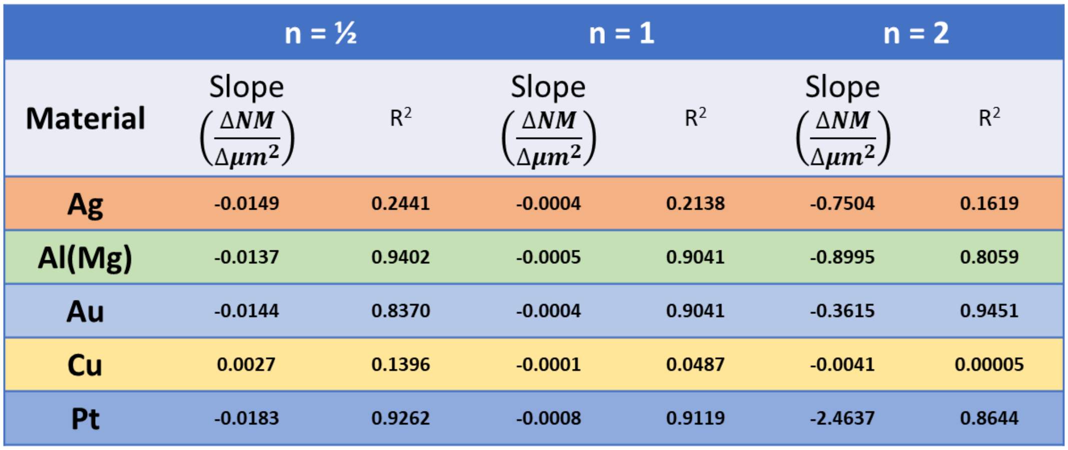

	n = ½		n = 1		n = 2	
Material	Slope $\left(\frac{\Delta NM}{\Delta \mu m^2}\right)$	R^2	Slope $\left(\frac{\Delta NM}{\Delta \mu m^2}\right)$	R^2	Slope $\left(\frac{\Delta NM}{\Delta \mu m^2}\right)$	R^2
Ag	-0.0149	0.2441	-0.0004	0.2138	-0.7504	0.1619
Al(Mg)	-0.0137	0.9402	-0.0005	0.9041	-0.8995	0.8059
Au	-0.0144	0.8370	-0.0004	0.9041	-0.3615	0.9451
Cu	0.0027	0.1396	-0.0001	0.0487	-0.0041	0.00005
Pt	-0.0183	0.9262	-0.0008	0.9119	-2.4637	0.8644

Table 3.4 Linear slope fitting results of $NM_{t=10,000s}$ vs D^n

3.2 Single crystal Ag

The work from Section 3.1 demonstrated that some FCC metal films will show increased relaxation as the grain size is increased. As the grain size is increased the density of grain boundaries for a given area of film decreases. In Hall-Petch strengthening mechanisms a higher density of grain boundaries provides more obstacles for dislocation motion or more dislocation sources, hardening the material in high strain environments. As this relaxation behavior is thought to be controlled by dislocation motion, it follows that a higher density of grain boundaries could also harden the material in low strain environments such as in relaxation tests. The grain boundaries could act as dislocation pinning sites, mitigating the extent of dislocation motions and reducing the viscoelastic relaxation. It could be argued that the high density of growth twins in the Ag and Cu films make the effective grain size smaller than it would appear (although this doesn't explain the case of Au, which also has growth twins).

To explore this theory further, this part of the chapter will describe the relaxation behavior of a Ag film with essentially zero grain boundaries (i.e., single crystal) and very few growth twins. This will test the D^n proportionality trend of Figure 3.21 to its maximum by utilizing an extreme of the grain size where there are no grain boundaries or other interfaces that could block dislocation motion. An infinitely large grain size area is the point where the grain size becomes sufficiently large that it is considered as a single crystal within the 12 mm by 3 mm bulge specimen relaxation area. This is shown schematically in Figure 3.22.

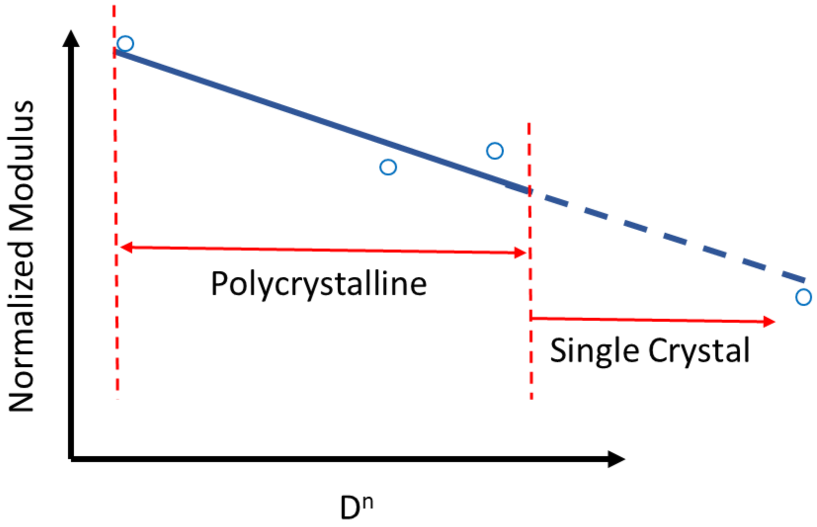

Figure 3.22 Single crystal relaxation hypothesis

Deposition of a single crystal film generally requires elevated temperature (~1000 °C) and direct contact between the metal film and a single crystal substrate. Au was ruled out for high temperature single crystal film growth due to the high diffusion rate of silicon into gold below the eutectic temperature [86]. Others have successfully grown single crystal Ag films to similar thickness ranges of this work [71,87] making it a promising candidate for iso-strain bulge testing. Ag does not have a low temperature eutectic with silicon and a negligible etch rate in KOH making it an ideal candidate for epitaxial growth on the silicon-based bulge test coupons that can also survive the harsh environment of wet etching. The epitaxial growth of single crystal Ag on (100) substrates of the bulge coupons follows the process steps of Figure 2.5.

3.2.1 Characterization of single crystal film

The plan-view and cross-sectional views of the single crystal Ag film were investigated in a similar manner to the polycrystalline films. In Figure 3.23a, a Zeiss in-lens SEM image shows the plan-view image of the Ag film to have a mottled contrast. Since the plan view images are inconclusive as to the presence or lack of grain boundaries, the FIB was used to verify the single crystal nature of the film, Figure 3.23b. No grain boundaries are evident in the cross-section, indicating that the Ag film appears to be single crystal.

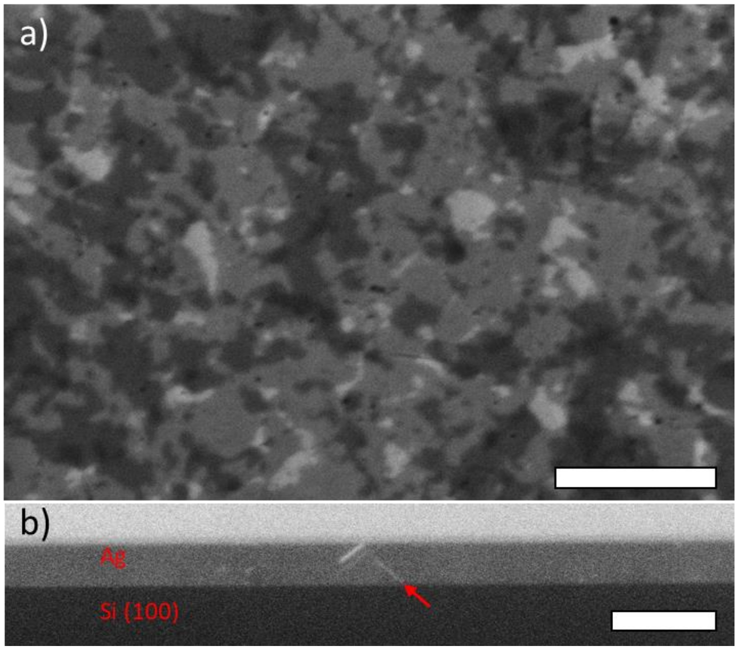

Figure 3.23 Single crystal Ag film in a) plan-view and b) cross section. Scale bars 1 micron. Twin depicted with arrow in b)

To further classify the crystallinity of the Ag film, an XRD analysis was performed. The 2-theta scan of Figure 3.24 shows the comparison of this single crystal Ag film against a polycrystalline Ag film. The epitaxial nature of the single crystal Ag film is evident in the strong (200) texture measurement, which is reasonable for a film that was grown on a (100) plane of a silicon wafer. As some other crystal planes are present, notably the (111) orientation signal, it is more appropriate to classify the film as mostly (100) single crystal Ag with some mis-oriented (111) grains.

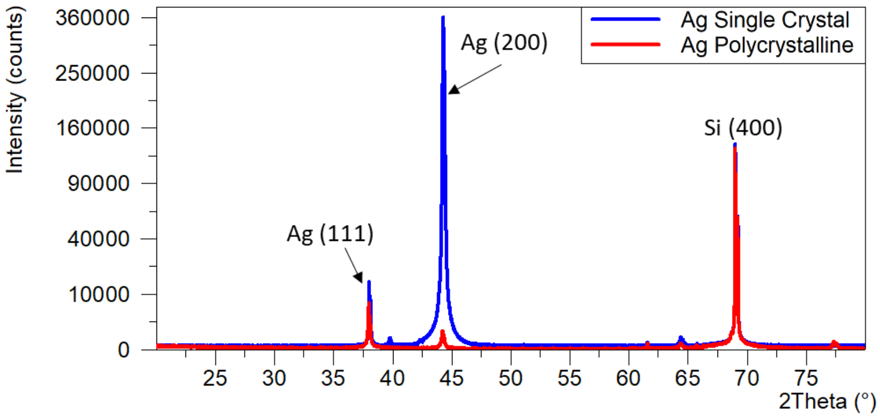

Figure 3.24 Single crystal vs polycrystalline XRD scans

Figure 3.25 compares the single crystal film texture against a bulk Ag polycrystalline standard, normalized by the intensity of the highest peak. In this figure the single crystal film is highly textured in the (200) orientation, signifying almost full epitaxial growth of a large (100) Ag grain on the (100) Si substrate.

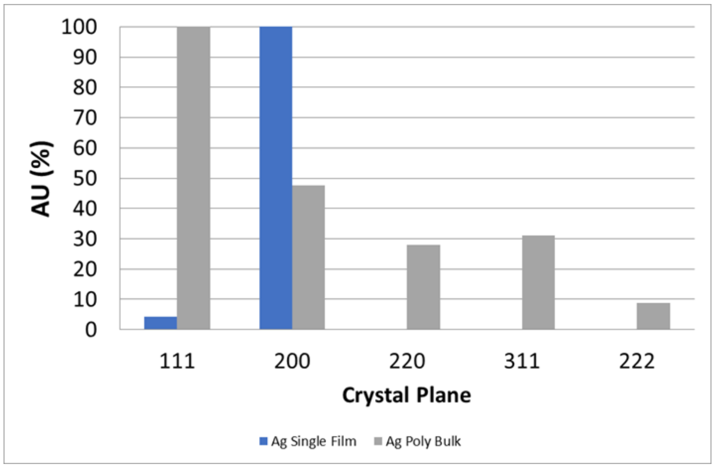

Figure 3.25 Single crystal Ag texture comparison

Electron Back Scatter Detection (EBSD) was also performed on the Ag single crystal film. Figure 3.26 shows a plan view mapping and Inverse Pole Figure (IPF), which shows that across a large scan area (~15 μm X 15 μm), the Ag film is oriented in the (100) configuration (red color coded). There are some areas that failed to index and others that showed a non-(100) orientation, but they are a minor fraction of the film surface. Note that the EBSD technique could only be used for the single crystal film as the polycrystalline films were too fine-grained to meet the resolution requirements of the incident SEM electron beam.

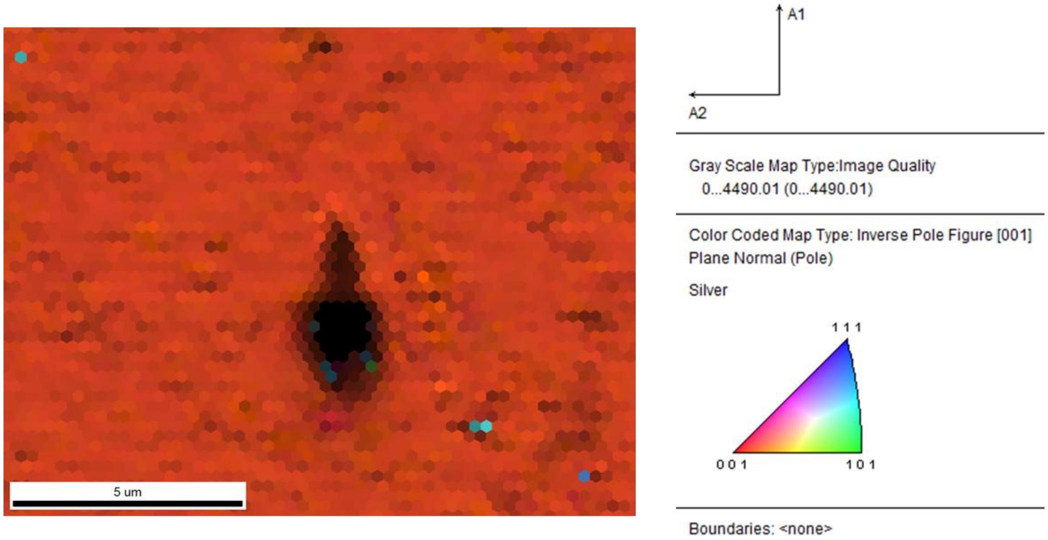

Figure 3.26 Single crystal Ag film EBSD mapping

3.2.2 Single crystal relaxation behavior

The viscoelastic relaxation behavior (steady state, no viscoplastic) of the Ag single crystal film is compared against the polycrystalline Ag films in Figure 3.27. The single crystal behavior (red curve) relaxes to a lesser extent than all the polycrystalline films (grey curves). The Ag single crystal film did not follow the hypothesis of Figure 3.22, in which the lack of boundaries would be expected to increase relaxation. Thus it is proven that there is no inherent correlation between grain boundary density and the extent of relaxation. However, the measurement of appreciable (non-zero) relaxation in the single crystal Ag strengthens the argument that the viscoelastic relaxation event is dominated by dislocation-based processes within the grains of each film and not at the grain boundary. Grain boundary sliding mechanisms suggested by others [51] are less likely to be contributing to the low-strain deformation behavior measured in this work. If grain boundary mechanisms did dominate the relaxation behavior the Ag single crystal relaxation extent would be expected to be closer to zero due to a lack of grain boundaries in the microstructure. Likewise, the twin density appears to play little or no role.

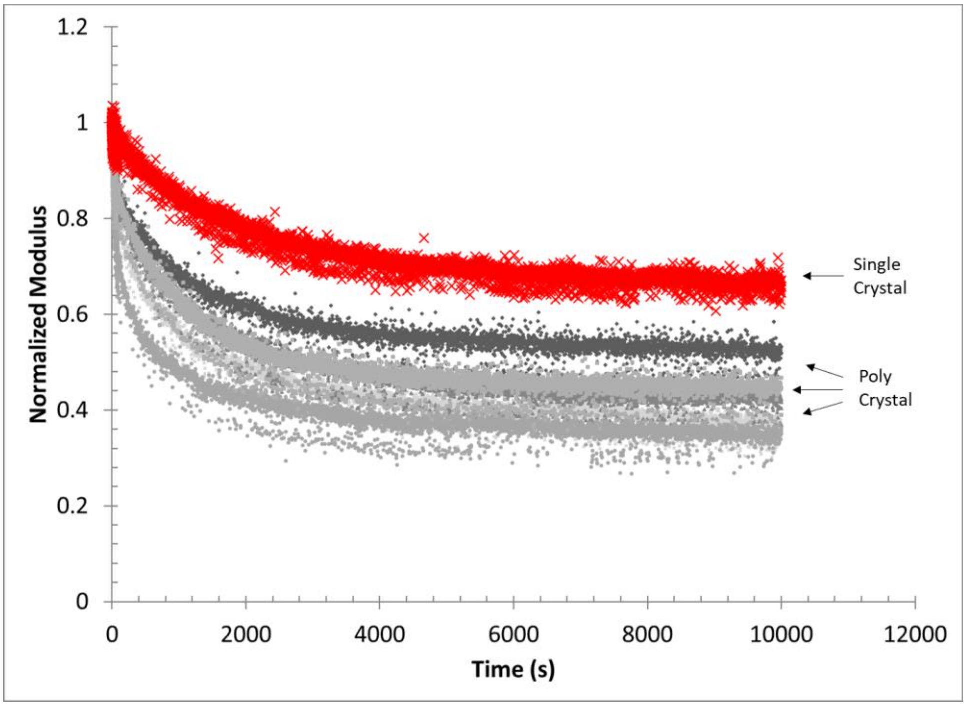

Figure 3.27 Viscoelastic relaxation behavior of Ag single crystal

The single crystal relaxation behavior was also fit to a four term Prony series, Figure 3.28. The red curve compares the single crystal Prony fit to the orange shaded polycrystalline curves. The Prony constants for the single crystal relaxation behavior: P_{10} = 0.02991, P_{100} = -0.0286, P_{1000} = 0.2287, and $P_{10,000}$ = 0.1799.

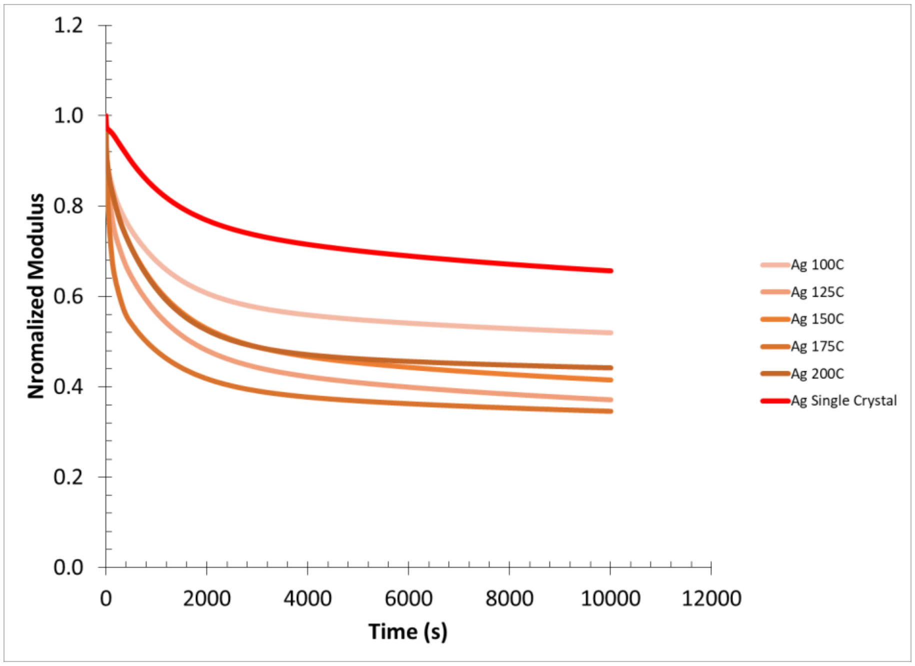

Figure 3.28 Prony series fitting of single crystal Ag relaxation

3.3 Thickness dependence with constant grain size

Up until this point the film thickness has been kept constant within a given metal film set while the in-plane grain size was modified with substrate temperature. This section of the chapter will explore the effect of thickness (z dimension) when the grain size (x-y dimension) is held roughly constant to determine if grain volume, rather than just diameter, is correlated with relaxation in those films that show an effect.

3.3.1 Characterization of Au films of varying thickness

Two Au films were sputtered at 400 °C for longer sputtering times than used for the 670 nm Au films of Figure 3.17c. The metal thickness measured at 1000 nm and 1412 nm with 200 nm of SiN_x substrate underneath each film. The thickness was measured using X-Ray Reflectometer methods and verified with cross-sectional imaging. SEM images of the plan view surface were taken using the Zeiss in-lens detector. These images are shown Figure 3.29.

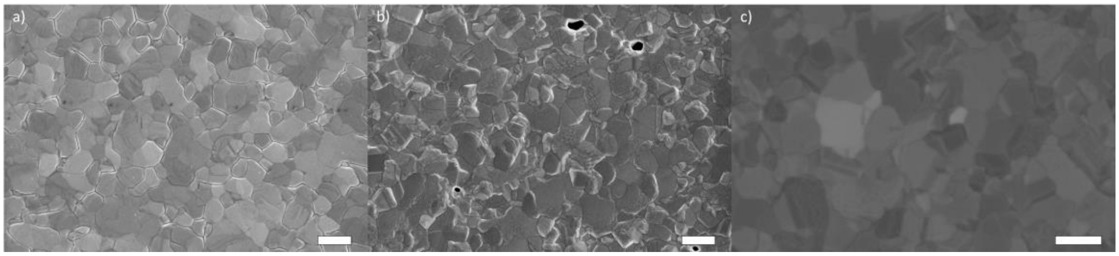

Figure 3.29 Plan view images of Au films of different thickness a) 670 nm b) 1000 nm c) 1412 nm. Scale bar 1 micron

To verify the columnar structure of the thicker films, FIB cross-sectional images were also taken and shown in Figure 3.30. These images show full columns of Au grains from SiN_x substrate to the metal surface. Similar densities of growth twins are visible in all three cases.

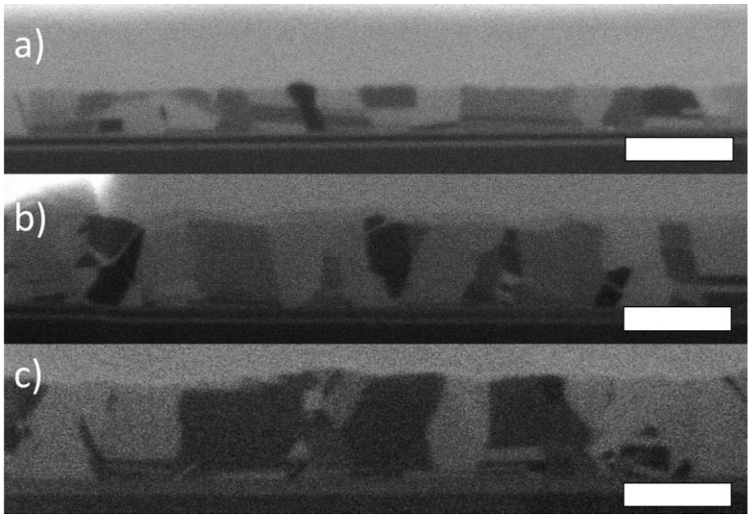

Figure 3.30 Cross-section FIB images of Au films of varying thickness a) 670 nm b) 1000 nm c) 1412 nm. Scale bars 1 micron

The grain size of the films was measured using the same methods described in Section 3.1.1.2. The grain size of the two thicker films in this study were comparable to the 670 nm thick 300 °C Au sample and not the 670 nm thick 400 °C sample. The properties of the three films are shown in Table 3.5. The average grain size for each Au film is within 10% of each other and each film has predominantly columnar microstructure, allowing for a suitable z-height thickness comparison in bulge relaxation studies.

Material	Thickness (nm)	Sputter Temperature (C)	Average Grain Size (nm)
Au	670	300	658.7
Au	1000	400	671.1
Au	1412	400	706.2

Table 3.5 Film properties of Au films of different thickness

3.3.2 Variable Au thickness relaxation behavior

Each thicker film was tested using the 80 °C bulge test like all tests previously. The viscoplastic relaxation was exhausted until only viscoelastic relaxation remained. The three viscoelastic curves for the 670 nm, 1000 nm, and 1412 nm films are shown in Figure 3.31. The Prony fits, Figure 3.32, highlights a slight difference in the 1000 nm film relaxation response that may be hidden in the noisier bulge data of Figure 3.31. However, the relative closeness of these curves indicates that film z-height or thickness has a marginal effect on relaxation behavior if the grain size is kept constant.

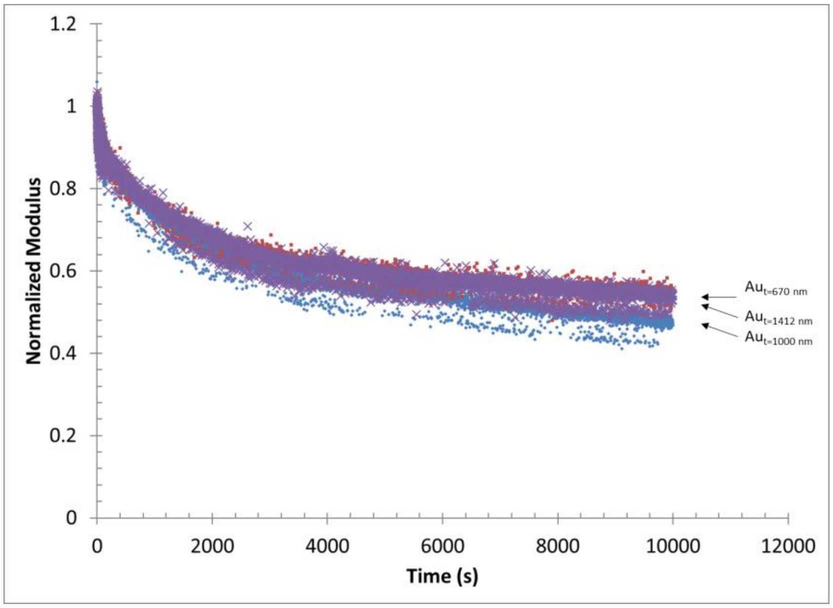

Figure 3.31 Viscoelastic relaxation curves for variable thickness Au films

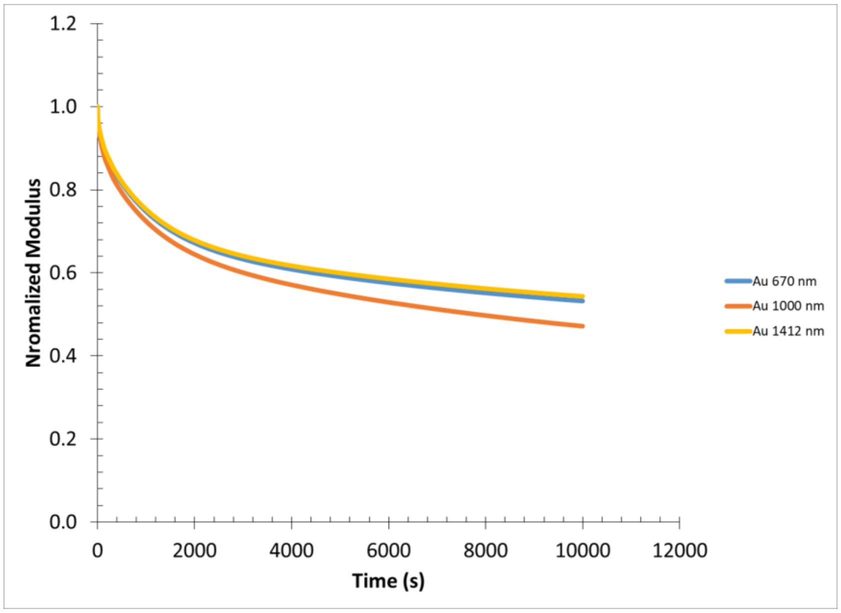

Figure 3.32 Prony fits for variable thickness Au films

The variable thickness relaxation response was incorporated into the constant thickness Au D^2 behavior of Figure 3.21. This is shown in the two red data points added to the Au linear grain size dependence in Figure 3.33. This indicates that the planar grain size contributes more to the relaxation behavior of an FCC film than the z-height or thickness of the film (or, equivalently, the duration of the deposition process). Since the data points track quite closely with the grain area (D^2) trends, the Au stress relaxation behavior appears to be independent of the thickness dimensions.

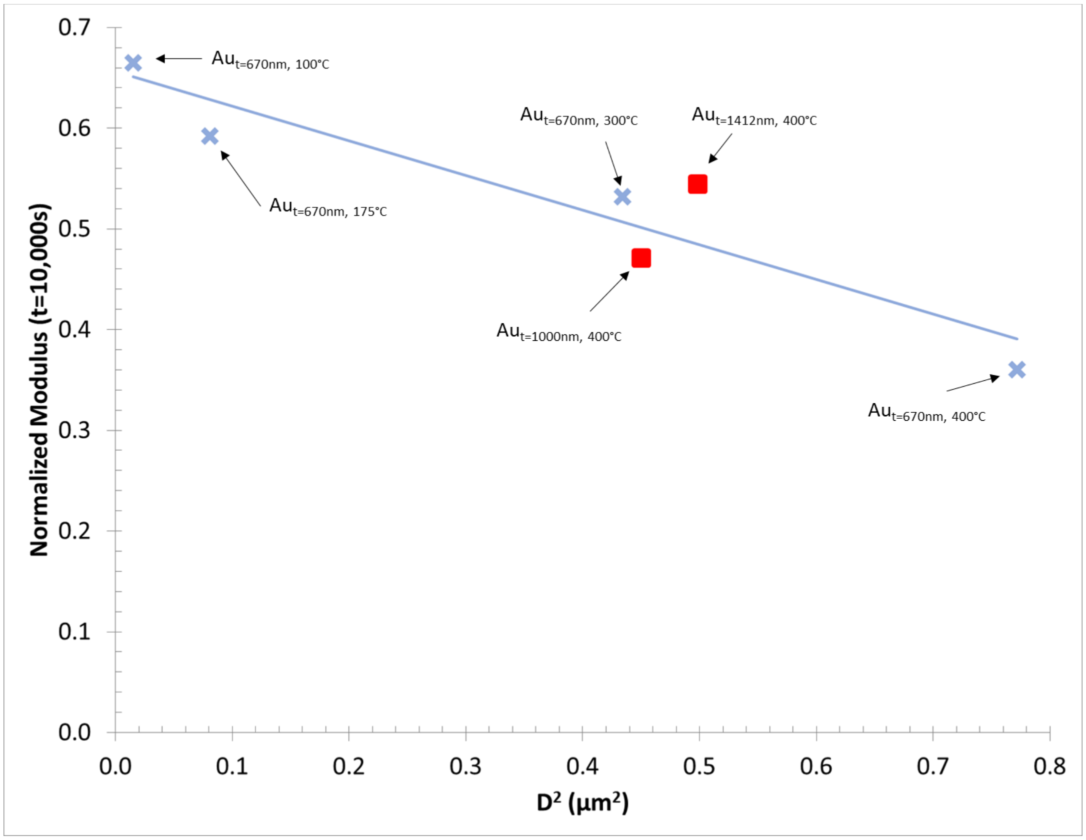

Figure 3.33 Incorporating variable thickness relaxation response with grain size dependence

3.4 Grain size effect and mechanism discussion

The effect of grain size on the low-strain, time-dependent deformation behavior of FCC thin films was explored in this chapter. It can be seen in Figure 3.21 that, in general, an increase in grain size (D) would result in increased viscoelastic relaxation response for Al(Mg), Au, and Pt films. The Ag and Cu films' viscoelastic relaxation was shown to be independent of grain size over the range of sizes explored here. The relationship between grain size and the deformation mechanism controlling the anelastic behavior will be explored in this section. Throughout, it is assumed that there could be a direct interaction between moving dislocations and the grain boundaries (or growth twins) in order to explore the ramifications of such a mechanism.

A 2014 microbeam bending study on Al-(1 wt%)Cu films with grain sizes ranging from 4 to 20 μm found no grain size dependence on low-strain, recoverable viscoelastic behavior [58]. In that study the thin film specimens were tested in both tension and bending. The anelastic behavior was attributed to diffusion-limited dislocation glide where the dislocation motions were impeded by interaction with the network of dislocations within each grain or by Cu solutes. It was claimed that upon removal of stress, backstresses within the mobile dislocations reverse the direction of the dislocation, driving the recovery of the deformed material. In another study, creep experiments on an Al-Mg alloy indicated a similar mechanism as found in the Al-Cu study, whereby the creep deformation and recovery was attributable to bowing and unbowing of mobile dislocations [88]. In that Al-Mg study, the authors suggest a two stage ‘unbowing’ process: a fast stage where the dislocation experiences minimal obstacles, and a slow stage where the dislocation must un-bow across higher energy obstacles such as precipitates. The authors of the Al-Mg study suggest a thermally activated unbowing of pinned dislocations is the driving force for recovery after creep deformation.

The relaxation trends found within this work suggest that a similar dislocation bowing and unbowing mechanism is driving the viscoelastic relaxation response. An increase in grain size could enable more widely-spaced grain boundary barriers to dislocation motions, thus increasing the possible relaxation extent. In Figure 3.34, three distinct anelastic deformation scenarios are presented based on this model: (a) a dislocation-free, ultra-fine crystal structure, (b) an intermediate grain size regime between ~50 nm and ~750 nm, and (c) large-grained films greater than 750 nm. Grain boundary sliding in nanocrystalline materials (i.e. < 50 nm, Figure 3.34a) has been attributed to low-temperature creep in electrodeposited Ni films [56]. We assume that grain boundary sliding will dominate in other nanocrystalline FCC materials as well. Thus the available evidence suggests that there is a grain size regime in which dislocations are less important than grain boundaries, and a much larger grain size regime in which there may be no size dependence.

The present work on stress relaxation suggests a special intermediate grain size regime, Figure 3.34b, where dislocations exist and are reasonably close to a grain boundary. In Figure 3.34c, the grains are sufficiently large where most of dislocation obstacles are other dislocations (or solutes/precipitates) and far from grain boundary interactions. This would be the scenario in previously mentioned Al-Cu microbeam tests, where the grains were larger than 4 μm.

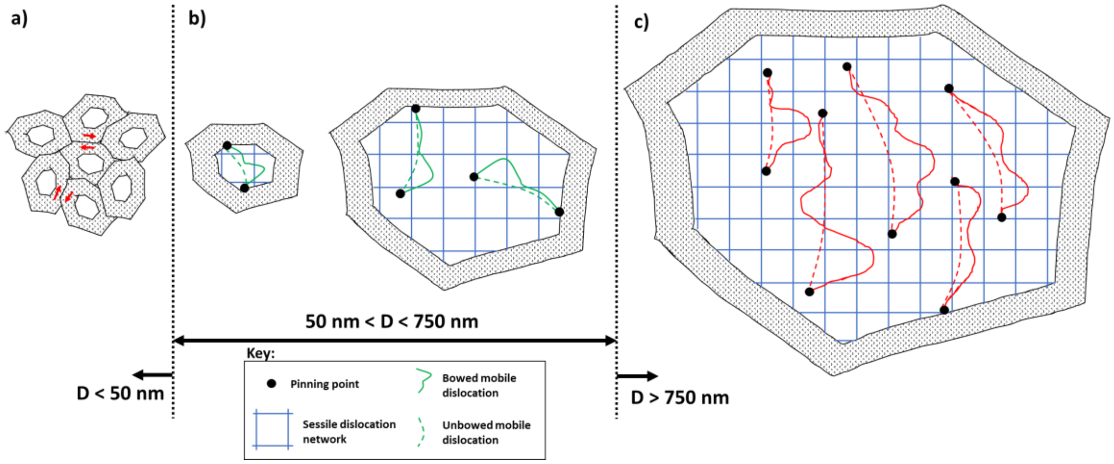

Figure 3.34 Schematic of anelastic deformation and recovery mechanisms a) grain boundary sliding b) dislocation bowing with grain size dependence c) dislocation bowing without grain size dependence

Dislocations in smaller grains within the intermediate grain size of Figure 3.34b may react strongly with the grain boundaries, and this interaction will weaken as the grain increases to the coarser end of this range. Decreased grain boundary-dislocation interactions with increasing grain size is one plausible explanation for the observed D^n relaxation trends. It suggests that the available grain matrix area available for bowing motion of dislocations during low stress, iso-strain relaxation events is higher as the grain size increases. In plastic deformation theory, Hirth suggests a hard and soft region of a grain for dislocation motions [89]. The soft region is the portion of the grain sufficiently far from the dislocation-interfering forces of a grain boundary while the hard region is close enough to the repulsive forces of the grain boundary. These forces are shown to have a $\frac{1}{R}$ dependence with R being the distance from the grain boundary (or also other dislocations/obstacles). Figure 3.35 shows a schematic of this interaction distance between the "soft" grain (D_{soft}) and the full grain size (D). The hatched portion represents the grain boundary interaction region in this figure and in Figure 3.34. In high stress plasticity studies, Shen et al. showed that dislocation spacings will tend to average around 40 nm and will pile up to closer spacings near the grain boundary [90]. Since our experiments are low stress, elastic bulge tests, pile up is not expected near the grain boundary, but an equilibrium spacing of 40 nm is a reasonable distance within the grain's soft matrix and for the grain boundary interaction area.

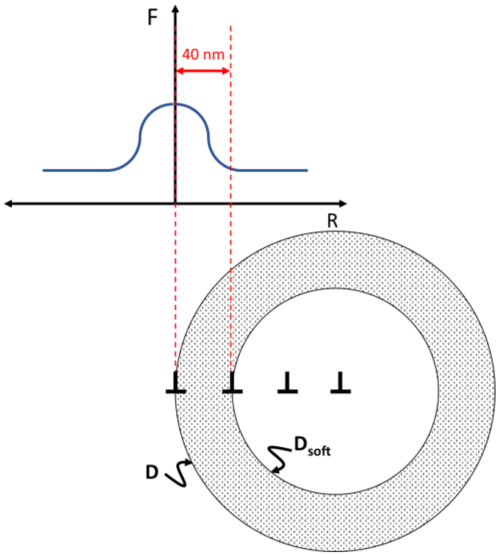

Figure 3.35 Dislocation interaction distance in circular grain (D)

If the grain boundary-dislocation separation distance is 40 nm in the films of this study, it further suggests increasing grain size will increase the available soft area for bowing dislocations. Within the 50 nm to 750 nm grain size regime of this study, the relative amount of soft grain area (D_{soft}) increases quite rapidly as grain size (D) increases, which translates to a larger area for dislocation bowing/unbowing. A grain size of 750 nm represents the point at which the ratio of $\frac{D_{soft}}{D}$ becomes larger than 90% for a 40 nm thick ring of grain boundary interaction, where a grain size of 50 nm has virtually zero soft grain available. According to this model, at grain sizes larger than 750 nm, the D^n trend is expected to discontinue and further relaxation is independent of increases in grain size. This could explain the lack of grain size dependence in large grained (D > 4μm) Al-Cu films described earlier [58].

Prior work in our group on Au films found a similar D^2 trend across three test temperatures (20, 50, and 80 °C), Figure 3.36 [8,91]. Region I of this picture falls within the special grain size regime depicted in Figure 3.34b. Region II follows the large grained film behavior of Figure 3.34c where the soft matrix of the grain becomes sufficiently large compared to the hard grain boundary area. Within Region II grain size dependent relaxation is expected to end.

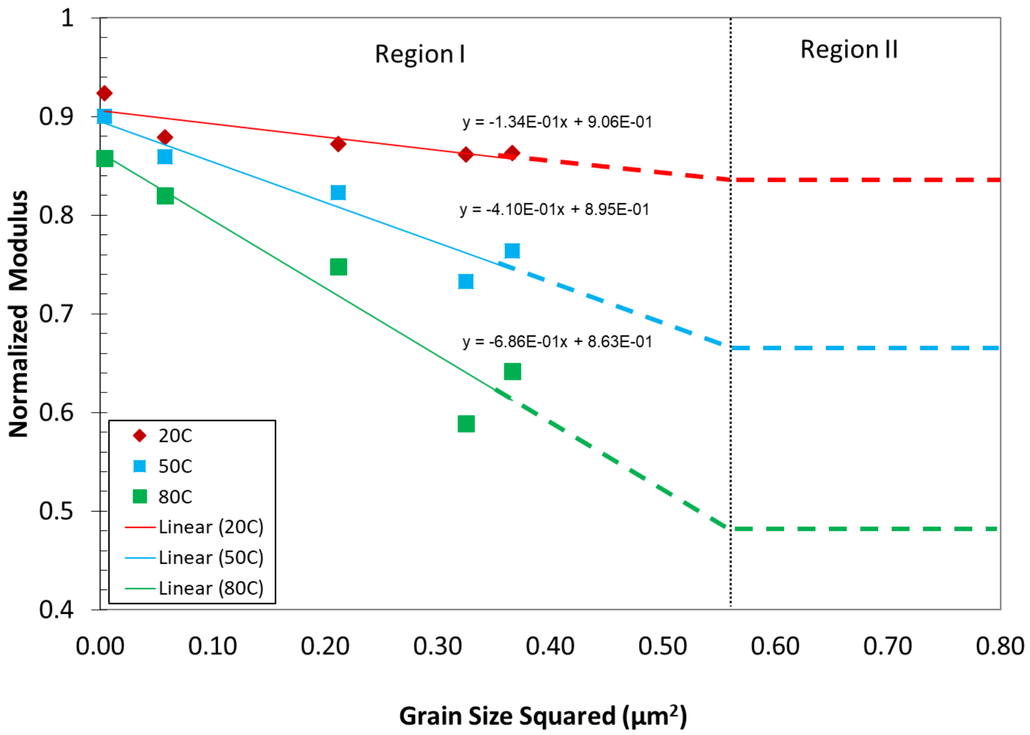

Figure 3.36 Au film relaxation behavior with D^2 dependence for three test temperatures

The Pt, Al(Mg), and Au films of this work exhibit relaxation behavior proportional to D^n while the Ag and Cu films do not. The lack of D^n relaxation response in Ag and Cu is considered next. The first plausible explanation for the lack of grain size dependence in Ag and Cu comes from the relatively small range of grain sizes that could be grown with the sputtering process. The bulge test method requires a smooth surface finish for proper electrode operation, and the Ag and Cu films could not be deposited smoothly above average grain sizes of 334 nm and 412 nm, respectively. Ag, Au, and Cu metals each have low to mid-range values of stacking fault energies, which increase the film susceptibility to growth twins, as the TEM images show in Figure 3.11. If it were possible to sputter larger-grained Ag and Cu films, like the range possible with Au, it may follow that the gradual D^n behavior measured in Au films is also present in Ag and Cu films, as Figure 3.37. In this figure the dashed trend lines would match the Au behavior if the hypothetical large-grained Ag and Cu films (dashed red circles) could be fabricated with a smooth surface finish. This explanation is somewhat weakened by the strong D^n trends observed for Al(Mg) and Pt, both of which also had a fairly restricted grain size range.

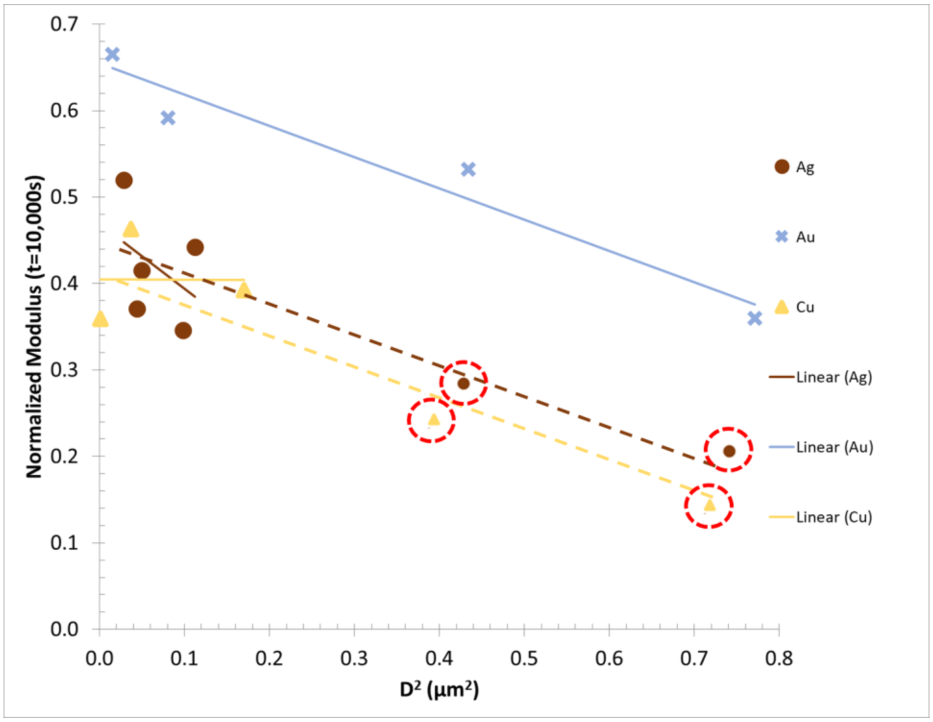

Figure 3.37 Hypothetical relaxation response of larger grained Ag and Cu films

A second, more likely, explanation for the low and negligible D^n dependence of the Ag and Cu films may be that the effective "soft" matrix available for dislocation bowing is reduced not just by the grain boundary, but also by the presence of twins. Growth twins are more likely in low SFE materials, especially Ag which has the lowest SFE of the FCC metals tested. In Figure 3.38a, the soft grain area increases from A_0 to A_1 as the grain size increases. In a low SFE, highly-twinned film, Figure 3.38b, the effective soft grain area remains a constant $A_{0,t}$ even as the grain size increases. The available dislocation bowing area in a twinned material is effectively reduced as twins act as an additional energetic barrier to further relaxation. The relaxation of highly twinned materials appears to be independent of true grain size and more dependent on twin density. The weakness in this explanation is the strong D^n trend in Au which has a similar stacking fault energy as Cu, and also exhibited many growth twins.

The shortcomings of the "hard" grain boundary region model suggest that a different dislocation interaction could be responsible for the D^n behavior in Al(Mg), Au, and Pt, and that the boundaries themselves are not the key. Instead, the elevated temperature depositions may have altered some other aspect of the microstructure so that grain size is only a proxy for the real determining factor. This possibility will be discussed in the following chapters.

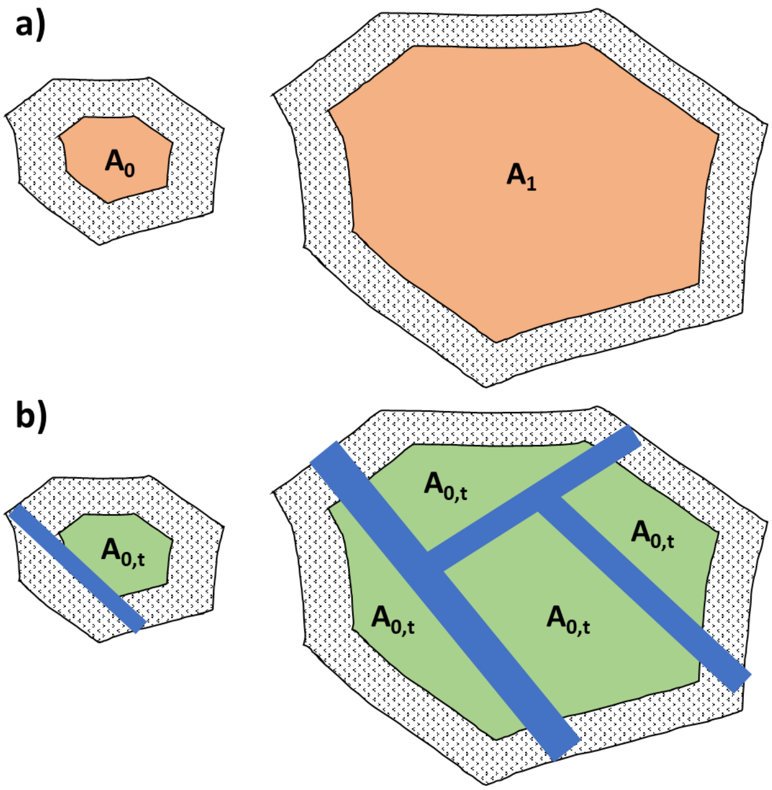

Figure 3.38 Plan view schematic of available "soft" grain in a) high SFE and b) low SFE material

3.5 Summary of grain size dependence

Five sub-micron FCC metal films were fabricated by DC magnetron sputtering. The planar grain size of each film, D, was altered by heating the substrate during deposition using a heat lamp. The bulge test technique was used to measure the viscoelastic response of each film during low stress, iso-strain experiments. It was shown that some FCC metal films will relax more with increased grain size as measured by the normalized modulus after 10,000 seconds at 0.1% strains. The relaxation extent was linearly proportional to D^n where n values range between ½ and 2. The low temperature, low stress environments of the bulge test suggest that dislocation bowing and unbowing are plausible mechanisms for the relaxation and recovery events, respectively. One model for this behavior suggests that a unique planar grain regime of 50 nm to 750 nm exists where the relaxation behavior will follow the D^n grain size dependence. If so, the increase in soft grain areas with increasing grain size D, will decrease the barriers to dislocation bowing mechanisms, which increases the relaxation extent. However, not all of the evidence supports this model so other possibilities must also be considered.

4. Dislocation density effect on relaxation

The metal films used in this study are highly pure (Ag, Au, Cu, and Pt) except for the Al(Mg) film which contained <1% Mg solutes to mitigate grain growth. An increased relaxation response with grain size behavior ($NM \propto D^n$) was determined in Chapter 3. Since no alloying elements such as solutes or precipitates were systematically added to harden the films against relaxation, only two logical strengthening mechanisms are accessible in this study: the presence of 1) grain boundaries or 2) dislocation-dislocation interactions. This chapter will explore the contributions of dislocation density and arrangement and determine if grain size (grain boundaries) are directly responsible for an independent mechanism controlling relaxation response or if they are associated with a microstructural change during film growth that is actually responsible for the grain size dependence.

4.1 Dislocation density measurement results

4.1.1 XRD measurements using CMWP method

The Convoluted Multiple Whole Profile (CMWP) X-ray line broadening technique was used to measure dislocation density of all films used in this study. An example of the individual fitting functions for each Au film are shown in Figure 4.1 with a compilation plot in Figure 4.2. For the Ag, Al(Mg), Cu, and Pt films, the individual fittings are not shown, only the compilation plots in Figure 4.3, Figure 4.4, Figure 4.5, and Figure 4.6 respectively. Since the films were considerably textured only highly reflecting planes such as (111) and/or (200) were used for CMWP fitting purposes.

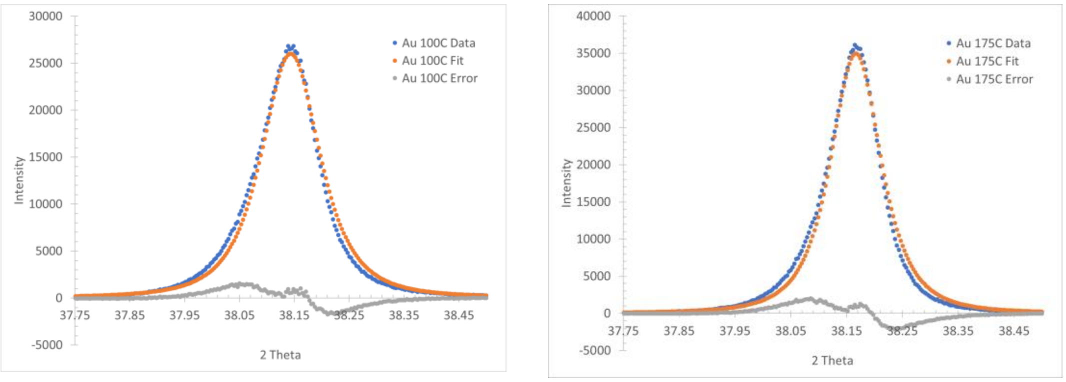
a) Au 100 °C

b) Au 175 °C

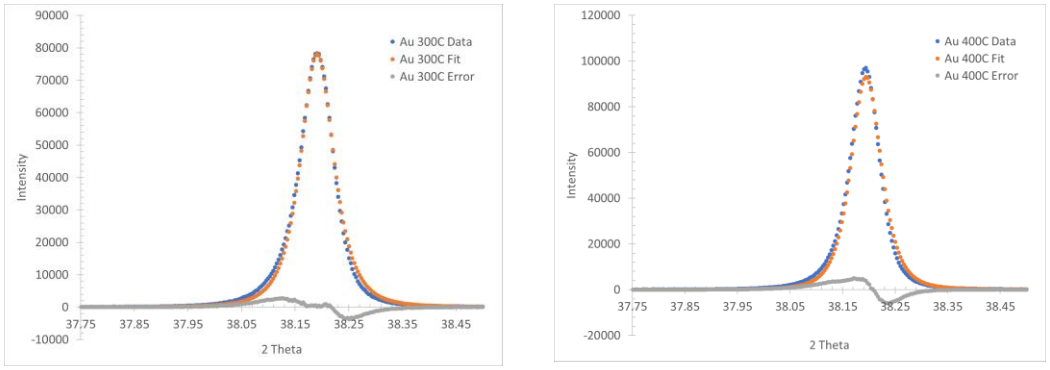
c) Au 300 °C

d) Au 400 °C

Figure 4.1 Individual CMWP fittings for each Au film

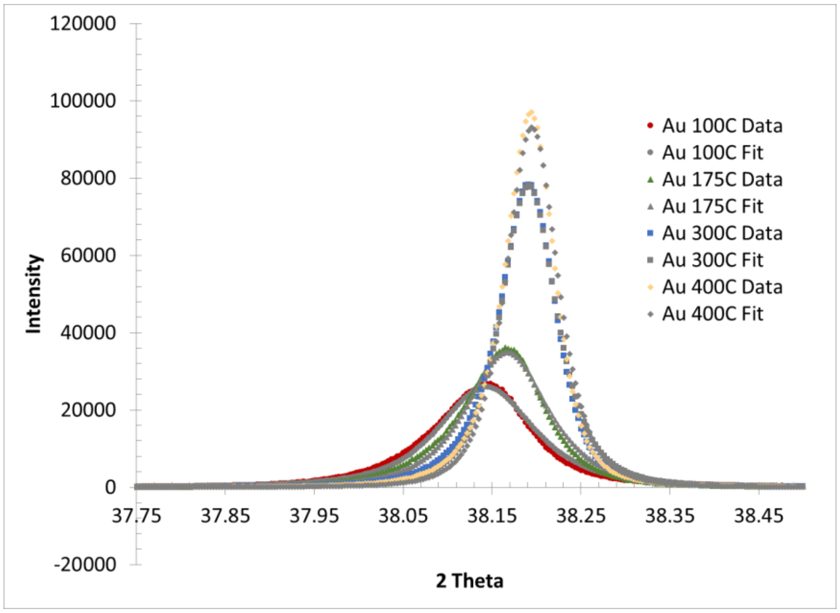

Figure 4.2 CMWP fit comparison for all Au films

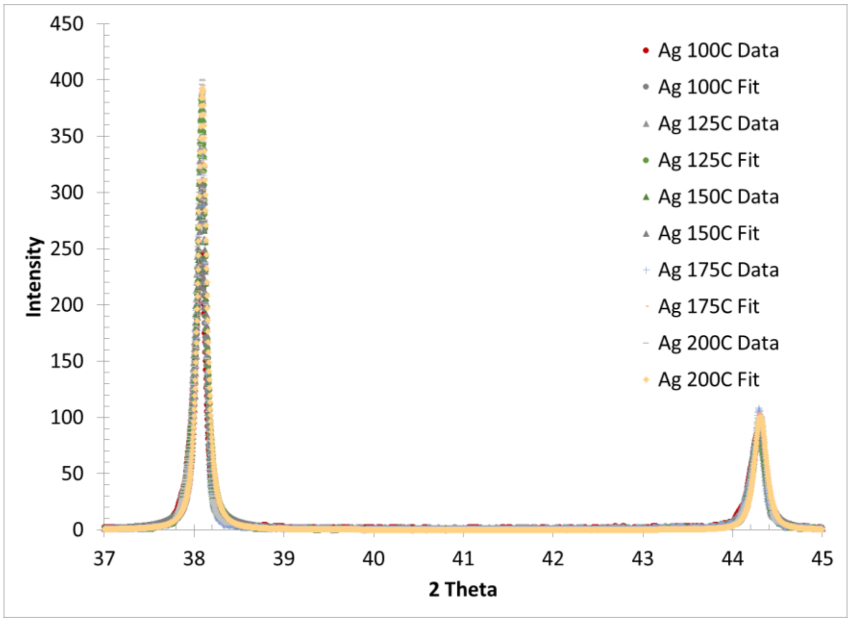

Figure 4.3 CMWP fit comparison for all Ag films

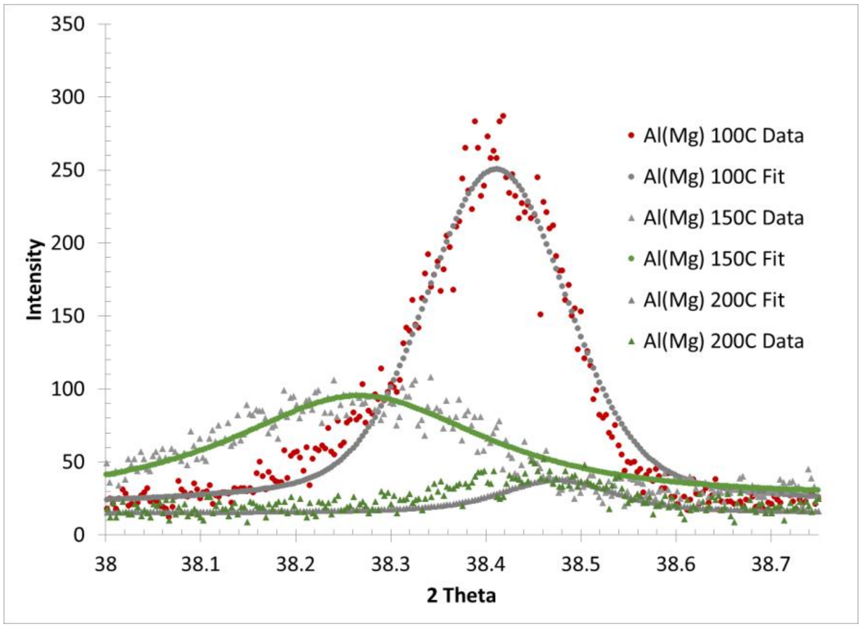

Figure 4.4 CMWP fit comparison for all Al(Mg) films

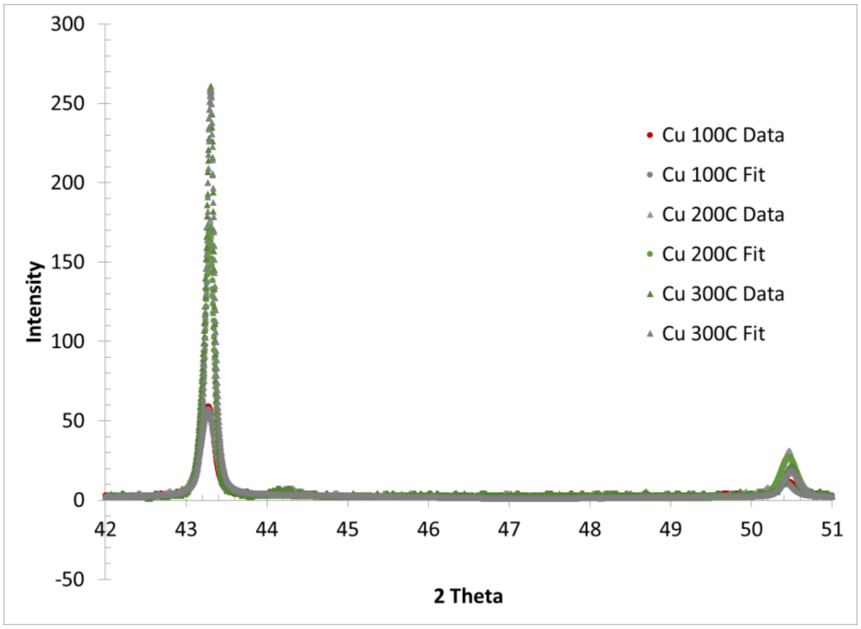

Figure 4.5 CMWP fit comparison for all Cu films

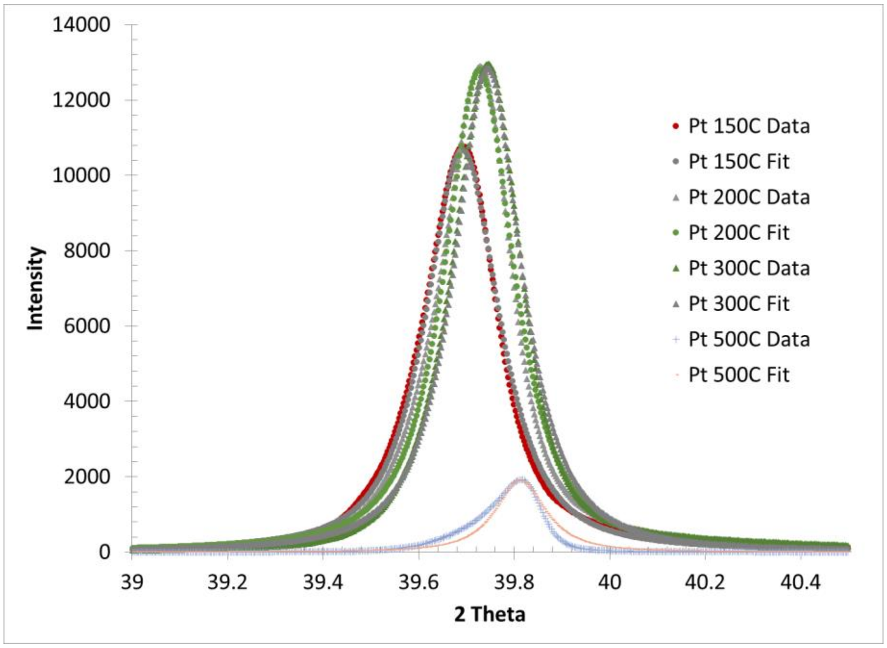

Figure 4.6 CMWP fit comparison for all Pt films

The dislocation density (ρ) was extracted from each CWMP fitting curve and is tabulated in column six of Table 4.1. The CMWP XRD analysis shows the dislocation density decreasing with increasing sputter temperature (and proportionally grain size) in the Au and Al(Mg) film only. The Ag, Cu, and Pt films show dislocation density to be independent of grain size. This is depicted graphically as a plot of the CMWP dislocation density against grain size D in Figure 4.7. In-situ TEM studies have shown dislocations form during cooling in sputtered films [92,93] as a means of stress relief; these same studies have reported similar dislocation density magnitudes as those measured in this work. Other researchers have also determined dislocation densities around 10^{15} m^{-2} in electrodeposited nanocrystalline Ni films [94] and sputter-coated Pt thin films [95]. In each reference the films were (111)-textured like the films in this study.

Material	Thickness (nm)	Sputter Temperature (C)	Average Grain Size, D (nm)	$\frac{-\Delta G}{G} = (1 - NM_{t=10,000s})$	ρ (X 10^{14} m^{-2}) CMWP (TEM)	L (nm)
Ag	500	100	168.05	0.480	13.5	46.0
		125	210.01	0.629	11.9	56.0
		150	223.38	0.585	11.0	56.2
		175	312.8	0.654	12.0	57.1
		200	334.5	0.558	12.0	52.7
Al(Mg)	500	100	111.8	0.333	12.1 (2.6)	40.5
		150	278.4	0.439	12.1	46.5
		200	371.8	0.445	7.2 (0.9)	60.5
Au	670	100	122.9	0.335	11.8 (5.0)	41.1
		175	284.0	0.408	11.9	45.2
		300	658.7	0.468	6.0	67.9
		400	878.4	0.640	4.1 (5.2)	96.7
Cu	500	100	31.9	0.641	15.1	50.3
		200	191.4	0.537	15.1	46.0
		300	412.5	0.608	15.1	49.0
Pt	500	150	44.8	0.174	12.8	28.4
		200	60.4	0.247	12.9	33.8
		300	151.5	0.285	12.8	36.4
		500	264.1	0.375	12.9	41.7

Table 4.1 Dislocation density measurements compilation

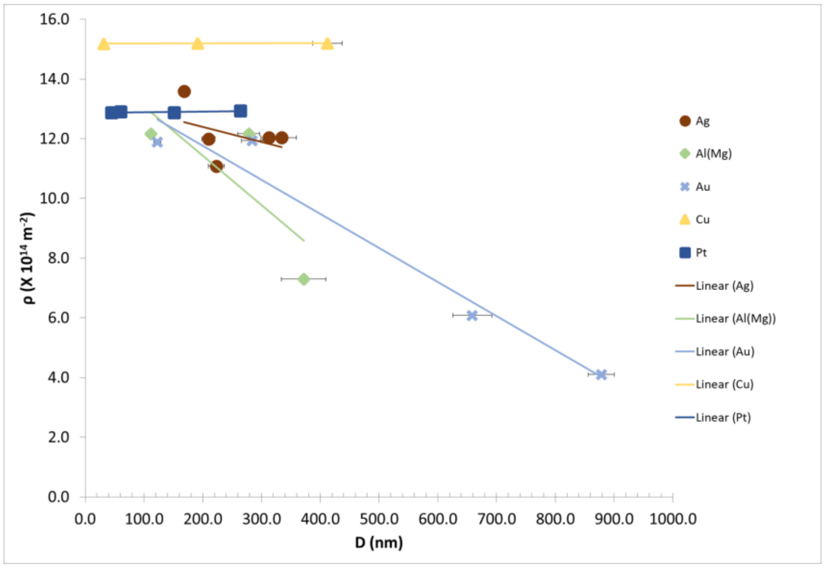

Figure 4.7 CMWP dislocation density measurements with grain size D

4.1.2 TEM measurements using Ham's method

Plan view TEM samples of the coarsest and finest Au and Al(Mg) films were prepared for dislocation density measurements using a TEM direct inspection method (Ham's method [80]). The foils were prepared using the technique described in Chapter 2. Using an SEM in-lens detector, the thickness of the Au foils after FIB milling was found to be roughly 50 nm and the Al(Mg) foils were roughly 150 nm in thickness, both sufficiently thin for 200 kV TEM electron transmission.

The Au and Al(Mg) plan view images are shown in Figure 4.8 and Figure 4.9 respectively. Ham's direct inspection dislocation density measurement method requires a grid or mesh overlay on each micrograph. The mesh (m) is shown as a grid of faint greyish-white lines in each figure. Each foil was tilted in the TEM to create diffraction conditions to allow dislocation contrast. Using ImageJ the dislocation intersections with this grid are counted and the length of the mesh within the grain of interest is measured.

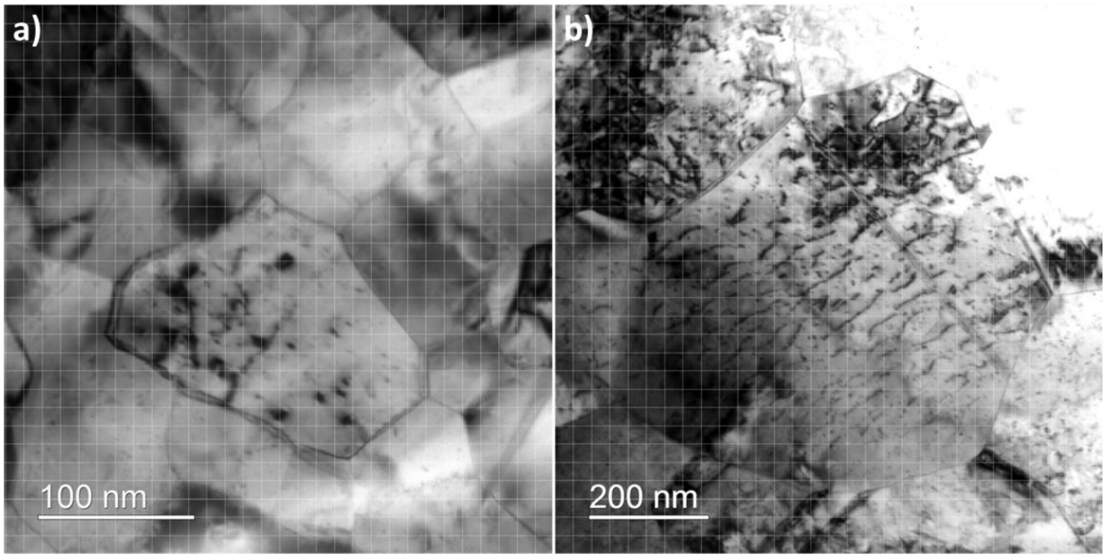

Figure 4.8 Au foil images following Ham’s method dislocation density analysis a) 100 °C b) 400 °C

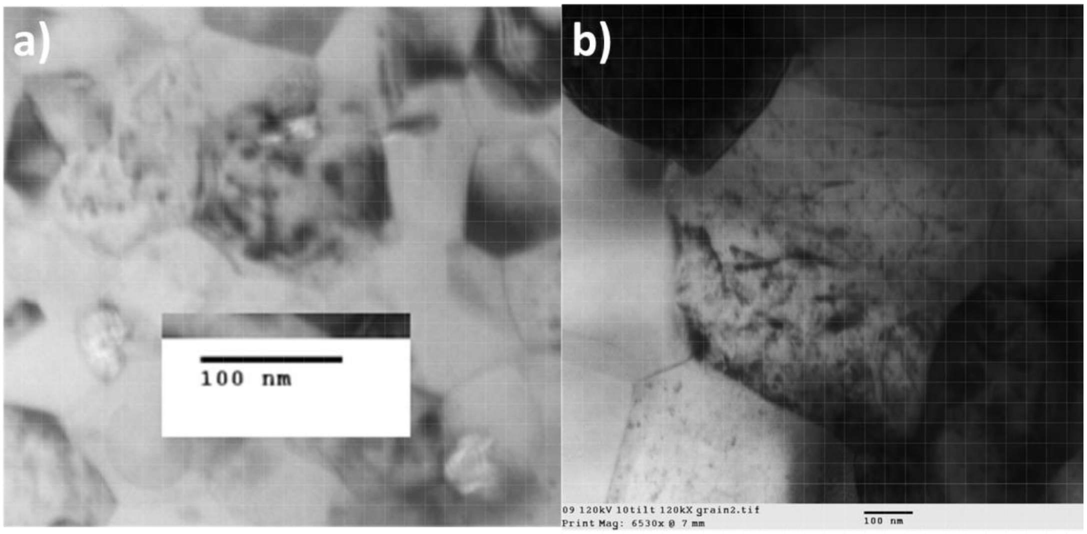

Figure 4.9 Al(Mg) foil images following Ham’s method dislocation density analysis a) 100 °C b) 200 °C

The analysis of these images is summarized in Table 4.2. Equation 2.4 was used to calculate the dislocation densities after measuring the mesh length, counting the number of dislocation intersections, and measuring the foil thickness. The densities calculated from TEM analysis are also added in parentheses in column six of Table 4.1 to compare against the CMWP method. The TEM analysis shows that the dislocation density is comparable in magnitude to the CWMP analysis (~ 10^{14} m^{-2}) but does not display the same trend of decreasing density with increased grain size. Dislocations invisible in the given imaging conditions or lack of resolution in the fine-grained sample may have contributed to sources of error in the direct inspection methodology.

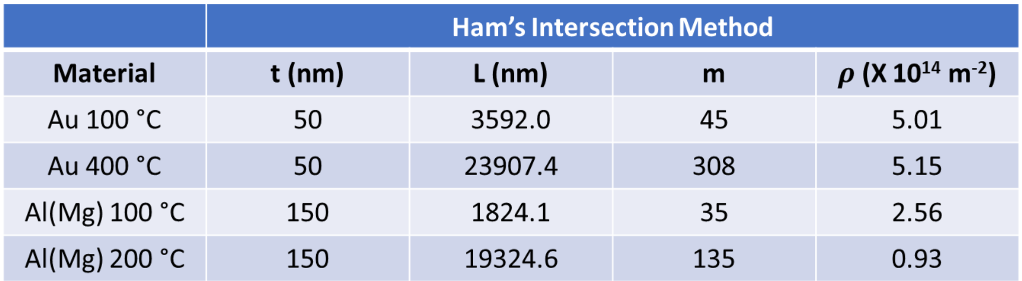

	Ham's Intersection Method			
Material	**t (nm)**	**L (nm)**	**m**	**ρ (X 10^{14} m^{-2})**
Au 100 °C	50	3592.0	45	5.01
Au 400 °C	50	23907.4	308	5.15
Al(Mg) 100 °C	150	1824.1	35	2.56
Al(Mg) 200 °C	150	19324.6	135	0.93

Table 4.2 Ham intersection method results

4.2 Dislocation density discussion

Inspection of measured dislocation density trends for this present work indicates that the stress relaxation behavior of FCC metal films is independent of the of the dislocation density. In Figure 4.7, the Au and Al(Mg) films exhibit decreasing dislocation densities with increasing grain size, suggesting that a viscoelastic relaxation is also proportional to dislocation density. However, the Pt film shows a constant measurement of dislocation density with grain size, yet this film did exhibit relaxation behavior that followed D^n behavior. Since the Al(Mg), Au, and Pt films all showed D^n relaxation dependencies (Chapter 3), yet the trends in dislocation density with grain size are inconsistent, a different mechanism must be at play. The most likely factor driving relaxation behavior is not dislocation density itself, but an important characteristic of the dislocation density, the average pinning distance between dislocations, L. The dislocation density is related to pinning distance by $\rho = N_v L$ where N_v is the number of dislocations per unit volume.

Friedel proposed that a reduction in modulus due to bowing of dislocations pinned into a network arrangement is directly proportional to the density and arrangement of the pinned dislocations as in equation 1.19. The stress relaxation response measured in this work is related to the Friedel modulus decay in the following way:

$$\frac{\Delta G}{G} = (1 - NM_{t=10{,}000s}) = \frac{1}{6}\rho L^2 \qquad \textbf{(4.1)}$$

Although this is written in terms of the shear modulus, G, the fractional change in Young's modulus should be the same. It is seen that the relaxation response for a given stress is related linearly to the dislocation density and to the square of the pinned dislocation distance L.

Direct and accurate measurement of L would be very difficult, but a sanity check on the magnitude of L can be performed using the Freidel model and previously measured characteristics of the films. Using the relaxation metric measured through bulge testing ($NM_{t=10,000s}$) and the measured dislocation density, an average L spacing was calculated for each metal film assuming that the Freidel model applies. The results are tabulated in column seven of Table 4.1 and plotted in Figure 4.10. The calculated L spacings are shown to increase with grain size for those films that demonstrated grain size dependent relaxation (Al(Mg), Au, and Pt films) and remained approximately constant for the Ag and Cu films.

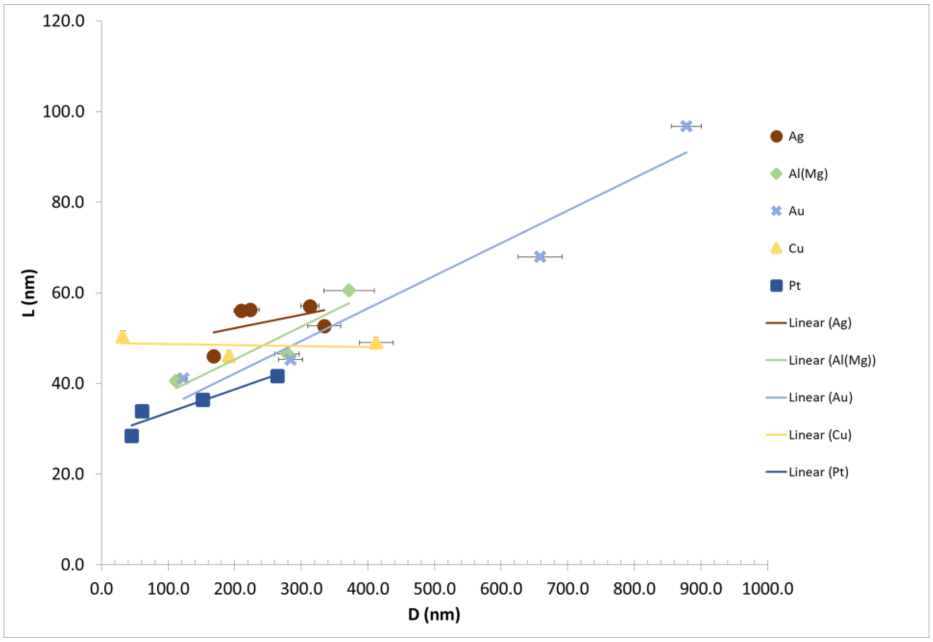

Figure 4.10 Calculated dislocation pinning distance L with grain size D

Bowing and unbowing of pinned dislocations is the proposed mechanism controlling viscoelastic relaxation and recovery in FCC metal films. The work to this point has shown the relationships between grain size D, dislocation density ρ, and pinned dislocation distance L. Considering all three variables (D, ρ, L), there exists four reasonable explanations for the observed D^n relaxation dependence in this work:

i. Dislocations near grain boundaries have reduced mobility, thus reducing grain size should reduce relaxation extent.

ii. Dislocation density changes as grain size changes, changing the dislocation-dislocation interaction probabilities.

iii. Inhomogeneous grain-to-grain distribution of dislocations in finer-grained films reduce relaxation by reducing pinning distance L.

iv. Dislocation arrangement and order increases with increasing grain size, effectively increasing pinning distance L.

Figure 4.11 shows schematics of the four mechanisms listed above. A fine and coarse-grained scenario are shown in the left and right side of each quadrant, respectively.

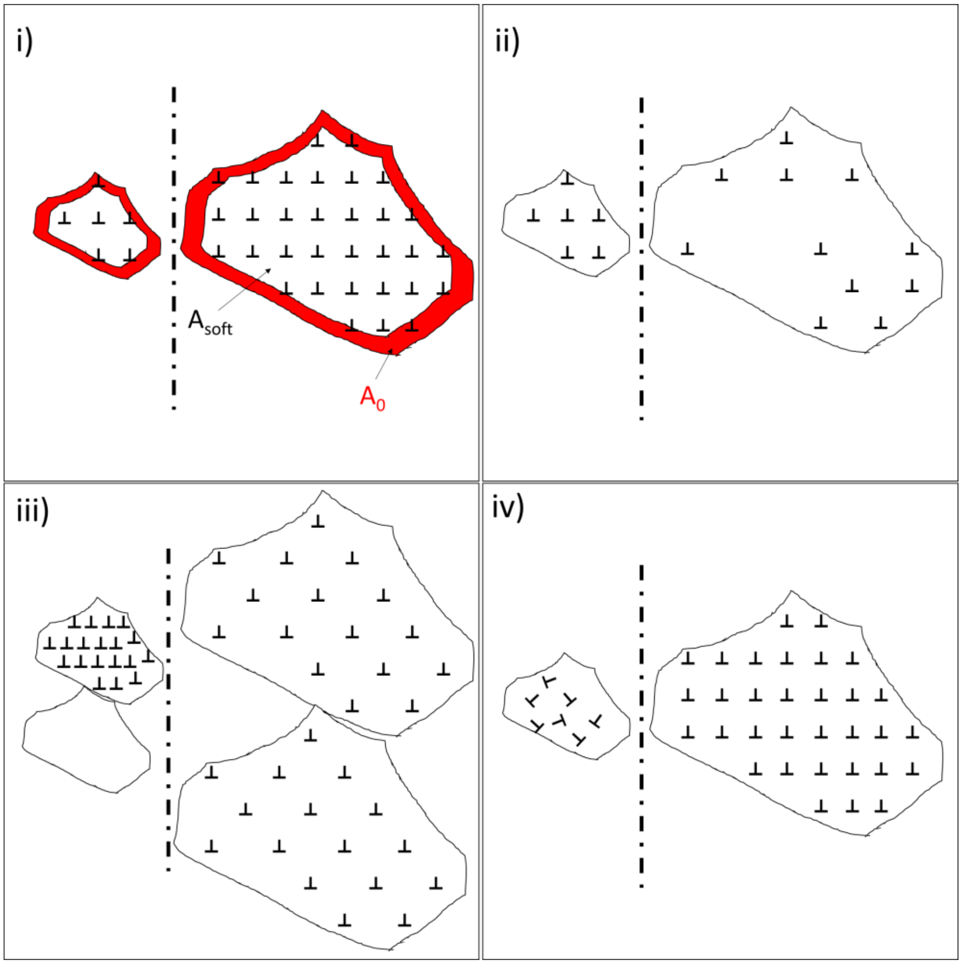

Figure 4.11 Schematics of plausible dislocation mechanisms driving D^n relaxation behavior

The first mechanism (Figure 4.11(i)) would be like the Hall-Petch strengthening mechanism where relaxation resistance is directly proportional to the grain size. Dislocations near the grain boundary should bow less than those in the "soft" grain interior, thus a decreasing grain size would result in decreased relaxation for a given dislocation density. However, it can be shown geometrically that the relative fraction of soft area to full grain area ($\frac{A_{soft}}{A_0}$) is dependent on the grain size to the -½ or $D^{-1/2}$. The viscoelastic relaxation response measured in this work was linearly proportional to D^n with n ranging from ½ to 2, thus it is unlikely a grain boundary hardening mechanism is controlling the relaxation response.

Figure 4.11(ii) depicts the scenario where a larger-grained film would have a higher dispersion of dislocations or lower dislocation density. This would imply dislocations in larger-grained films would have a larger separation distance L, thus allowing for larger relaxations. The results of the CMWP dislocation density analysis show that in some cases an increasing grain size correlates with a decreased dislocation density such as in the Al(Mg) and Au films. However, the Pt film shows no grain size dependence on dislocation density and because this film does show grain size dependence on relaxation, it rules out mechanism (ii).

The variables of grain size (D), and dislocation density (ρ) are shown to have weak to minor direct effects on the relaxation response. The third variable, pinned dislocation segment distance L, is approached in argument (iii) and (iv). In Figure 4.11(iii) a reasonable situation exists where fine grains (e.g. D ~ 50 to 100 nm) would generate an inhomogeneous distribution of dislocations during the film growth and cooling process, whereas a larger-grained film would have a more homogenized distribution. Consider the case where one grain in the finer-grained film has double the dislocations while a neighboring grain may have zero dislocations. On the average it would have the same dislocation density as the coarser grain as measured through XRD techniques, but the local distribution is heavily weighted. The result of this scenario would be a fine-grained film with a very low L distance separation, either very small in the double-dislocation density grain or zero in the dislocation-free grain.

A coarser-grained film with homogenous distribution would have a relatively larger L spacing, thus allowing greater relaxation as grain size increases.

The last scenario, Figure 4.11(iv) depicts a situation where the larger grain allows more uniform arrangement of dislocations formed during cooling while a finer-grained film generates a more chaotic arrangement. Although dislocation densities can be similar the separation spacing L between dislocations can be shortened in the more chaotic dislocation distribution of a fine-grained film. An example TEM image is shown in Figure 4.12 depicting the dislocation arrangement of the as-cooled state of a several hundred nanometer grain in a thin copper film [93]. This image suggests a non-uniform distribution of dislocations during the stress relief process would be exaggerated if the grain was smaller.

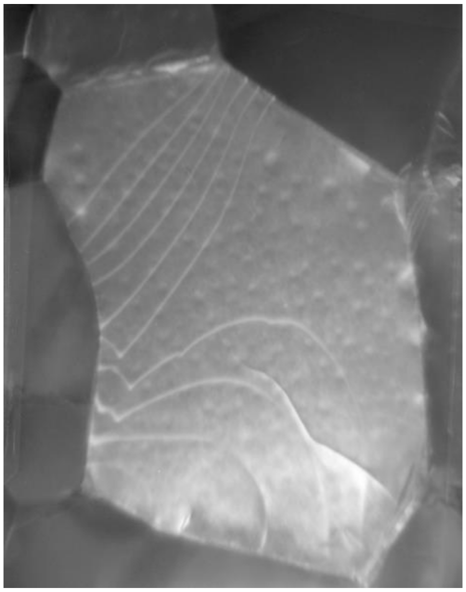

Figure 4.12 Inhomogeneous distribution of dislocations during thin film cooling from [93]

Mechanisms (iii) and (iv) are the most likely scenarios that explain the D^n relaxation response measured in this work. The pinned dislocation distance L is shown to increase with grain size D, thus increasing relaxation extent. Plan view TEM images of fine-grained Au films in this study depict a more chaotic dislocation structure and a more uniform distribution in coarser-grained Au films, Figure 4.13c and d. In this figure an arbitrary L spacing is drawn in the fine and coarse grains, L_f and L_c, respectively. In Figure 4.13d a hypothetical bowing of a dislocation is shown in the defect free region of the grain.

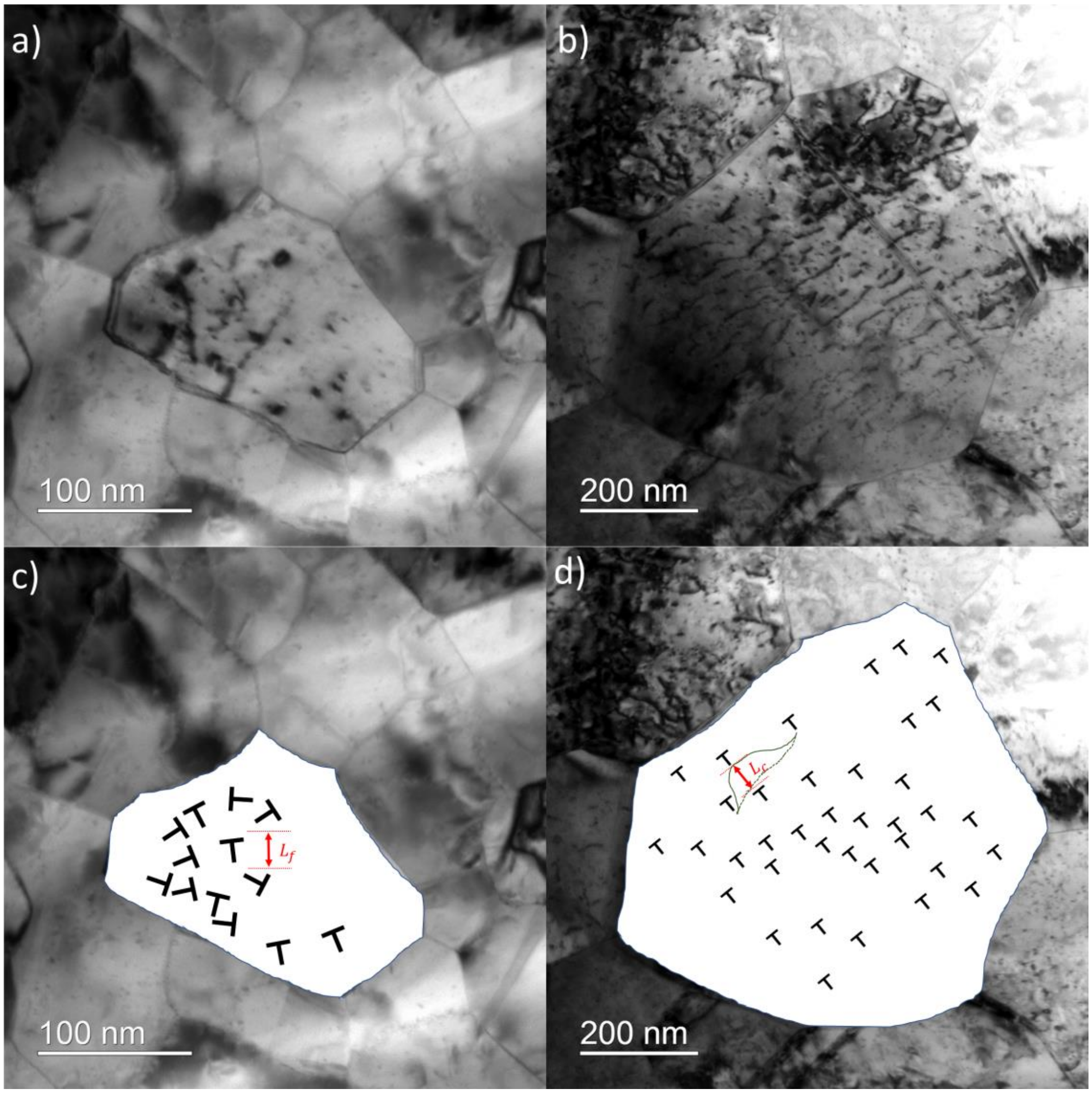

Figure 4.13 Dislocation spacing analysis for a) fine and b) coarse TEM plan view images with respective schematic dislocation arrangement in c) and d)

4.3 Summary of dislocation density dependence

The dislocation density analysis of the FCC metal films indicated dislocation density itself is not a strong contributor to relaxation. However, it was shown that the pinned dislocation spacing distance L could be an important driver for relaxation response. This variable can be independent of dislocation density through inhomogeneous grain-to-grain distribution of dislocations or by irregular arrangement of dislocations within a grain. These microstructural features of the grains are believed to control the D^n relaxation behavior since it was shown that the L values calculated using the Friedel model are reasonable for the films studied here. The models shows that relaxation increased when the dislocation spacing L also increased.

5. A mechanism for anelasticity in FCC metal films

One of the purposes of this study is to investigate the mechanism underlying the anelastic (a.k.a., viscoelastic) deformation of metallic thin films, especially regarding the grain size and dislocation arrangement. In low temperature experiments both grain boundary sliding and dislocation glide have been the prescribed mechanisms for the anelastic behavior. Much of the grain boundary studies involved very fine grain structures (typically D < 50 nm) and the mechanisms to describe these materials are generally not suitable for the larger grained films of this study (50 nm < D < 1000 nm). The anelastic behavior observed via stress relaxation tests in this work is proposed to be rate limited by dislocation-obstacle interactions, where the Peierls barrier is the primary obstacle. Thermally-activated, low-strain dislocation glide and overcoming obstacles will be discussed in terms of the iso-strain bulge tests performed in this work.

5.1 Thermally-activated dislocation glide

A dislocation moving within a grain due to an external applied stress can encounter a combination of strong obstacles (see Chapter 1) and a weaker lattice obstacle known as the Peierls stress [26]. The Peierls stress is the energy required to move a dislocation across a lattice in the absence of any thermal energy. A schematic of these two barriers is shown in Figure 5.1. In this figure the bulge test generates a sub-yield hoop stress that drives a dislocation trapped by hard pinning points A and B to the large discrete obstacle, which would typically be another dislocation in single element thin films. At a test temperature of 80 °C, there might be insufficient thermal energy to overcome this large obstacle by climb and the dislocation bowing stops. Upon removal of the hoop stress the line tension returns the pinned dislocation(s) to the unbowed state and the macroscopic stress state of the film recovers anelastically. In Figure 5.1a, the applied hoop stress is shown to be larger than the lattice friction or Peierls force meaning a dislocation can more easily move across defect-free regions of the slip plane while it is effectively blocked by the obstacle. Increasing the thermal energy of the system during testing may allow dislocations to overcome larger obstacles by lowering the work (ΔW) required to surpass them. Mongkolsuttirat et al. observed increasing relaxation by increasing the environmental test temperature from 20 °C to 80 °C in Au thin films bulge tests [91].

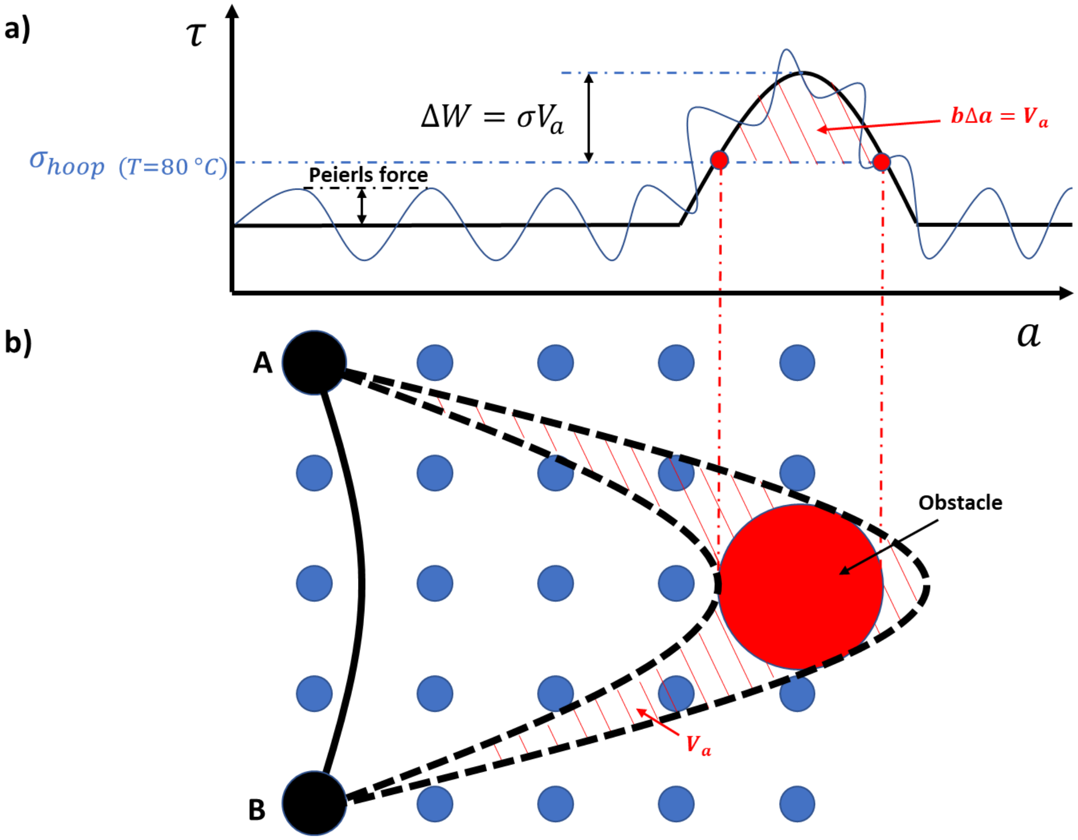

Figure 5.1 Schematic of thermally-assisted dislocation glide with a) stress energy landscape for a moving dislocation and b) pinned dislocation at points A and B overcoming discrete obstacle after bowing during a bulge test. Conventional activation volume highlighted in hashed region.

In Figure 5.1b, the hatched region represents a characteristic area a dislocation must sweep through to overcome the obstacle barrier. The size of this special region multiplied by the dislocation Burgers vector is known as the activation volume and it can be used to illuminate the rate-limiting deformation mechanism for a material. In the absence of stress, the energy barrier for dislocation propagation is ΔF where $\Delta F = \Delta F_0$. However, applying a stress reduces the energy barrier by subtracting an athermal stress component as follows:

$$\Delta F = \Delta F - \tau V_a \quad \textbf{(5.1)}$$

where τ is the applied stress and V_a is the activation volume. As seen in Figure 5.2a, only thermal energy can move a dislocation from X_1 to X_2 in stress-free conditions. Applied stress reduces the needed energy to overcome dislocation obstacles with a characteristic activation volume, V_a, as shown in Figure 5.2b.

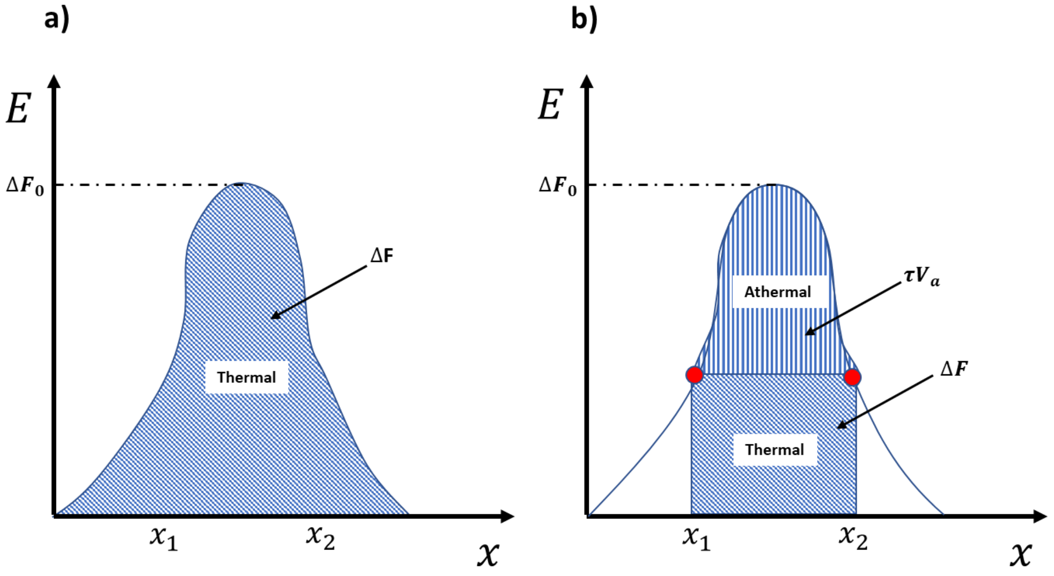

Figure 5.2 Dislocation energy barriers in a) stress-free conditions (thermal only) and b) with athermal applied stress contributions

The activation volume is a function of the area swept by the dislocation as it passes through barriers, with Figure 5.1b showing the conventional description. It is an indicator of the what kind of mechanism is driving the deformation. Qualitatively, V_a will be small for kink-pair mechanisms, larger for dislocation-solute interactions, and larger yet for dislocation-dislocation forest interactions [96]. Building on equation (5.1), Caillard [96] shows that:

$$\tau = -\frac{\alpha k_b T}{V_a} + \frac{\Delta F_0}{V_a} \tag{5.2}$$

Where α is a constant. This indicates that a smaller activation volume will correspond to a rapid decrease in macro stress (τ) while a larger activation volume will have a slower decrease in stress at a given temperature.

One way to measure activation volumes is through macro-scale transient tests such as stress relaxation or creep transient tests. The present work employs the bulge test and an iso-strain stress relaxation experiment. In this test, the stress decrement with time, $\Delta\tau(t)$, can be modeled as a logarithmic decay relation as follows [96]:

$$\Delta\tau(t) = -\frac{k_b T}{V_a} \ln\left(1 + \frac{t}{C_r}\right) \tag{5.3}$$

Where k_b is the Boltzmann constant, V_a is the apparent activation volume, and C_r is the time constant for the relaxation mechanism.

As mentioned earlier, the magnitude of the activation volume provides insight into what deformation mechanism is controlling the stress relaxation process. Activation volumes are listed in units of b^3 where b is the Burgers vector of the material. The absolute values of activation volume are quite small and can range from 10^{-25} to 10^{-29} m^{-3} and are divided by b^3 for comparison purposes. Each material has characteristic Burgers vectors, thus the extraction of activation volumes for a given relaxation event will be different depending on the material. For example, Conrad et al. determined grain size dependence of deformation mechanisms in copper during high-strain, plasticity experiments by analyzing activation volumes [97]. In this study three grain size regimes were identified: coarse-grained ($D \approx 10^{-6}$-10^{-3} m) measured activation volumes of 420 - 2040b^3 indicating traditional intragranular intersection of mobile dislocation mechanisms; an intermediate regime (D ≈ 10^{-8}-10^{-6} m) measuring a 1b^3 activation volume indicating a grain boundary shear plus dislocation pile-up mechanism; and a fine regime (D < ~ 10^{-8} m) where only grain boundary shearing mechanisms were indicated. Another plastic deformation study by Wang [98] of nanocrystalline Ni (D ~ 30 nm or ≈ 10^{-8} m) determined an activation volume around 20b^3 which rules out the low activation volume grain boundary processes described above by Conrad. They suggest a dislocation-based process is driving the mechanism with a high concentration of dislocations near the grain boundaries. This concentrated dislocation density leads to a small pinning distance, L, which corresponds to a relative small activation volume (20b^3 instead of > 100b^3).

In low-strain, anelastic conditions (such as this study's relaxation tests) the activation volume can be thought of as proportional to the work required to bow a dislocation from a straight segment between points A and B of Figure 5.1b until reaching the first insurmountable obstacle. Specifically, work = σV_a. Figure 5.3 shows the sweeping area of a bowing dislocation in low-stress conditions where only the Peierls barrier is overcome. The activation volume is the proportional to the work required to extend a dislocation to its maximum bowed condition.

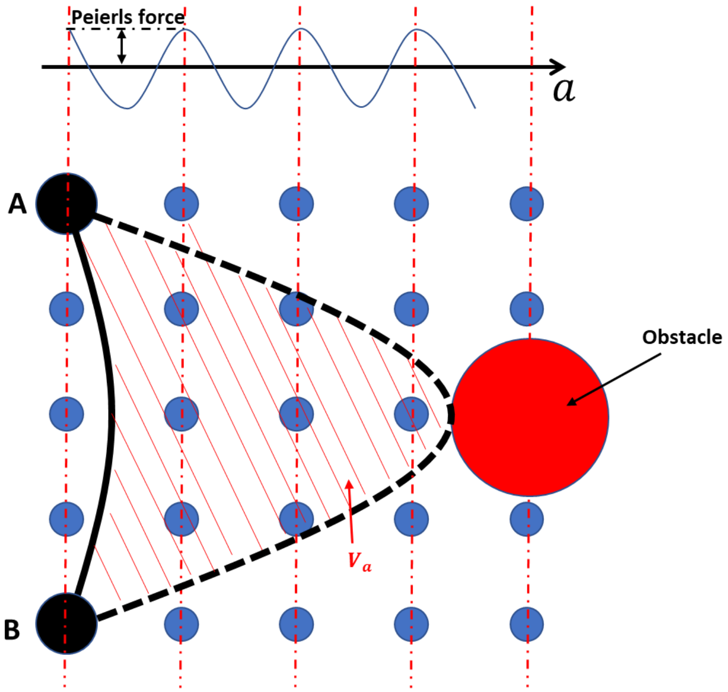

Figure 5.3 Activation volume in anelastic dislocation bowing conditions of the present study

This is considered "preyield microplasticity" and activation volumes can also be measured when the dislocation is sweeping across a Peierls barrier. Activation volumes of approximately $100b^3$ for this type of deformation have been observed in FCC metals [99]. The anelastic mechanism of bowing and unbowing dislocations are commonly attributed to the creation of a propagating double kink, to be discussed in more detail in Section 5.3.

5.2 Apparent activation volume results

Activation volumes for the FCC metal films of the present study were measured by fitting iso-strain relaxation curves to Equation (5.3). As shown in Chapter 3, the Normalized Modulus decay for each film was fit using a four-term

Prony series. This data is converted into a stress decay (ΔT) function using a new set of four Prony constants as determined by:

$$\Delta \mathrm{T} = -\sum_{i=1}^{4} P_i \left(1 - e^{\frac{-t}{\tau_i}}\right) \tag{5.4}$$

with the time constants (τ_i) varying from i=10, 100, 1000, and 10,000 s. The shear stress decay ΔT was converted from a bulge hoop stress divided by the Taylor factor of 3.06 or $\Delta T = \frac{\Delta\sigma_{hoop}}{3.06}$. Incorporation of the Taylor factor allows consistent comparison of dislocation barrier strengths with other research groups [100]. The fitting procedure was performed on each film with an example shown in Figure 5.4.

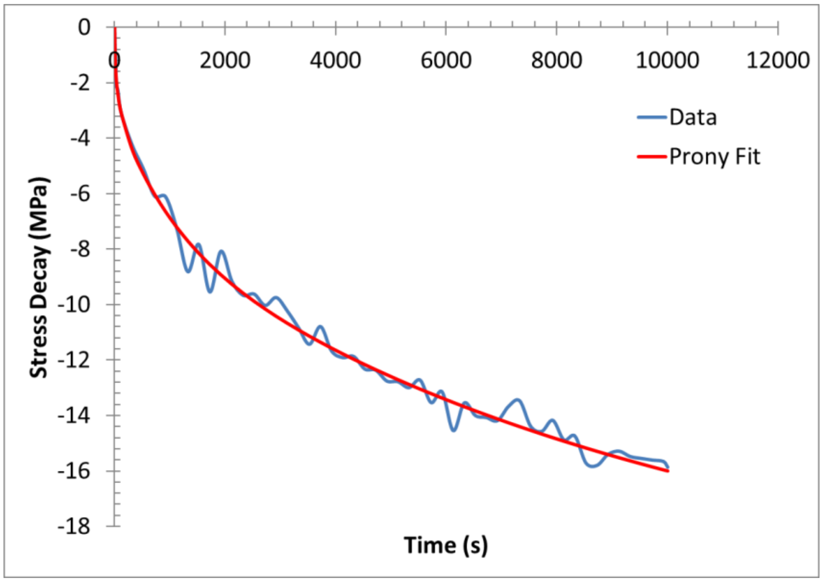

Figure 5.4 Example of fitting relaxation data to stress decay Prony series

The stress-decay Prony constants for all films are tabulated in Table 4.1.

Material	Sputter T	P_1	P_2	P_3	P_4
		$\tau = 10s$	$\tau = 100s$	$\tau = 1000s$	$\tau = 10{,}000s$
Ag	100	1.224	1.735	6.240	2.762
	125	2.079	3.286	7.175	3.572
	150	1.597	1.763	8.034	3.679
	175	1.835	6.096	5.075	2.001
	200	1.842	1.435	8.429	1.754
Al(Mg)	100	0.897	0.626	4.129	1.873
	150	0.469	0.823	5.114	2.501
	200	1.386	1.781	4.500	1.941
Au	100	1.356	0.412	5.482	3.985
	175	1.207	0.209	6.771	5.044
	300	1.049	0.974	6.309	6.425
	400	1.437	1.448	4.177	14.145
Cu	100	2.373	1.329	10.655	6.498
	200	2.638	1.152	8.082	6.534
	300	1.811	1.337	8.776	10.204
Pt	150	1.531	0.518	5.536	3.811
	200	0.846	1.367	5.982	5.913
	300	0.803	1.126	7.866	5.419
	500	1.035	2.480	6.273	8.082

Table 5.1 Stress decay Prony constants for FCC metal films

The activation volume is typically extracted from the first few hundred seconds of relaxation experiments [98,101]. For this work the activation volume is extracted from the first 100 seconds of relaxation, which is dominated by the value of second Prony constant (P_2). An example fitting of the equation (5.3) to the Prony data is shown in Figure 5.5.

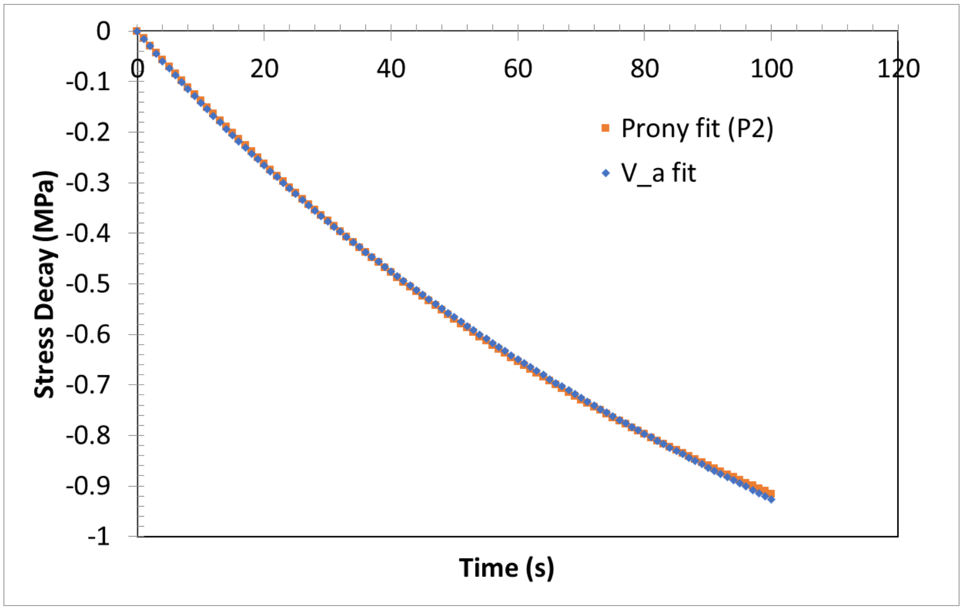

Figure 5.5 Activation volume extraction from Prony fit of relaxation data

The extracted activation volume for each FCC film is plotted in Figure 5.6. A clear trend in decreasing activation volume with increasing grain size is observed in Al(Mg), Au, and Pt thin films, while the activation volume measurement is independent of grain size for Ag and Cu films. Tabulated values of the activation volumes of the first 100 s of relaxation are shown in Table 5.2.

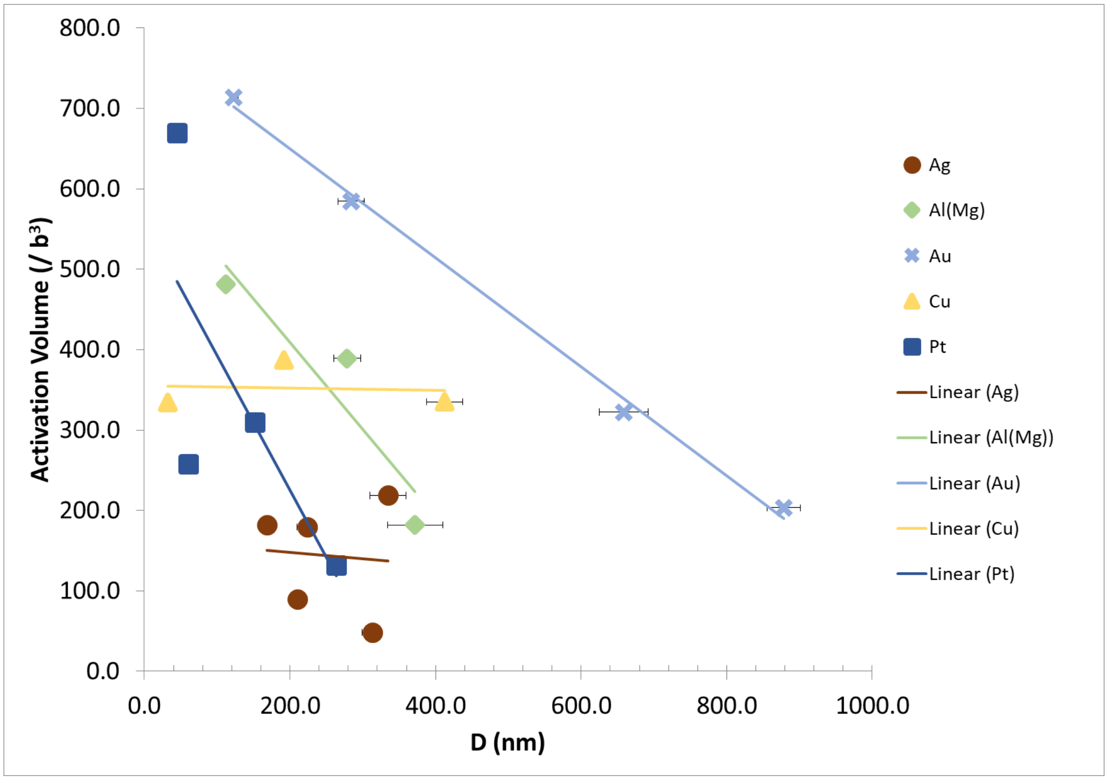

Figure 5.6 Activation volume (V_a) plotted against grain size (D) for all FCC films

Material	Sputter T	D (nm)	V_a for 100 s ΔT (b^3 units)
Ag	100	168.1	182
	125	210.0	89
	150	223.3	179
	175	312.8	48
	200	334.5	218
Al(Mg)	100	111.8	480
	150	278.4	389
	200	371.8	181
Au	100	122.9	713
	175	284.0	584
	300	658.7	322
	400	878.4	203
Cu	100	31.9	334
	200	191.4	386
	300	412.5	335
Pt	150	44.8	669
	200	60.4	257
	300	151.5	309
	500	264.1	132

Table 5.2 Activation volumes for each FCC metal film for 100 s relaxation

5.3 Kink pair formation

A pinned, rectilinear dislocation (Figure 5.7a) can bow under an applied force, even in sub-yield, microplastic conditions [64,96]. The bowing process is initiated by the formation of a kink pair (also known as a double kink nucleation) whereby the dislocation line is extended from one Peierls minimum into the next, see Figure 5.7b. The probability of forming a kink pair is increased with increasing thermal energy.

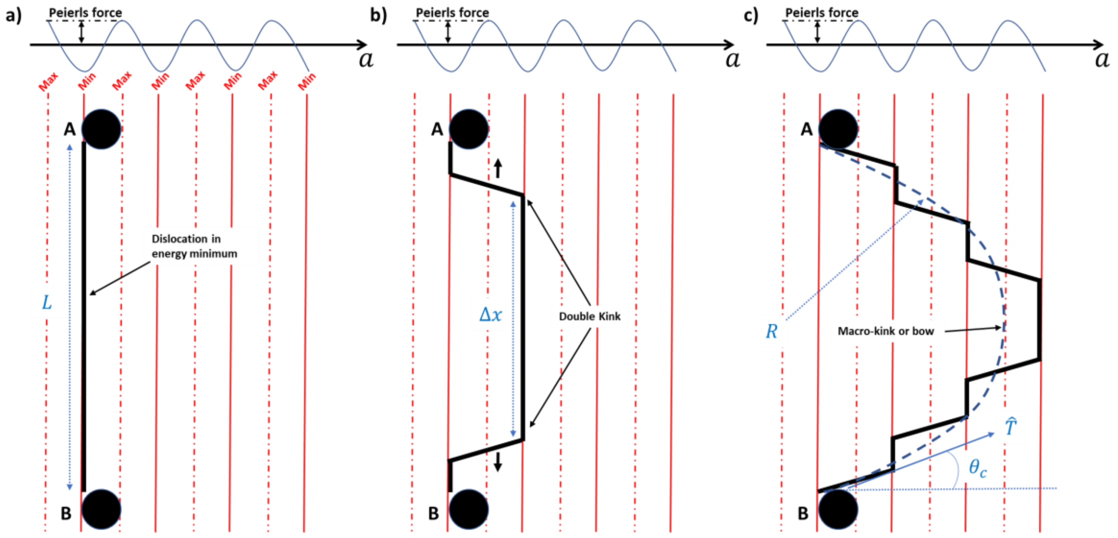

Figure 5.7 Kink pair formation and propagation a) rectilinear, pinned dislocation segment b) double kink forms and extends c) macro-kink or bowed formation

The pinning points A and B will slow down the dislocation bowing but not stop it until spacing ΔX approaches a critical value, ΔX_c. Each kink of the kink pair has the same burgers vector but opposite line direction, therefore under the critical ΔX_c they will tend to attract and annihilate each other. This critical kink separation distance determines when the microscale bowing and macroscale relaxation processes stop. For low stress conditions the critical spacing of kinks is found to be in the range of 20b [64] to 50b [99]. This suggests that a larger initial spacing (L) between pinning points provides a higher probability for a kink to form and not annihilate by having more available line space to reach the critical spacing threshold. This is shown graphically in Figure 5.8 where a shorter L may increase the likelihood of a kink pair annihilating before extending to a stable separation distance.

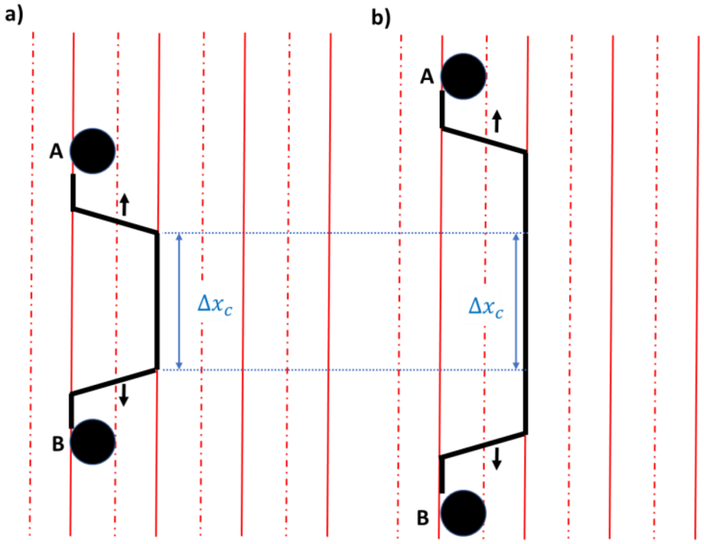

Figure 5.8 Kink pair formation above critical spacing a) small L pinning distance b) large L pinning distance

The successful formation and separation of a kink pair will bow the dislocation one Peierls valley at a time until it becomes energetically unfavorable to form new kinks. The result is a bowed dislocation as in Figure 5.7c. The radius of curvature due to the kink formation events is given as [96]:

$$R = \frac{L}{2cos\theta_c} \tag{5.5}$$

where θ_c is the angle between dislocation line and pinning point, L is the pinning distance, and R is the radius of curvature. The line tension that develops during a bowing event is related to the radius of curvature by $R = \frac{\hat{T}}{\tau b}$, which leads to:

$$\tau = \frac{2\hat{T}}{bL} cos\theta_c \qquad \textbf{(5.6)}$$

Where τ is the applied stress and $\hat{T}$ is the line tension in the curved dislocation. This implies that for a given line tension $\hat{T}$, an increased L will reduce the applied stress necessary to bow a given distance. Similarly, it implies for a given applied stress, a dislocation with a larger pinning distance will propagate farther than one with a shorter pinning distance.

The stress relaxation tests from this work show a changing (decreasing) activation volume in those films that also displayed an increased pinning distance L. A lower activation volume with increasing grain size correlated with an increased modulus decay in the bulge tests. Knowing that activation volume is proportional to the work to overcome barriers as $\Delta W \propto \sigma V_a$ [66], the lower activation volumes imply that anelastic bowing is energetically more favorable in films that generate larger dislocation spacings.

5.4 Summary

The activation volumes extracted from stress relaxation tests indicate the general deformation mechanism responsible for viscoelasticity in the metallic thin films. The extracted activation volumes range between 50b^3 to 700b^3 for all FCC metals films across all grain sizes. This intermediate V_a range indicates a dislocation-based mechanism is responsible for the observed viscoelasticity. The anelastic bowing and unbowing of dislocations can be accommodated by the formation of kink pairs. These kink pairs will extend the dislocation line by overcoming the Peierls barrier. It is shown that a dislocation that has a larger initial pinning distance L will have a reduced barrier to bowing. Increasing grain size was shown to increase the pinning distance L, which correlates with an increased relaxation extent.

6. Conclusions and future work

6.1 Conclusions

Thin metallic films used in RF MEMS devices are often nanocrystalline and of high purity, primarily due to the constraints of the deposition process. Consequently, these films exhibit anomalous mechanical behaviors that can lead to degradation of device performance. The focus of this work was investigating the grain size effects on low-strain, stress relaxation response in sub-micron thickness metallic films. A series of FCC materials, including Ag, Al(Mg), Au, Cu, and Pt were investigated using the gas pressure bulge test at a temperature of 80 °C.

The in-plane grain size of each film was adjusted by heating the substrate during the DC magnetron sputtering process. SEM analysis revealed the grain size, D, to vary from tens to hundreds of nanometers. Stress relaxation tests on each film were performed until a steady state viscoelastic response was determined. The evaluation metric was the plane strain modulus decay after 10,000 s of relaxation at a constant strain of 0.1%. The Al(Mg), Au, and Pt films showed increased relaxation (i.e. larger modulus decay) with increasing grain size while the Ag and Cu films showed no relaxation dependence on grain size. The relaxation dependence was shown to be linearly proportional to D^n where n ranged from ½ to 2.

A dislocation-based deformation mechanism is proposed as controlling the viscoelastic relaxation and recovery processes observed in the FCC films. The sputtering process tends to generate a relatively high concentration of dislocations as the deposited film cools. The dislocation densities as measured via TEM and XRD techniques were found to lie between 4.1×10^{14} m^{-2} to 15.1×10^{14} m^{-2} for all films. The dislocations disperse in such a way to relieve stresses generated between film and substrate. This dispersion generates an average pinned dislocation segment length, L, between mobile dislocations that determines the extent of relaxation. The anelastic bowing and unbowing of dislocations within the pinned L spacing generates the global relaxation response. This microstructural feature, L, most likely increases with grain size, D, in those films that exhibit a relaxation dependence on grain size.

The activation volume, V_a, was extracted from the first 100 s of each FCC metal steady-state viscoelastic relaxation test. It ranged from $50b^3$ to $700b^3$. The magnitude of V_a indicated that dislocation-based deformation mechanisms were responsible for the observed relaxation. Other commonly proposed mechanisms such as grain boundary sliding ($V_a \sim 1b^3$) and dislocation-forest interactions ($V_a \sim >1000b^3$) were ruled out with this measurement. Anelastic bowing of dislocations across the Peierls barrier are known to have activation volumes near $100b^3$ indicating a reasonable match to this present work. For those films that showed grain size dependence on relaxation, V_a was observed to decrease with D. Since the activation volume is proportional to the work required to overcome the Peierls barrier, a decreased V_a would indicate that larger grained films will relax more due to increased bowing of dislocations.

A key outcome of this work was observing that most, perhaps all, FCC metallic films will exhibit a viscoelastic relaxation in response to sub-yield stress environments. The proposed mechanism for deformation, anelastic bowing of pinned dislocations due to kink pair formation, appears to be active in all metal films as shown by this work. The grain size-dependence of time-dependent deformation is not an independent mechanism that determines the extent of relaxation to a given stimulus, like Hall-Petch strengthening is for all metals. Instead, grain size often correlates with microstructural features that are important to the deformation response. For instance, this study revealed that if an increasing grain size, D, changes the dislocation arrangement via increases in L, the relaxation extent will increase.

6.2 Practical impact of work

Design engineers of bulk components and devices have access to resources that help to optimize the selection of an alloy for a given application. The bulk material properties are well characterized in textbooks, online databases, and commercial software packages. The thin film material property resources are not as richly developed for MEMS design engineers, potentially leading to sub-optimal selection of material for a given application. This conclusions from the present study suggest guidelines a MEMS designer should follow when designing for low-strain elastic environments, common to RF MEMS applications. Three rules of thumb could be extracted from the viscoelastic results of this work:

1. All FCC metal films are susceptible to viscoelastic relaxation, regardless of melting point. Low (Al) and high melting point films (Pt) showed time-dependent deformation due to dislocation bowing

across the Peierls barrier. To increase reliability, there are a few practical solutions that can be employed to minimize the relaxation behavior. One would be alloying the FCC base metal which will raise the Peierls barrier and decrease the extent of dislocation bowing. Another solution would be to substitute the FCC moving membrane material with a BCC metal, since BCC metals exhibit a much higher Peierls barrier. Barriers to dislocation motion are higher in BCC materials and anelastic bowing should be reduced.

2. Keeping the in-plane grain size, D, of the metal film as small as possible is not a guaranteed method for relaxation resistance, but keeping D small is generally preferred to larger-grained films.
3. Employing manufacturing strategies to keep L small will reduce relaxation behavior. One way to keep the pinning distance short is to alloy the base metal with solid solutions or dispersions. These dispersed obstacles within the grain will cause shorter segments of pinned dislocations and reduce the maximum modulus decay. Thermal exposure during processing should be avoided to prevent annealing of the microstructure which will increase the L spacing. Additionally, the operating temperature should be kept as low as possible to strengthen the pinning points in the existing dislocation network.

6.3 Future work

The present work investigated the grain size effects on low strain viscoelastic relaxation in common FCC metallic thin films. The understanding of the stress relaxation response is not nearly complete and many areas are available for continued work. The following will highlight some areas that were either lightly touched on in this work or require more in-depth analysis:

1. The most obvious need for further study coming from this work is why the Al(Mg), Au, and Pt films showed D^n relaxation response while the Ag and Cu films did not. It is suspected that the Ag and Cu films showed an increased density of growth twins that would impact the character and arrangement of dislocations that formed during deposition. These two materials generally have a low stacking fault energy which implies these metals are more prone to growth twins. A systematic study of a low SFE material, such as Ag, would further reveal the impact that twins have on anelastic dislocation deformation. It is known that adjusting the sputter deposition rate greatly influences the twinning density of low SFE materials and would be a straightforward way to observe the twin influence on anelasticity under constant grain size.
2. The dislocation density, ρ, of a film is one contributor to the pinned dislocation segment distance, L. This present study indicated that changing the grain size of a film does not necessarily change the

dislocation density, but the arrangement of distributed dislocations can change with grain size, affecting the L parameter. Further work isolating the impact of dislocation density is needed where the grain size of the film is kept constant while adjusting the dislocation density.

3. Further in-situ TEM viscoelastic relaxation studies of films within the grain size range of this study would clarify the nature of the dislocation-based deformation process. This type of investigation would complement the macro-scale transient bulge testing of this work by providing grain-specific deformation behavior.
4. With great difficulty, one single crystal Ag film was tested using the bulge test. The film measured nominal viscoelastic relaxation, indicating the presence or lack of grain boundaries is not a significant contributor to the relaxation extent. Further study of single crystal films would allow the isolation and study of microstructural features, such as dislocations or other defects without the influence of grain boundaries. The single crystal Ag film was epitaxially deposited onto a bulge coupon using a collaboration with the Max Plank Institute for Intelligent Systems in Stuttgart, Germany. It is also possible to epitaxially grow single crystal films on a NaCl single crystal, but the removal, transfer, and adherence to the bulge test coupon is very problematic.

5. Alloying pure metals with precipitates is a common way to strengthen bulk metals. Prior work in our group demonstrated improved relaxation resistance by alloying Au thin films with reactively sputtered V_2O_5 precipitates. An alternative could be co-sputtering more reactive base metals, such as Cu, with other elements that are immiscible. A Cu-Ta film would provide an economical option for increased relaxation resistance when reactive sputtering is not possible. A few Cu-Ta thin films were made in this work, and TEM analysis showed interesting phase separation behavior between the Cu and Ta species at different sputtering temperatures. However, during low temperature bulge testing, the microstructure proved unstable as the films showed visible evidence of diffusion or rearrangement on the surface. Further work on understanding this phenomenon might lead to practical manufacturing solutions for common MEMS device materials.
6. Most sputtered films form columnar grains with (111)-orientation. This was true for this work, except for the single crystal Ag film, which was grown epitaxially on a (100) surface. The dislocation-based relaxation mechanism proposed in this work is the bowing and unbowing of dislocations over the Peierls barrier. In FCC metals, this only occurs on the {111} slip planes in <110> directions. Other

textures could reduce the resolved shear stress on the {111} planes, thereby reducing the driving force for relaxation.

7. References

[1] S.M. Spearing, Acta Mater. 48 (2000) 179–196.

[2] G.M. Rebeiz, C.D. Patel, S.K. Han, C.H. Ko, K.M.J. Ho, IEEE Microw. Mag. 14 (2013) 57–67.

[3] G.M. Rebeiz, RF MEMS: Theory, Design, and Technology, John Wiley & Sons, 2004.

[4] E.R. Brown, IEEE Trans. Microw. Theory Tech. 46 (1998) 1868–1880.

[5] A. Basu, G.G. Adams, N.E. McGruer, J. Micromechanics Microengineering 26 (2016) 104004.

[6] X. Yan, W.L. Brown, Y. Li, J. Papapolymerou, C. Palego, J.C.M. Hwang, R.P. Vinci, J. Microelectromechanical Syst. 18 (2009) 570–576.

[7] M. McLean, W.L. Brown, R.P. Vinci, J. Microelectromechanical Syst. 19 (2010) 1299–1308.

[8] K. Mongkolsuttirat, Time and Temperature Dependence of Viscoelastic Stress Relaxation in Au and Au Alloy Thin Films, Lehigh University, 2013.

[9] K. Nadaud, F. Roubeau, A. Pothier, P. Blondy, L.Y. Zhang, R. Stefanini, in: 2016 IEEE MTT- Int. Microw. Symp. IMS, 2016, pp. 1–4.

[10] B. Lakshminarayanan, D. Mercier, G.M. Rebeiz, IEEE Trans. Microw. Theory Tech. 56 (2008) 971–981.

[11] D. Mercier, K.V. Caekenberghe, G.M. Rebeiz, in: IEEE MTT- Int. Microw. Symp. Dig. 2005, 2005, pp. 4 pp.-.

[12] H. Sedaghat-Pisheh, R. Mahameed, G.M. Rebeiz, in: 2011 IEEE MTT- Int. Microw. Symp., 2011, pp. 1–4.

[13] V. Mulloni, G. Resta, B. Margesin, J. Micromechanics Microengineering 24 (2014) 075003.

[14] G.-D. Sim, J.A. Krogstad, K.M. Reddy, K.Y. Xie, G.M. Valentino, T.P. Weihs, K.J. Hemker, Sci. Adv. 3 (2017) e1700685.

[15] S.J. Suresha, M. Haj-Taieb, K. Bade, J. Aktaa, K.J. Hemker, Scr. Mater. 63 (2010) 1141–1144.

[16] J.R. Greer, W.C. Oliver, W.D. Nix, Acta Mater. 53 (2005) 1821–1830.

[17] A.Y. Cho, J.R. Arthur, Prog. Solid State Chem. 10 (1975) 157–191.

[18] S.M. George, Chem. Rev. 110 (2010) 111–131.

[19] C.K. Malek, V. Saile, Microelectron. J. 35 (2004) 131–143.

[20] P.J. Kelly, R.D. Arnell, Vacuum 56 (2000) 159–172.

[21] N. Laegreid, G.K. Wehner, J. Appl. Phys. 32 (1961) 365–369.

[22] D.L. Smith, Thin-Film Deposition : Principles and Practice, International ed, New York : McGraw-Hill, 1995.

[23] I. Petrov, P.B. Barna, L. Hultman, J.E. Greene, J. Vac. Sci. Technol. A 21 (2003) S117–S128.

[24] C.V. Thompson, R. Carel, Mater. Sci. Eng. B 32 (1995) 211–219.

[25] W.D. Callister, Materials Science and Engineering: An Introduction, 2014.

[26] R.W. Hertzberg, R.P. Vinci, J.L. Hertzberg, Deformation and Fracture Mechanics of Engineering Materials, 5th Edition, Wiley Global Education, 2012.
[27] K. Lu, L. Lu, S. Suresh, Science 324 (2009) 349–352.
[28] H.M. Otte, J.J. Hren, Exp. Mech. 6 (1966) 177–193.
[29] H. Conrad, Acta Metall. 11 (1963) 75–77.
[30] H. Huang, F. Spaepen, Acta Mater. 48 (2000) 3261–3269.
[31] W.C. Oliver, G.M. Pharr, J. Mater. Res. 7 (1992) 1564–1583.
[32] G.M. Pharr, W.C. Oliver, MRS Bull. 17 (1992) 28–33.
[33] R. Saha, W.D. Nix, Acta Mater. 50 (2002) 23–38.
[34] W.D. Nix, Metall. Trans. A 20 (1989) 2217.
[35] G.G. Stoney, Proc R Soc Lond A 82 (1909) 172–175.
[36] G.C.A.M. Janssen, M.M. Abdalla, F. van Keulen, B.R. Pujada, B. van Venrooy, Thin Solid Films 517 (2009) 1858–1867.
[37] M.D. Thouless, J. Gupta, J.M.E. Harper, J. Mater. Res. 8 (1993) 1845–1852.
[38] M.A. Haque, M.T.A. Saif, Exp. Mech. 42 (2002) 123–128.
[39] J.H. Han, M.T.A. Saif, Rev. Sci. Instrum. 77 (2006) 045102.
[40] Y. Zhu, H.D. Espinosa, Proc. Natl. Acad. Sci. 102 (2005) 14503–14508.
[41] Y. Xiang, X. Chen, J. j. Vlassak, J. Mater. Res. 20 (2005) 2360–2370.
[42] J.J. Vlassak, W. d. Nix, J. Mater. Res. 7 (1992) 3242–3249.
[43] M.K. Small, W.D. Nix, J. Mater. Res. 7 (1992) 1553–1563.
[44] B. Merle, M. Göken, J. Mater. Res. 29 (2014) 267–276.
[45] B. Merle, E.W. Schweitzer, M. Göken, Philos. Mag. 92 (2012) 3172–3187.
[46] H.J. Frost, M.F. Ashby, Deformation Mechanism Maps: The Plasticity and Creep of Metals and Ceramics, Pergamon Press, Oxford, UK, 1982.
[47] M.F. Ashby, Acta Metall. 20 (1972) 887–897.
[48] S.-J. Hwang, Y.-C. Joo, J. Koike, Thin Solid Films 516 (2008) 7588–7594.
[49] R.L. Coble, J. Appl. Phys. 34 (1963) 1679–1682.
[50] G.-D. Sim, J.J. Vlassak, Scr. Mater. 75 (2014) 34–37.
[51] A.J. Kalkman, A.H. Verbruggen, G.C. a. M. Janssen, Appl. Phys. Lett. 78 (2001) 2673–2675.
[52] X. Li, Y. Wei, W. Yang, H. Gao, Proc. Natl. Acad. Sci. 106 (2009) 16108–16113.
[53] N. Karanjgaokar, F. Stump, P. Geubelle, I. Chasiotis, Scr. Mater. 68 (2013) 551–554.
[54] N.J. Karanjgaokar, C.-S. Oh, J. Lambros, I. Chasiotis, Acta Mater. 60 (2012) 5352–5361.
[55] X. Wei, D. Lee, S. Shim, X. Chen, J.W. Kysar, Scr. Mater. 57 (2007) 541–544.
[56] N. Wang, Z. Wang, K.T. Aust, U. Erb, Mater. Sci. Eng. A 237 (1997) 150–158.
[57] H.-J. Lee, P. Zhang, J.C. Bravman, Thin Solid Films 476 (2005) 118–124.
[58] L.I.J.C. Bergers, J.P.M. Hoefnagels, M.G.D. Geers, Acta Mater. 124 (2017) 47–58.

[59] J. Rajagopalan, J.H. Han, M.T.A. Saif, Science 315 (2007) 1831–1834.
[60] J. Rajagopalan, J.H. Han, M.T.A. Saif, Scr. Mater. 59 (2008) 921–926.
[61] A.S. Nowick, B.S. Berry, Anelastic Relaxation in Crystalline Solids, Academic Press, 1972.
[62] N. Ghazi, J.W. Kysar, Exp. Mech. (2016) 1–12.
[63] D. Choi, W.D. Nix, Acta Mater. 54 (2006) 679–687.
[64] D. Hull, D.J. Bacon, Introduction to Dislocations - (Fifth Edition) - ScienceDirect, n.d.
[65] J. Friedel, Lond. Edinb. Dublin Philos. Mag. J. Sci. 44 (1953) 444–448.
[66] G.E. Dieter, Mechanical Metallurgy, McGraw-Hill, 1986.
[67] K.R. Williams, R.S. Muller, J. Microelectromechanical Syst. 5 (1996) 256–269.
[68] K.R. Williams, K. Gupta, M. Wasilik, J. Microelectromechanical Syst. 12 (2003) 761–778.
[69] A.A. Volinsky, N.R. Moody, W.W. Gerberich, Acta Mater. 50 (2002) 441–466.
[70] R.H. Dauskardt, M. Lane, Q. Ma, N. Krishna, Eng. Fract. Mech. 61 (1998) 141–162.
[71] M.-A. Nicolet, Thin Solid Films 52 (1978) 415–443.
[72] J.J. Yang, J.P. Strachan, Q. Xia, D.A.A. Ohlberg, P.J. Kuekes, R.D. Kelley, W.F. Stickle, D.R. Stewart, G. Medeiros-Ribeiro, R.S. Williams, Adv. Mater. 22 (2010) 4034–4038.
[73] H. Okamoto, J. Phase Equilibria 19 (1998) 598.
[74] W.A. Soer, J.T.M.D. Hosson, A.M. Minor, J.W. Morris, E.A. Stach, Acta Mater. 52 (2004) 5783–5790.
[75] G.K. Williamson, W.H. Hall, Acta Metall. 1 (1953) 22–31.
[76] B.E. Warren, B.L. Averbach, J. Appl. Phys. 21 (1950) 595–599.
[77] G. Ribárik, T. Ungár, J. Gubicza, J. Appl. Crystallogr. 34 (2001) 669–676.
[78] G. Ribárik, J. Gubicza, T. Ungár, Mater. Sci. Eng. A 387–389 (2004) 343–347.
[79] G. Csiszár, L. Balogh, A. Misra, X. Zhang, T. Ungár, J. Appl. Phys. 110 (2011) 043502.
[80] R.K. Ham, Philos. Mag. J. Theor. Exp. Appl. Phys. 6 (1961) 1183–1184.
[81] Y. Miyajima, S. Okubo, H. Abe, H. Okumura, T. Fujii, S. Onaka, M. Kato, Mater. Charact. 104 (2015) 101–106.
[82] I.J. Beyerlein, X. Zhang, A. Misra, Annu. Rev. Mater. Res. 44 (2014) 329–363.
[83] J. Spreadborough, J.W. Christian, J. Sci. Instrum. 36 (1959) 116.
[84] F.M. Mulder, B. Assfour, J. Huot, T.J. Dingemans, M. Wagemaker, A.J. Ramirez-Cuesta, J. Phys. Chem. C 114 (2010) 10648–10655.
[85] K. Lejaeghere, V.V. Speybroeck, G.V. Oost, S. Cottenier, Crit. Rev. Solid State Mater. Sci. 39 (2014) 1–24.
[86] H. Okamoto, T.B. Massalski, Bull. Alloy Phase Diagr. 4 (1983) 190–198.
[87] D. Dayal, P. Rudolf, P. Wiβmann, Thin Solid Films 79 (1981) 193–199.
[88] L.O. Bueno, R.L. Bell, Mater. Sci. Eng. A 410–411 (2005) 72–78.

[89] J.P. Hirth, Metall. Trans. 3 (1972) 3047–3067.

[90] Z. Shen, R.H. Wagoner, W.A.T. Clark, Acta Metall. 36 (1988) 3231–3242.

[91] K. Mongkolsuttirat, J.R. Smyth, W.L. Brown, R.P. Vinci, Scr. Mater. 155 (2018) 1–4.

[92] G. Dehm, T.J. Balk, H. Edongué, E. Arzt, Microelectron. Eng. 70 (2003) 412–424.

[93] T.J. Balk, G. Dehm, E. Arzt, MRS Online Proc. Libr. Arch. 673 (2001).

[94] G. Csiszár, K. Pantleon, H. Alimadadi, G. Ribárik, T. Ungár, J. Appl. Crystallogr. 45 (2012) 61–70.

[95] M. Hecq, A. Hecq, J.I. Langford, J. Appl. Phys. 53 (1982) 421–427.

[96] D. Caillard, J.L. Martin, Thermally Activated Mechanisms in Crystal Plasticity, Volume 8 - 1st Edition, 2003.

[97] H. Conrad, Mater. Sci. Eng. A 341 (2003) 216–228.

[98] Y.M. Wang, A.V. Hamza, E. Ma, Acta Mater. 54 (2006) 2715–2726.

[99] G. Fantozzi, C. Esnouf, W. Benoit, I.G. Ritchie, Prog. Mater. Sci. 27 (1982) 311–451.

[100] R.E. Stoller, S.J. Zinkle, J. Nucl. Mater. 283–287 (2000) 349–352.

[101] L. Lu, T. Zhu, Y. Shen, M. Dao, K. Lu, S. Suresh, Acta Mater. 57 (2009) 5165–5173.

VITA

Name: Jeffrey R. Smyth

Date of Birth: May 2, 1985

Place of Birth: Carmel, New York, USA

Parents: Douglas Smyth and Kathleen Magnusson

Education:

M.S. Materials Science & Engineering
Rutgers University, Piscataway, NJ, USA, October 2012

B.S. Ceramic Engineering
Rutgers University, Piscataway, NJ, USA, May 2007

Professional experience:

Design Engineer
U.S. Army Armament Research, Development & Engineering Center
Picatinny Arsenal, NJ, July 2009 - present